Surfactant Self-assembly in a Magnetic Room Temperature Ionic Liquid

vorgelegt von

Diplom-Chemiker Andreas Klee

geb. in Geilenkirchen

von der Fakultät II - Mathematik und Naturwissenschaften

der Technischen Universität Berlin

zur Erlangung des akademischen Grades

Doktor der Naturwissenschaften

Dr.rer.nat.

genehmigte Dissertation

Promotionsausschuss:

Vorsitzender: Prof. Dr. Peter Strasser

1. Gutachter: Prof. Dr. Michael Gradzielski (Technische Universität Berlin)

2. Gutachter: Prof. Dr. Werner Kunz (Universität Regensburg)

Tag der wissenschaftlichen Aussprache: 22. Mai 2015

Berlin 2015

Danksagung

An erster Stelle möchte ich mich ganz herzlich bei Prof. Dr. Michael Gradzielski bedanken, in dessen Arbeitskreis ich die letzten Jahre die Möglichkeit hatte, meine Dissertation anzufertigen. Ich bedanke mich einerseits für das große Vertrauen, mir so viele Freiheiten zur selbständigen Arbeit und Ideenentwicklung zu überlassen, andererseits bestand jederzeit die Möglichkeit zur wissenschaftlichen Diskussion, welche während der gesamten Zeit immer wieder sehr hilfreich war. Auch bedanken möchte ich mich für die Ermöglichung von so vielen Konferenzbesuchen, welche einen erheblichen Beitrag dazu lieferten, regelmäßig über den Tellerrand schauen zu können.

Die gegebenen Experimentiermöglichkeiten durch die Ausstattung im Institut vor Ort wurden massiv erweitert durch Messreisen zu verschiedenen europäischen Neutronenquellen, wofür ich mich beim HZB Wannsee, PSI Villigen, ILL Grenoble und LLB Saclay für die bewilligten Messzeiten bedanken möchte. Ebenso bei Klaus Kiefer vom LaMMB (HZB Wannsee) für die Ermöglichung der magnetischen SQUID-Messungen.

Großer Dank geht ebenfalls an alle Mitarbeiter des Stranski-Labors, für eine sehr angenehme Arbeitsatmosphäre, in der mir viel Hilfs- und Disskussionsbereitschaft entgegengebracht wurde. Ganz besonders danke ich Sylvain Prevost, der einen erheblichen Anteil meines Verständnisses für Kleinwinkelstreuung zu verantworten hat und Lisa Reile und Miriam Simon, die mich im Rahmen ihrer Bachelorarbeit bzw. hilfswissenschaftlichen Tätigkeit unterstützt haben. Nicht zu vergessen sind auch die Mitarbeiter der Werkstatt und der Glasbläserei, mit deren Hilfe verschiedenste Versuchsaufbauten überhaupt erst realisiert werden konnten.

Neben aller fachlichen Unterstützung möchte ich mich jedoch ebenso bei all den Menschen bedanken, mit denen ich in den letzen Jahren neben der Doktorarbeit Zeit verbracht habe. Dies gab mir immer wieder die wichtige Möglichkeit, Abstand zu nehmen von der spezialisierten Tätigkeit des Grundlagenforschers, was immer wieder Kraft, Gelassenheit und einen geschärften

Blick fürs wesentliche und große Ganze gefördert hat. Neben all den neuen und alten Freunden bedanke ich mich hierfür vor allem bei den Laubenmusikern, meiner Familie und natürlich der phantastischen Katharina.

Parts of this thesis has already been published as listed in the following:

- **Paper I:** "Magnetic Microemulsions based on Magnetic Ionic Liquid" A. Klee, S. Prevost, W. Kunz, R. Schweins, K. Kiefer and M. Gradzielski. *Phys. Chem. Chem. Phys.*, **2012**, *14*, 15355–15360. http://pubs.rsc.org/en/content/articlepdf/2012/cp/c2cp43048g – Reproduced by permission of the PCCP Owner Societies.

- **Paper II:** "Self-Assembly of Imidazolium-Based Surfactants in Magnetic Room-Temperature Ionic Liquids: Binary Mixture" A. Klee, S. Prevost and M. Gradzielski. *ChemPhysChem*, **2014**, *15*, 4032–4041. http://onlinelibrary.wiley.com/doi/10.1002/cphc.201402548/pdf – Reprinted with permission. Copyright 2014 Wiley-VCH.

- **Paper III:** "Understanding and Optimising Microemulsions with Magnetic Room Temperature Ionic Liquids (MRTIL)" A. Klee, S. Prevost, U. Gasser and M. Gradzielski. *J. Phys. Chem. B*, **2015**, *119*, 4133–4142. http://pubs.acs.org/doi/pdf/10.1021/jp512545c – Reprinted with permission. Copyright 2015 American Chemical Society.

Contents

Abstract

In this work the self-assembly in a nonaqueous system was investigated, realized by using different magnetic room temperature ionic liquids (MRTIL, alkylmethylimidazolium tetrachloroferrates, $C_i$mim$FeCl_4$ with i = 2, 4, 6) as solvent and imidazolium based surfactants ($C_j$mimCl with j=12, 14, 16, 18) as amphiphile.

In a systematic fashion the phase behavior was studied. For this purpose we started with the simplest case of binary MRTIL/surfactant mixtures where the alkyl chain length of surfactant and MRTIL was varied over a broad temperature range and the complete range of compositions. In this way it was possible to find classical mesoscopic structures like micelles and liquid crystalline structures. The complexity was extended by adding oil and cosurfactant to the system which enabled us to formulate microemulsions. Again the influence of surfactant and MRTIL alkyl chain lengths on the phase behavior was investigated and additionally the investigation was broadened by a versatile variation of the structure and amount of the cosurfactant and oil. To ensure an as substantive and reliable picture as possible it was made use of many complementary methods as calorimetry (DSC), polarized microscopy, neutron and X-ray scattering (SANS/SAXS), and surface tension.

In general it was proven that it is possible to form typical self-assembled structures in this MRTIL-based matrix like micelles, liquid crystals, emulsions and microemulsions as they are common for classical aqueous systems. However in difference to the latter ones it was shown that the ability to self-assemble is weaker which is expressed e. g. by higher critical aggregation concentrations leading to micelles with rather low aggregation numbers and which are partly swollen by the solvent, or smaller tri-phasic regions for microemulsions, in which the mesoscopic domains show a less pronounced long range ordering.

The weakness in self-assembly was quantified by the solvophobic effect of the alkyl chain which is in the MRTIL only about a fifth of that in water. It

was distinguished between the effects of the solvophobic and -philic part of the surfactant and as a result it was quantitatively shown that deficits in the ability to self-assemble are mainly present in the surfactant's solvophobic tail. Two opposed trends for the amphiphilic stregth could be pointed out given on the one hand by the length of surfactant alkyl chains which quantifies the solvophobicity of the amphiphile, and on the other hand by the length of MRTIL alkyl chains, which quantifies the solvent polarity.

As for this study ionic liquids with paramagnetic properties were chosen, it was proven that this property is still present in the formulated microemulsion systems. As a second result it was possible to orient mesoscopic structures in an external magnetic field. However this was only possible for certain locations in the phase diagrams and at rather high magnetic fields of ≥ 5.5 Tesla.

In summary, the here presented broad investigation yields quantitative information on the composition-structure relationship and therefore gives recipes to design magnetic self-assembled structures with optimised properties and structures, as it has not yet been done for such systems that can be manipulated by a magnetic field. These findings are useful for designing strategies for formulating microemulsions of a given structure with MRTILs as polar component. This is important as such microemulsions could in the future be employed as interesting reaction media which contain also a component for separation via magnetic forces.

Zusammenfassung

In der vorliegenden Arbeit wurde die Selbstorganisation von Tensiden in einem wasserfreien System untersucht, und zwar durch Verwendung von verschiedenen magnetischen Raumtemperatur ionischen Flüssigkeiten (MRTIL, Alkylimidazoliumtetrachloroferraten, $C_i$mim$FeCl_4$ mit i = 2, 4, 6) als Lösungsmittel und Tenside mit einer Imidazolium-Kopfgruppe ($C_j$mimCl mit j=12, 14, 16, 18).

Das Phasenverhalten wurde zuerst für den einfachsten Fall von binären MRTIL/Tensid-Mischungen untersucht, indem systematisch die Kettenlänge von Tensid und MRTIL über einen breiten Temperaturbereich und in allen Mischungsverhältnissen variiert wurde. Dabei wurden klassische mesoskopische Strukturen gefunden wie z.B. Mizellen und Flüssigkristalle. Desweiteren wurde durch die Zugabe von Öl und Kotensid die Komplexität erhöht, woduch es möglich war, Mikroemulsionen herzustellen. Auch hier wurde der Einfluss von MRTIL- und Tensidkettenlängen auf das Phasenverhalten untersucht und zusätzlich durch eine vielfältige Variation von Menge und Struktur des Öls und Kotensids das Beobachtungsspektrum erweitert. Um ein möglichst fundiertes und vertrauenswürdiges Bild zu erhalten, wurden viele komplementäre Methoden wie Kalorimetrie (DSC), Polarisationsmikroskopie, Neutronen- und Röntgenstreuung (SANS/SAXS) und Oberflächenspannung verwendet.

Generell konnten die für wässrige Systeme typischen Strukturen wie Mizellen, Flüssigkristalle, Emulsionen und Mikroemulsionen in diesen ionischen Flüssigkeiten dargestellt werden, jedoch mit einer schwächer ausgeprägten Triebkraft, ausgedrückt z. B. durch höhere kritische Mizellisierungskonzentrationen, kleinere Aggregationszahlen für Mizellen, welche zusätzlich eine teilweise Quellung mit Lösungsmittel aufwiesen, oder kleineren Dreiphasengebieten für Mikroemulsionen, deren Domänen eine weniger ausgeprägte Fernordnung zeigten.

Die schwächere Selbstorganisation wurde mit der Solvophobie der Alkylketten quantifiziert, welche etwa nur ein fünftel in den MRTIL-Systemen ver-

glichen mit Wasser beträgt. Es konnte zwischen dem Effekt von solvophilem und -phobem Tensidteil unterschieden werden mit dem Ergebnis, dass Defizite in der Fähigkeit zur Selbstorganisation hauptsächlich auf den solvophoben Tensidmolekülteil zurückzuführen sind. Zwei entgegengesetzte Trends zur Beeinflussung der amphiphilen Stärke des Systems konnten herausgestellt werden: Einerseits quantifiziert die Tensidkettenlänge die Solvophobizität des Amphiphils und andererseits erhöht die MRTIL-Alkylkettenlänge die Lösungsmittelpolarität.

Da in der vorliegenden Arbeit ionische Flüssigkeiten mit paramagnetischen Eigenschaften verwendet wurden, wurde verifiziert, dass diese Eigenschaft in den untersuchten Mikroemulsionssystemen erhalten blieb. Desweiteren was es möglich, mesoskopische Strukturen in einem externen Magnetfeld auszurichten, jedoch nur für ganz bestimmte Bereiche im Phasendiagramm und unter recht hohen Feldern von $\geq 5.5\,\mathrm{Tesla}$.

Zusammenfassend liefert die hier vorgestellte Arbeit quantitative Informationen zur Struktur-Eigenschaftsbeziehung und gibt damit Anleitung zur maßgeschneiderten Formulierung von mesoskopischen Strukturen mit magnetischen Eigenschaften. Dies ermöglicht z. B. die gezielte Herstellung von Mikroemulsionen mit bestimmten Strukturen, welche MRTIL als polare Komponente enthalten. Dies ist nützlich, da solche Mikroemulsionen in der Zukunft als interessante Reaktionsmedien mit der Option zur magnetfeldinduzierten Separierung genutzt werden könnten.

1 Introduction

1.1 Self-assembly

Self-assembly in water is a phenomenon known for a long time and it is known to be an important driving force leading to fundamental biological mechanisms (e.g., protein folding, cell membranes) and is widely used in applications (washing processes, solubilization, foams, gels, emulsions, food industry). In general the basic building block essential for such structure formation is an amphiphilic molecule (or particle) equipped with a hydrophilic and a hydrophobic part. Models to describe this phenomenon have been developed like the hydrophobic effect or the concept of water structure, which are based on the disruption of the water structure caused by the presence of hydrophobic moieties.[1,2]

An early approach to correlate the aggregation behaviour and the resulting structures with the molecular geometry of the amphiphile is the HLB (hydrophilic-lipophilic balance) value[3] which is related to the molar mass of

the hydrophilic (M_h) and lipophilic (M_l) part of the amphiphilic molecule:

$$HLB = 20 \cdot (1 - \frac{M_l}{M_l + M_h}) \tag{1.1}$$

A disadvantage of this approach is that the amphiphile is characterized disregarding its environment. Another famous model to explain different structures accessible by amphiphilic self-assembly which overcomes this disadvantages is the packing parameter p. This widely used parameter characterizes the amphiphile in a geometrical approach by the volume and shape of its hydro- and lipophilic building blocks which gives the relation between the area a_s occupied by the hydrophilic block and the length (l) and volume (v) of the hydrophobic part given in eq. 1.2.

$$p = \frac{v}{a_s \cdot l} \tag{1.2}$$

The energetically most favorable values for a_s, l and v define the so-called spontaneous packing parameter which is related to a preferred curvature which then defines the expected possible structures as shown systematically in Fig. 1.1. The beauty of this model relies on its simplicity and it is easy to use as relationship between molecular structure of the building blocks and the resulting mesoscopic hierarchical functions. Other widely used parameters based on the same geometrical approach are the HLD (hydrophilic-lipophilic deviation)[4] or the spontaneous curvature[5] which both can be related to p.[6]

A disadvantage of this geometrical approach is that the values for a_s, l and v are difficult to generalize as they are strongly dependent on the surrounding matrix. For example the headgroup spacing is strongly affected by solvation, ionic strength (which screens neighboring ionic headgroups) or co-surfactant (which can compensate frustrated volumes between surfactant headgroup and tail).[7] This makes it obvious that the spontaneous packing parameter cannot be seen as a characteristic of an isolated surfactant but instead is defined for an amphiphile in its actual environment.

Furthermore beside the geometries defined by the spontaneous curvature, more unfavorable headgroup spacings and with that packing parameters can be formed depending on the energy cost for that whereby so-called frustrated

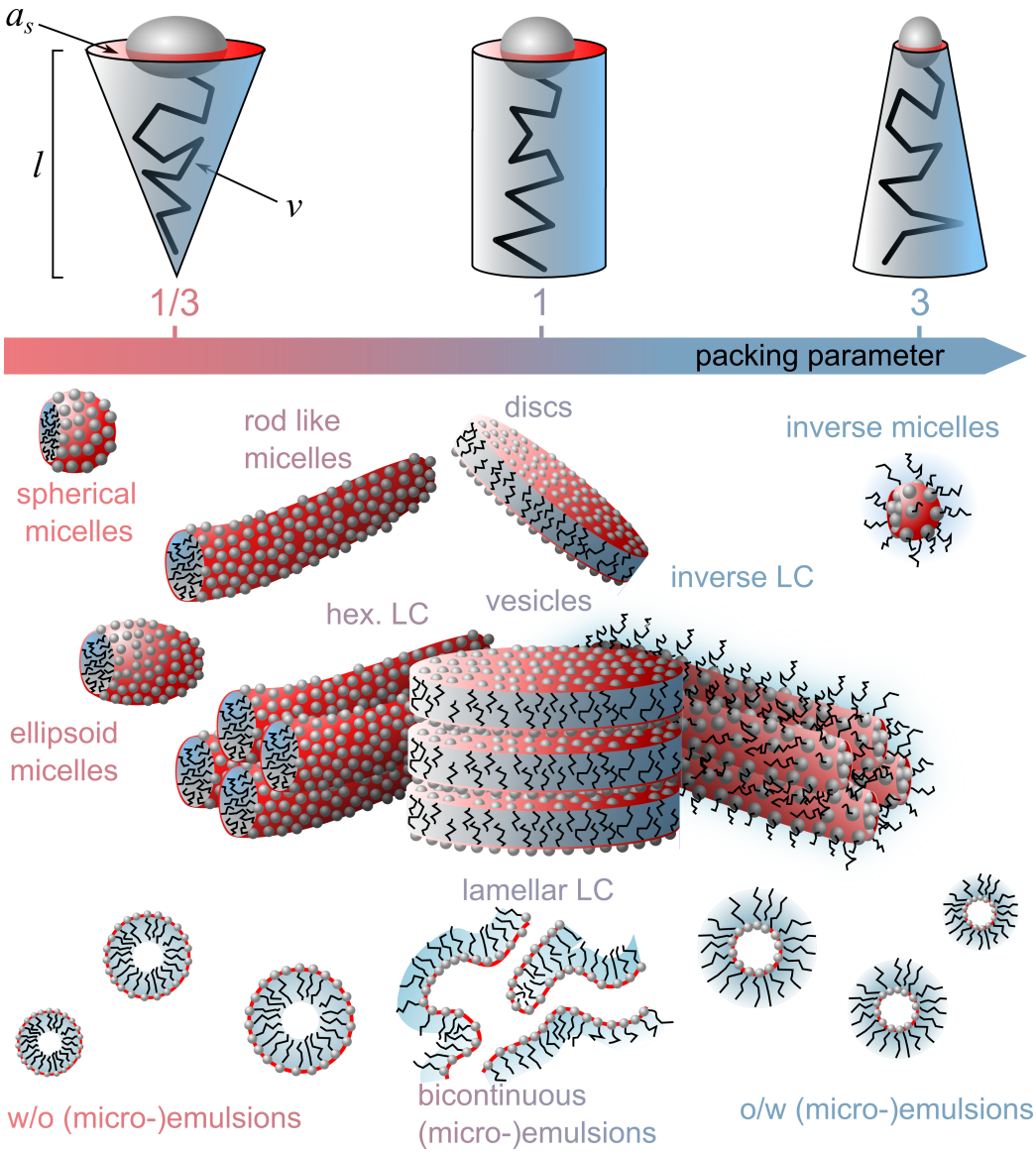

Figure 1.1 Schematic illustration of the geometrical values which define the packing parameter in eq. 1.2 (top) and related mesoscopic structures (bottom).

structures are accessible.[7,8]

1.2 Room Temperature Ionic liquids

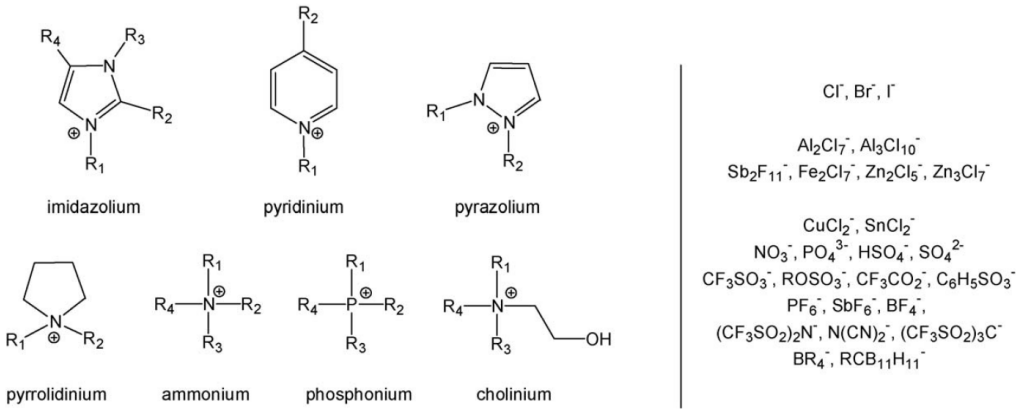

Figure 1.2 Overview of different ions commonly used to design room temperature ionic liquids (RTIL). Reprinted with permission from Olivier-Bourbigou, H.; Magna, L.; Morvan, D. *Appl. Catal., A* **2010**, *373*, 1–56. Copyright 2010 Elsevier.

Room temperature ionic liquids (RTIL) are molten salts with a melting point under or near room temperature (often $\leq 100°C$ is used as an arbitrary definition). This is usually realized by bulky organic ions, which render crystallization difficult. In Fig. 1.2 an overview is given for a few common building blocks used to design RTILs. The possibility of a modular combination of these or others plenty known ions makes a great pool of properties accessible. By varying the used ions or chemical groups within them to formulate RTILs, physical properties can broadly be varied, i. e., values for the viscosity, melting point, glass transition temperature or conductivity can be changed by decades which is nicely summarized in a review by Handy.[9] By introducing functional groups which are known to work as catalysts, the whole RTIL can be transformed into a solvent with an intrinsic catalytic property. This was sucessfully demonstrated for example for Lewis acid catalyst, Henry reaction, or the use of transition metals[10–12]

Many common ions can give a luminescent behaviour to the RTIL[13,14]

partially with remarkable fluorescence quantum yields.[15] Furthermore ionic liquids can be categorized in aprotic and protic ones where the latter ones contain one ore more functional groups with an acidic proton.[9]

Finally by using lanthanides or transition metals in the formulation of RTIL, a paramagnetic behavior can be introduced which was for example demonstrated for iron,[16–18] cobalt[19] or dysprosium[14] in various different ion architectures.

The here discussed fullness of possibilities to vary the solvent's physical and chemical properties which of course can only be briefly touched in this context makes it clear that RTILs are interesting for various applications as solvent, lubricant, additive or catalyst.[20–22]

1.3 Self-assembly in non-aqueous systems

Next to water systems, self-assembly was also found in non aqueous solvents, like glycol, formamide or DMF, which are highly polar liquids and possess a high surface tension (like water and typically higher than 45-50 mN/m)).[23–26] This has made it necessary to generalize the concepts which were originally developed specifically for water systems, from hydro- to solvophobic/-philic amphiphiles. Old concepts had to be extended to this new field, e. g. the above discussed packing parameter can in general be used to describe non-aqueous systems as well but as its quantities (e. g. the headgroup area) are strongly dependent on the surfactant environment, findings are very solvent-specific and have therefore to be newly tabulated for the new environment. As the concept of the hydrophobic effect relies on a disruption of the solvent structure by solvophobic moieties as the driving force for self-assembly, to apply this concept to non aqueous systems it is necessary to be able to quantify the cohesive energy of a solvent. An old definition for this it the Hildebrand solubility parameter (δ_h) which relates the cohesive energy between solvent molecules to its enthalpy of vaporisation (ΔH_{vap}).[27]

$$\delta_h = \sqrt{\frac{\Delta H_{vap} - RT}{v N_A}} \tag{1.3}$$

Here v is the molecular volume and N_A the Avogadro constant. As many ionic liquids have no measurable vapor pressure this quantity is impossible to measure. For this reason the, Gordon parameter is a more suitable concept, which quantifies the solvent quality for self-assembly.[28,29] and is defined by eq. 1.4.

$$G = \frac{\gamma}{\sqrt[3]{vN_A}} \tag{1.4}$$

Here the cohesive energy is alternatively expressed by the surface tension (γ) which is easily empirically accessible.

One quite different class of these water free solvents are ionic liquids (IL) which can again be divided into protic and aprotic ones as already introduced in section 1.2. A very famous class of the latter type consist of imidazolium based ILs.[30–32] and already more than 30 years ago the formation of micelles in ILs by normal surfactants has been observed.[33] Although plenty of studies are already published on self-assembly in IL,[34–37] most of them focused on the comparison of many, often very different systems with a lack in full details. Generally it is by now accepted that surfactant solvation effects play a key role for micelle formation in ILs.[38] Typically it is observed that aggregate formation is less pronounced in ILs, longer chain surfactants are needed for micelle formation and the micelles formed exhibit a higher curvature than they would have in aqueous solution, as for instance seen for classical nonionic alkylethoxy (C_iE_j) surfactants in ethylammonium nitrate (EAN).[39] Such nonionic surfactants typically show much more pronounced tendency for micellisation than equivalent ionic surfactants.[40] The formation of micelles by nonionic surfactants can easily be followed by methods like tensiometry, dynamic light scattering, or small-angle scattering and these methods could also show that for C_4mim based ionic liquids the variation of the counterion can have a pronounced effect on the aggregation behaviour.[41] In a systematic variation of the chain length of C_iE_j surfactants and measuring their *cmc*'s in bmimBF_4 by ^{1}H NMR it has been found that the *cmc* decreases exponentially with the chain length. From the thermodynamic parameters derived it could be concluded that this process is entropy driven in

a similar fashion as for the hydrophobic effect in aqueous solutions but the solvophobic effect in bmimBF_4 is much weaker then in water.[42] That solvophobic effect does not require the formation of a hydrogen bonded network and accordingly is similarly observed in protic and aprotic ILs.[34]

It might also be noted that not only micelles can be formed in ILs but also the formation of liquid crystals,[34,43] vesicles[44–46] or emulsions[47,48] has been reported in some cases. The formulation of microemulsions can also be widely found in literature. This has mostly been done for RTIL replacing water[43,49–57] but it is also possible that the RTIL functions as the hydrophobic component of the microemulsion.[58–60] However, in any case the range of applicable surfactant is much more restricted than in the case of water. The formation of RTIL containing microemulsions has mostly been investigated for bmim based ILs and with nonionic surfactants, where in particular TX-100 has been shown to be quite effective.[50,61] For these nonionic surfactants one can observe as a function of temperature and surfactant concentration in the phase behaviour the classical "Kahlweit-Fisch",[62] as for instance it has been demonstrated for the case of $C_{14}E_4$ and various alkanes.[57] For the case of ionic surfactants one typically has to resort to adding a cosurfactant in order to raise the solubilisation capacity of the hydrocarbon in the IL microemulsion (in this respect microemulsion in polar ILs behave similar to ones in water). For instance this has been successfully done for C_{16}mimCl in bmimBF_4, where the solubilisation of dodecane could be facilitated by the presence of decanol as cosurfactant.[63] Similarly for a system of CTAB in 1-ethyl-3-methylimidazolium hexylsulfate (emim hexSO_4) the solubilisation of toluene could be increased substantially by the use of pentanol as cosurfactant and one observes the percolation phenomenon as in similar microemulsions in water.[64] Here in the droplet regime also an increase of the droplet size with increasing content of IL was observed. Such microemulsions can be quite robust with respect to temperature changes, as demonstrated for the case of C_{16}mimCl in bmimBF_4 with decanol as cosurfactant and dodecane as continuous oil phase, where stability up to 150 °C has been shown,[49] obviously much higher than it can be achieved with similar water based systems.

So, there exists already quite a bit of knowledge regarding the formulation of structured solutions in ILs but the situation is in general more complex than in water as it depends also subtly on the precise type of IL employed. Nonetheless, up to now systematic information regarding the aggregation process of surfactants in ILs is still far from being satisfactory and deducing general information is difficult (as depending on its building blocks the properties of ILs scatter over a very broad range).

1.4 Aim of this work

The aim of this work is to get a deeper insight into the mechanisms and driving forces of surfactant self-assembly. For that purpose self-assembly is not studied in water but in a nonaqueous model system based on a magnetic room temperature ionic liquid (MRTIL) as solvent combined with an ionic surfactant. This gives the possibility by a variation of the molecular structure of both solvent and surfactant to systematically vary its properties (i. e. attraction potentials, solvophobicity/-philicity) and by that extract information on the correlation between these parameters and the driving force for self-assembly. It will be made use of a broad palette of complementary methods to guarantee a well balanced and reliable view on the system, nonetheless small angle neutron scattering will be a central method.

In a first step a detailed picture of this model system and its phase behavior and with that ability to form structures as micelles, microemulsions and liquid crystals will be investigated. By this and by comparing with other (classical aqueous) systems, qualitative and quantitative information on self-assembly will be derived.

By choosing an ionic liquid with paramagnetic properties as solvent, this opens the possibility to also investigate the magnetic behavior of the resulting mesoscopic structures. This will include first the proof of principle if a paramagnetic behavior is still present in these structures and then an investigation on how and if an external magnetic field can trigger the systems stability, shape and orientation.

Next to the more theoretical insights in the origin and driving force of

self-assembly which are already of high value on its own, the work can as well point to some potential future application. As already mentioned above there are already plenty of known applications for ionic liquids (e. g as catalyst or custom build solvent) just as it is known for mesoscopic systems (e. g. as nano-sized containers, structured reaction media, shaping template). By a combination of those both one opens up the possibility to an extended field of application. Examples are mesoscopic systems with a temperature range beyond the limit of 0–100 °C caused by water or microemulsions as anhydrous reaction media. In particular the MRTILs used in this study offer by their contain of the transition metal ion iron the possibility to function as media for catalysis or as solvent which can be manipulated by an external magnetic field interesting e. g. for separation chemistry.

2

Methods and Materials

2.1 Used Compounds

In this study 1-alkyl-3-methylimidazoliumtetraferrates ($C_i$mimFeCl_4) with different chain lengths (i=2, 4, 6) were used as solvents. This ionic liquids have, due to its iron containing anion, a paramagnetic behavior. As listed in table 2.1 the calculated Gordon parameters (see eq. 1.4) for all three solvents with different chain lengths are far lower than highly structured water ($2.7\,J/m^3$) but still above $0.5\,J/m^3$, the border under which no self-assembly was found till now.[34] Accordingly these solvents have potential to function as matrix for self-assembly but a lower driving force compared to water is expected and a graduation with respect to the chain length.

As surfactant 1-alkylimidazoliumchlorides ($C_j$mimCl) with different chain lengths (j=12, 14, 16, 18) were used. By reason of its very similar head group with respect to the solvent cation, it is expected to be well soluble and with that the imidazolium group function as the solvophilic part of the molecule.

Table 2.1 Summarized properties of the MRTIL used as solvent in this study. v is the molecular volume calculated from the density, $G = \frac{\gamma}{\sqrt[3]{vN_A}}$ is the Gordon parameter and T_m is the melting temperature.

$C_i$mimFeCl$_4$	$\frac{\rho(25\,^\circ\mathrm{C})}{\mathrm{gcm}^{-1}}$	$\frac{\gamma(25\,^\circ)}{\mathrm{mNm}^{-1}}$	$\frac{v}{\mathrm{nm}^3}$	$\frac{G}{\mathrm{Jm}^{-3}}$	$\frac{T_m}{^\circ\mathrm{C}}$
2	1.44	52	0.368	0.86	16
4	1.36	47	0.411	0.75	-88[a]
6	1.30	42	0.466	0.64	-86[a]

[a] Glass transition, taken from literature[65]

The structures of solvents and surfactants are given in Fig. 2.1.

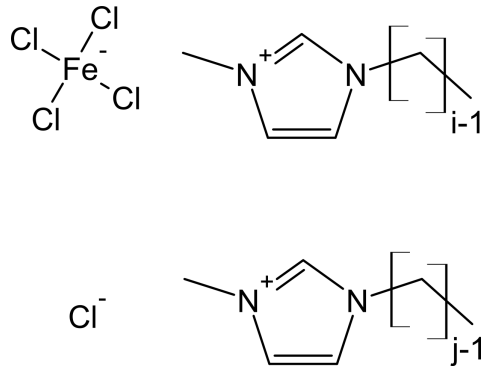

Figure 2.1 Structures of the used compounds. **Top:** 1-alkyl-3-methylimidazoliumtetraferrates ($C_i$mimFeCl$_4$ with i=2,4,6) as solvent. **Bottom:** 1-alkyl-3-methyimidazoliumchlorides ($C_j$mimCl with j=12,14,16,18) as surfactant.

The ionic liquids were synthesized analogously as described for the butyl-derivative in literature[16] C_{14}mimCl, C_{16}mimCl and C_{18}mimCl were synthesized as described in reference.[63] C_{12}mimCl was a gift from Prof. Werner Kunz (Universität Regensburg). Its synthesis is documented in literature.[66] The quality of the resultant materials was verified by NMR, ESI-MS and DSC.

Further used chemicals (oils and alcohols) to formulate microemulsions and binary mixtures were used as purchased. A summary is given in table 2.2.

Table 2.2 Suppliers and grades of oils and alcohols as used to formulate microemulsions and binary MRTIL/alcohol mixtures.

oil	supplier	grade/%
hexane	Fluka	98.5
octane	Fluka	99.5
decane	Fluka	98
isooctane	Fluka	99.8
cyclohexane	Sigma-Aldrich	99
alcohol	supplier	grade/%
1-propanol	Merck	99.8
1-butanol	Merck	99
1-pentanol	Fluka	99.5
1-hexanol	Sigma-Aldrich	99
1-heptanol	Merck	99
1-octanol	Sigma-Aldrich	99
1-decanol	Merck	99
1-dodecanol	Fluka	98
3,7-dimethyloctanol	Fluka	98
geraniol	Sigma-Aldrich	98
cis-nerolidol	Fluka	98
2-butoxyethanol	Sigma-Aldrich	99

2.2 Recording phase diagrams by visual observation

2.2.1 Microemulsion systems

The pseudo ternary phase diagrams were recorded at a constant temperature of 24±0.5 °C. Mixtures of different ratios between cyclohexane and surfactant/cosurfactant were titrated with C_4mimFeCl_4. In all cases the molar ratio of $C_j$mimCl/decanol was 1:2. The pseudo ternary phase diagrams to determine the cosurfactant and oil influence were recorded by the same titration method but starting with a constant mass ratio of 86.4% cyclohexane in all samples. For the cosurfactant dependency the ratio between C_{16}mimCl and

alcohol was then varied. The phase boundary was detected visually. The added relative amount of C_4mim$FeCl_4$ is calculated with respect to the final mixture.

Kahlweit fish diagrams[62] were recorded at 24±0.1 °C by titrating samples with a volume ratio of $C_i$mim$FeCl_4$/oil=1:1 and different surfactant concentrations with decanol or by repeatedly adding of solid surfactant. The added amounts were measured gravimetrically. For details see the appendix B. It should be mentioned that for the system C_2mim$FeCl_4$/C_{18}mimCl at 24 °C a precipitation of solid surfactant was observed after some time. As it was possible to prevent this by rising the temperature by 1-2°C and the phase diagram showed nearly no temperature dependency in this range (the fishtail-point was shifted by ≈ 2 wt% between 24 and 45 °C), this was not considered furthermore.

2.2.2 Binary MRTIL/alcohol mixtures

Different C_4mim$FeCl_4$/alcohol mixtures, sealed in glass ampoules together with a magnetic stirrer were heated up under stirring (0.5 °C-steps, including an appropriate holding time of several minutes). The sample clearing was detected visually and interpreted as the phase boundary.

2.3 Differential scanning calorimetry (DSC)

Measurements of binary MRTIL/surfactant mixtures as presented in chapter 3 were performed on a multi-cell calorimeter (TA Instruments MC DSC) at heating/cooling rates of 0.2 °C/min. More concentrated samples were before homogenized by alternating mixing with a spatula and heating several times. Results were extracted after observing at least two equivalent runs. Phase transition temperatures (peak position) and transition heats were read out from the heating cycles after background (unloaded cell) subtraction. For binary MRTIL/alcohol mixtures as presented in chapter 4.1 the phase boundary was read out from cooling cycles performed at rates of 0.5 °C/min.

2.4 Conductivity

Conductivity titration was done at a temperature of $24.0 \pm 0.1\,^{\circ}\mathrm{C}$ with a home-build Pt-electrode connected to a Methrom 712 conductometer at 2.4 kHz, starting with an oil rich microemulsion sample by stepwise addition of an oil free sample with a syringe.

2.5 Magnetic susceptibility

Magnetic susceptibility measurements were done at 300 K with a MPMS (Quantum Design, located at the Laboratory for Magnetic Measurements, HZB). Samples were placed in a home-made vacuum-sealed sample chamber and scanned in a range from -5 to 5 Tesla. The empty cell signal was subtracted from each measurement.

2.6 Viscosity

Viscosity measurements were done at $(25.0 \pm 0.1)\,^{\circ}\mathrm{C}$ with a micro-Ostwald viscosimeter (Ic or IIc, SI Analytics, Mainz). The obtained kinematic viscosity ν was multiplied with the density ρ of the same sample to calculate the dynamic viscosity η.

$$\eta = \rho \cdot K \cdot t = \rho \cdot \nu \tag{2.1}$$

Here t is the retention time needed for a defined sample volume and K is the capillary constant. For each sample at least three measurements were done. The deviation of the retention times gives the error for the viscosity and was $\leq 0.3\,\%$.

2.7 Small angle scattering

As small angle scattering relies on a complex and quite voluminous theory, for a better understanding it is referred to textbooks found in literature.[67,68]

In the following only the basic principles are discussed. An ideal scattering experiment is represented in Fig. 2.2 were an incoming wave, represented by the vector $\vec{k_i}$, strikes a scattering center in the sample which produces a scattered wave ($\vec{k_s}$) dependent on the angle θ. For purely inelastic scattering (which will be the assumption throughout this work) the energy of incoming and scattered wave is equal ($|\vec{k_i}| = |\vec{k_s}| = \frac{2\pi}{\lambda}$) which leads to the definition of the magnitude of the scattering vector q given by eq. 2.2.

$$q = |\vec{q}| = |\vec{k_i} - \vec{k_s}| = \frac{4\pi}{\lambda} \sin \frac{\theta}{2} \tag{2.2}$$

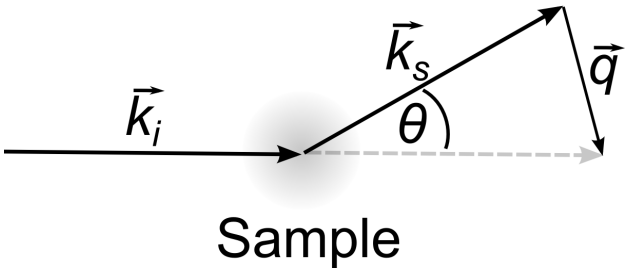

Figure 2.2 Schematic representation of a scattering experiment: The explanations are given in the main text.

For an assembly of scattering centers in a sample, the amplitude $A(q)$ of the elastic scattered wave is furthermore related to the Fourier transform of the scattering length density function $\beta(r)$, which defines the relative position of the scattering centers to each other.

$$A(q) = \int\int\int \beta(r) e^{iqr} \mathrm{d}^3 r \tag{2.3}$$

Eq. 2.3 gives the relation between the inverse length scale q and characteristic distances $r = 2\pi/q$ within the sample. As neutron and X-ray scattering experiments give access to a q-range of typically 0.01–8 nm^{-1}, this defines that structures of one to a few hundred nanometer sizes are visible by this technique. The measurable scattering intensity $I(q)$ is defined as

$$I(q) = \left\langle \frac{A(q)A^*(q)}{V} \right\rangle \propto \left| \int\int\int \beta(r) e^{iqr} \mathrm{d}^3 r \right|^2 \tag{2.4}$$

which is the squared scattering amplitude per sample volume V, averaged over time, all possible configurations and orientations. Its amplitude is defined by the scattering invariant Q_{inv}.

$$Q_{inv} = \int_0^\infty I(q) q^2 \, \mathrm{d}q \tag{2.5}$$

To solve eq. 2.4, assumptions have to be made how the sample is structured which will define $\beta(r)$ and Q_{inv}. Depending on the model it is oftenly useful to split the intensity into two terms, called the form factor $P(q)$ and the structure factor $S(q)$ where the first accounts for the scattering intensity originated by one single object and the latter one by the interaction of an assembly of several of these objects.

$$I(q) \propto P(q) \cdot S(q) \tag{2.6}$$

In this work small angle scattering experiments were done using neutrons (SANS) and X-rays (SAXS) as incoming beam.

2.7.1 SANS

For better contrast the microemulsion samples were prepared with D12-cyclohexane (For consistency mass fractions in the phase diagrams were recalculated to H12-cyclohexane with the same volume.) and for the measurements placed in cuvettes (Quarz, Hellma) of 1 mm thickness. To extract the scattering intensity purely originated by the sample, the intensity, measured at each pixel (i) of the detector plate at a given sample to detector distance (d), has to be corrected due to eq. 2.7.

$$I_{i,d} = \frac{\frac{I(S)_{i,d}}{T(S)_{i,d}} - \frac{I(BG)_{i,d}}{T(BG)_{i,d}}}{\frac{I(R)_{i,d}}{T(R)_{i,d}} - \frac{I(BG)_{i,d}}{T(BG)_{i,d}}} \cdot scaling\ factor \tag{2.7}$$

Here T is the transmission, S accounts for the sample, BG for the background which is the empty cell and R for a reference. As reference H_2O placed in a similar cuvette as for the sample measurements was used. As H_2O is expected to have a constant scattering over all angles it corrects in-

equalities in the detector pixel sensitivity. Additionally it brings the data to absolute scale when using the correct scattering cross section for water as the scaling factor. For each sample to detector distance $I_{i,d}$ was radial averaged and the data for different distances was merged to result the final q dependent 1D-spectra. When not stated differently, this data reduction was done with BerSANS[69] and fitting of the resulting 1D-spectra with SASfit.[70] For all measurements the samples were placed in a temperature controlled sample holder. As the SANS data were recorded at different facilities, their special characteristics are listed in the following.

V4 at HZB (Berlin)

An incoming beam of 4.6 Å wavelength at two detector distances (1.3 and 6 m with collimation at 2 and 8 m, respectively) was used, resulting in a q-range of $0.09\,\mathrm{nm}^{-1} \leq q \leq 6.5\,\mathrm{nm}^{-1}$. The scattering of water was used to correct the detector efficiency and to bring the data to absolute scale. Under these conditions data were recorded for microemulsion contrast variation as presented in Fig. 5.14 (except the system C_2mim$FeCl_4$/C_{18}mimCl).

D11 at ILL (Grenoble)

An incoming beam of 6 Å wavelength and a collimation length of 8 m was used. Scattered neutrons were recorded with a 2D-detector for sample-to-detector distances of 8 m and 1.2 m resulting in an observed q-range of $0.09\,\mathrm{nm}^{-1} \leq q \leq 5.12\,\mathrm{nm}^{-1}$. Incoherent scattering of water was used to correct the detector efficiency and to bring the data to absolute scale. Data reduction was done with LAMP.[71] Under these conditions data were recorded for microemulsions as shown in the appendix B.4.

SANSII at PSI (Villigen)

An incoming beam of 6 Å wavelength was used. Scattered neutrons were recorded for sample-to-detector distances of 1.2 m and 5 m resulting in an observed q-range of $0.09\,\mathrm{nm}^{-1} \leq q \leq 3.04\,\mathrm{nm}^{-1}$. Incoherent scattering of water was used to correct the detector efficiency. The data were brought to

absolute scale by comparing with the scattering intensity of glassy carbon[72] for a sample-to-detector distance of 5 m. Under these conditions data were recorded for binary MRTIL/surfactant mixtures as presented in chapter 3.

SANSI at PSI (Villigen) with cryo magnet

As sample environment a cryomagnet (MA11, Oxford Instruments), which allows to generate a horizontal magnetic field up to 8 T perpendicular to the incoming beam, was used. An incoming beam of 5 Å wavelength was used. Scattered neutrons were recorded for sample-to-detector distances of 2 m, 8 m and 18 m resulting in an observed q-range of $0.03\,\mathrm{nm}^{-1} \leq q \leq 2.1\,\mathrm{nm}^{-1}$. The q-range is shortened due to a partial screening of scattered neutrons by the magnet coils at high angles. Incoherent scattering of water was used to correct the detector efficiency.

To extract information about the anisotropy of scattering data as presented in chapter 5.3, the program SASET,[73] version 7.01.30, was used. From the 2D-detector image recorded at 2 m distance, a radial segment of $1.25\,\mathrm{nm}^{-1} \leq q \leq 1.43\,\mathrm{nm}^{-1}$ was analyzed to extract three different values for the anisotropy:

1. The principal component analysis (PCA),

2. the alignment factor, defined as

$$A_f = \frac{\int_0^{2\pi} I(q,\varphi)\cos(2\varphi)\mathrm{d}\varphi}{\int_0^{2\pi} I(q,\varphi)\mathrm{d}\varphi} \tag{2.8}$$

   with φ as the azimuthal angle,

3. and the order parameter S, defined as

$$S = \langle P_2(\cos\varphi)\rangle_I / \langle P_2(\cos\varphi)\rangle_{I^m} \tag{2.9}$$

$$\langle P_2(\cos\varphi)\rangle_I = \frac{\int_0^{\pi} I(q,\varphi)P_2(\cos\varphi)\sin\varphi\mathrm{d}\varphi}{\int_0^{\pi} I(q,\varphi)\sin\varphi\mathrm{d}\varphi} \tag{2.10}$$

   with $P_2(\cdot)$ as the second-order Legendre polynomial. It should be mentioned that in Fig. 5.24 $\langle P_2(\cos\varphi)\rangle_I$ is plotted instead of the order pa-

rameter because the normalization value $\langle P_2(\cos\varphi)\rangle_{I^m}$ for a perfectly aligned sample is not known.

For details it is recommended to use the given literature and the software documentation.[73]

Paxy at LLB (Saclay)

Scattered neutrons were recorded for sample-to-detector distances of 5 m and 1 m with an incoming beam of 4 Å resulting in an observed q-range of $0.1\,\mathrm{nm}^{-1} \leq q \leq 6\,\mathrm{nm}^{-1}$. Additionally for the short sample-to-detector distance the detector tube was shifted by an angle of 13° relative to the beam pathway to extend the observation window up to $q = 8.35\,\mathrm{nm}^{-1}$. Incoherent scattering of water was used to correct the detector efficiency and to bring the data to absolute scale. Under these conditions data were recorded for binary cyclohexane/decanol mixtures as presented in chapter 4.2, contrast variation for the system C_2mim$FeCl_4$/C_{18}mimCl (Fig. 5.14) and curves presented in Fig. 5.13.

2.7.2 SAXS

Small angle X-ray scattering (SAXS) experiments were performed on an Anton Paar SAXSess using a CCD-Kamera as detector. Samples were prepared as described for DSC and measured in sealed quarz capillaries (Hilgenberg, outer diameter 1.0 mm, wall thickness 0.01 mm).

2.8 Surface tension

Surface tension measurements were done by the pendant drop method. This method bases on the idea that the shape of a pendant drop is defined by the force equilibrium between the surface tension (γ), expressed by the Young-Laplace law, and the weight, resulting in eq. 2.11.

$$\gamma = \frac{1}{2}\left[\left(\frac{1}{R_{A1}} + \frac{1}{R_{A2}}\right)_A - \left(\frac{1}{R_{B1}} + \frac{1}{R_{B2}}\right)_B\right]\rho g h \qquad (2.11)$$

Here g is the acceleration due to gravity, ρ the density difference between drop and environment and R_i are the radii to define the curvatures at points A and B placed along the droplet surface with a difference h in height. Measurements were done on a Contact angle System OCA 15plus (Dataphysics) by using a needle with an outer diameter of 1.83 mm (NE45, Krüss) and a homebuild temperature control cell. All samples were measured with different droplet sizes and values were extrapolated to large droplet volumes to cancel out effects arising from needle tilting. The droplet profile was determined by the instrument software and surface tension values were corrected by the calculated sample density which is in good agreement with experimental values measured with Anton Paar densiometer. For details see Fig. S6 in the ESI†.

2.9 Density

The density was measured with an Anton Paar density-meter (DMA 4500). Calibration was done with deionized water. For the density ρ_{mix} of an ideal mixture (constant molecular volume) the following expressions are valid:

$$\frac{1}{\rho_{mix}} = \frac{\sum V_i}{\sum m_i} = \sum \frac{\phi_{m,i}}{\rho_i} \tag{2.12}$$

$$\rho_{mix} = \frac{\sum m_i}{\sum V_i} = \sum \phi_i \rho_i \tag{2.13}$$

With m_i, V_i, $\phi_{m,i}$, ϕ_i and ρ_i being the mass, volume, mass fraction volume fraction and density of the pure component i, respectively.

2.10 Polarized microscopy

Polarized microscopy for identification of liquid crystal (LC) phases was done on a Zeiss microscope (12.5x/0.25 planchromat pol objective) using the same samples prepared for DSC measurements. Temperature scans (1 °C/min with a linkam TMS91 hot stage) and photographs (1 photo/min with a Canon EOS

5D camera) were done remote controlled with home-build software.

2.11 Emulsion Stability

The magnetic field effect on the emulsion stability as presented in section 5.3 was done with a home-build temperature control cell at $(25.0 \pm 0.3)\,^{\circ}\mathrm{C}$. A magnetic field was applied by a Brucker magnet B-E15. The field profile was measured with a Brucker B-H11D Hall probe.

3

Binary Mixtures: MRTIL/Surfactant

As this study concentrates on a selected pool of molecular architectures, in this chapter just a variation of the alkyl chain of the cationic surfactant is investigated, but giving for these a detailed view over a large temperature range and the full concentration range using different complementary methods. For that purpose results of self-assembly in 1-ethyl-3-methylimidazolium tetrachloroferrate (C_2mimFeCl_4) and 1-butyl-3-methylimidazolium tetrachloroferrate (C_4mimFeCl_4) as solvents are presented. With the surface tension of the pure solvents Gordon parameters of 0.86 and 0.75 J/m^3 (for C_2mimFeCl_4 and C_4mimFeCl_4, respectively) can be calculated. This is far lower than highly structured water (2.7 J/m^3) but still above 0.5 J/m^3, the border under which no self-assembly was found till now.[34]

In order to study the aggregation conditions in these MRTILs in a systematic fashion we choose cationic surfactants with imidazolium chloride as head group, which has a high structural similarity to the solvent. Low interaction potentials and good solubility for this part of the molecule is expected.

As solvophobic part of the molecule, aliphatic hydrocarbon chains (with 14, 16 or 18 carbon atoms) are used because hydrocarbon oils with six and more C-atoms were observed to be insoluble in C_4mimFeCl_4 at the investigated temperature. Accordingly alkylimidazolium chlorides ($C_j$mimCl, with j=14, 16, 18) are expected to be suitable as amphiphiles in our solvent. It might be noted that for such $C_j$mimCl surfactants calorimetric investigations have shown negative enthalpies of micellization in EAN, while they are positive for micellization in water at not too high temperatures.[74–76]

3.1 Results

As the aim of our work was the systematic comparison of the aggregation behaviour of alkylimidazolium chlorides of different alkyl chain length in C_2mimFeCl_4 and C_4mimFeCl_4 as representative magnetic room temperature ionic liquids (MRTIL), we first made a determination of the temperature dependent phase behaviour. Based on that the individual phases were assigned structurally by polarized microscopy and SAXS. The *cmc* (critical micelle concentration) was determined by surface tension measurements and the structural details of the aggregates were deduced from SANS experiments.

3.1.1 Temperature dependent binary phase diagrams

Fig. 3.1 shows binary phase diagrams for all three surfactants in both C_2mimFeCl_4 and C_4mimFeCl_4 as solvent which were constructed from DSC and polarized microscopy measurements. As a common observation for all systems we found a phase boundary separating a multi-phase region at lower temperatures from homogeneous phases formed at higher temperatures which increases in size with the surfactant concentration. While at low concentrations the homogeneous phase is an (optically) isotropic phase, a birefringent liquid crystalline (LC) region was found at high surfactant concentration, showing typical textures for lamellar structures (see inset of Fig. 3.8). The LC-lamellar phase is directly connected with the pure surfactant isopleth (and not separated by another isotropic one-phase region) as known for sur-

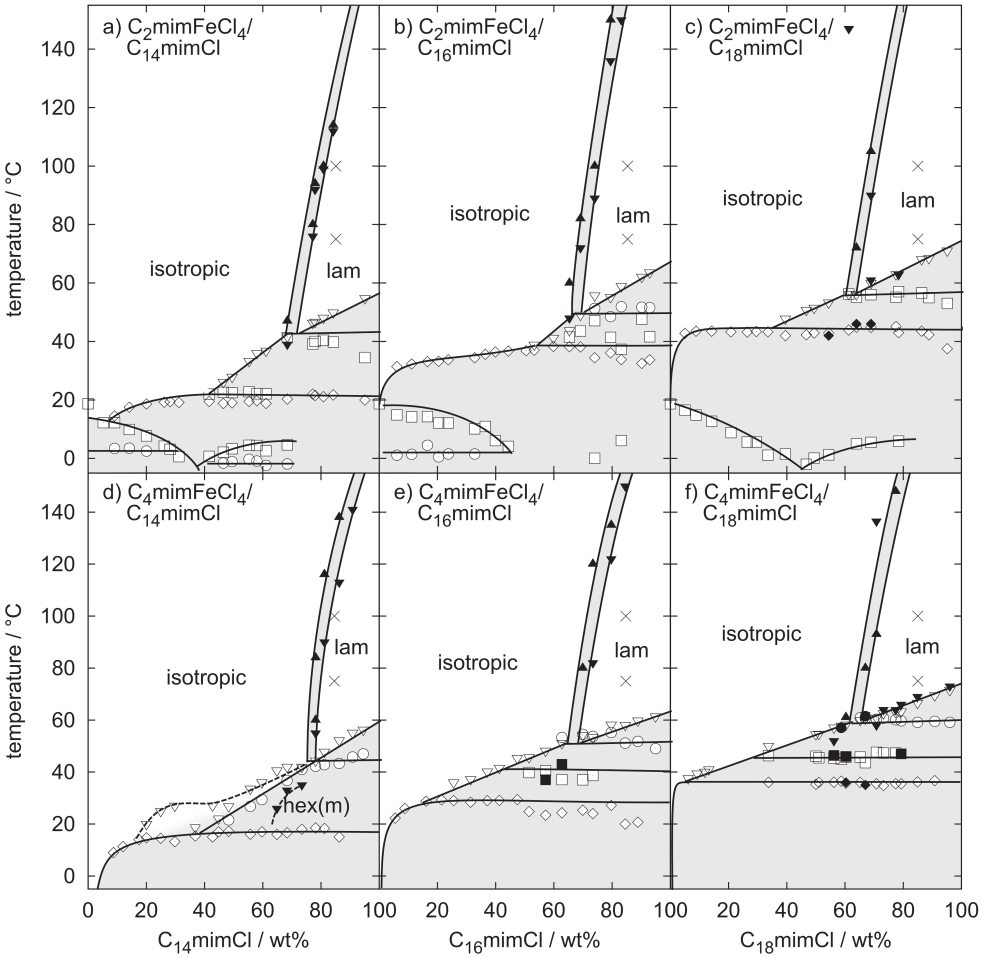

Figure 3.1 Temperature dependent phase diagrams for binary mixtures of C_{14}mimCl (left column), C_{16}mimCl (middle column) and C_{18}mimCl (right column) mixed with C_2mimFeCl$_4$ (top row) or C_4mimFeCl$_4$ (bottom row). Open symbols are transitions observed by DSC, filled symbols are transitions observed with polarized microscopy. Different symbol shapes are used to group similar transitions to enhance the clearness. Crosses give the position of samples analyzed by SAXS (see Fig. 3.8). Lines give a guide to the eye for equilibrium (straight) and metastable (broken) transitions. Multi-phase regions are displayed as gray area (it might be noted that upon approaching 100 wt% there will be single-phase regions again, but these regions are experimentally difficult to access and were not in the focus of our investigation).

factants having a thermotropic behavior.[77] A more detailed structural investigation of the LC-phase can be found in section 3.1.3. Beside the lamellar phase no other mesophases like cubic or hexagonal phases were found in equilibrium. This observation fits to earlier studies on cationic surfactants in IL.[78] Only for the system C_{14}mimCl/C_4mimFeCl$_4$ a metastable hexagonal phase was observed by polarized microscopy during cooling cycles (for details see Fig. A.12 in the appendix).

Focussing on the multi-phase region a Krafft discontinuity (at middle concentrations) or Krafft boundary (at lower concentrations) was observed which is comparable to findings for water systems.[77] A characteristic dropping down while going to lower concentrations, known as the Krafft knee can be found which is much more pronounced and at higher concentrations for the shorter chain surfactant systems which gives already a rough estimate for the critical micellization concentration (*cmc*). Analyzing the sum DSC-integral over all transition peaks for each sample gives enthalpy-values of around 5-6 kJ/mol per CH_2 unit of the surfactant chain (see table A.4, Fig. 3.2), a value very common for melting alkyl chains.[79,80] With that the multi-phase region can be interpreted as solid surfactant in equilibrium with monomeric, micellar, or liquid crystal phases, separated by isothermal phase boundaries.

The system C_{14}mimCl/C_4mimFeCl$_4$ shows by DSC an additional metastable region at low surfactant concentrations which can be interpreted by as due to a kinetically hindered transport of MRTIL molecules towards surfactant crystals. The reason why this is only observed here could be a coincidence of high solvent viscosity, low temperature and relatively high surfactant concentrations compared to the other systems which favors a slow transport kinetics. For C_2mimFeCl$_4$ as solvent additional transitions are observed due to the solvent's higher melting point of 18 °C showing a freezing-point depression by adding surfactant. C_4mimFeCl$_4$ has a much broader liquid range down to a glass transition at -88 °C[65] and therewith has no such transitions within our observation window. The solid surfactant phase could be dry surfactant or any kind of solvated crystals. Am indicator for the latter could be the missing transitions at high surfactant concentrations/low temperatures

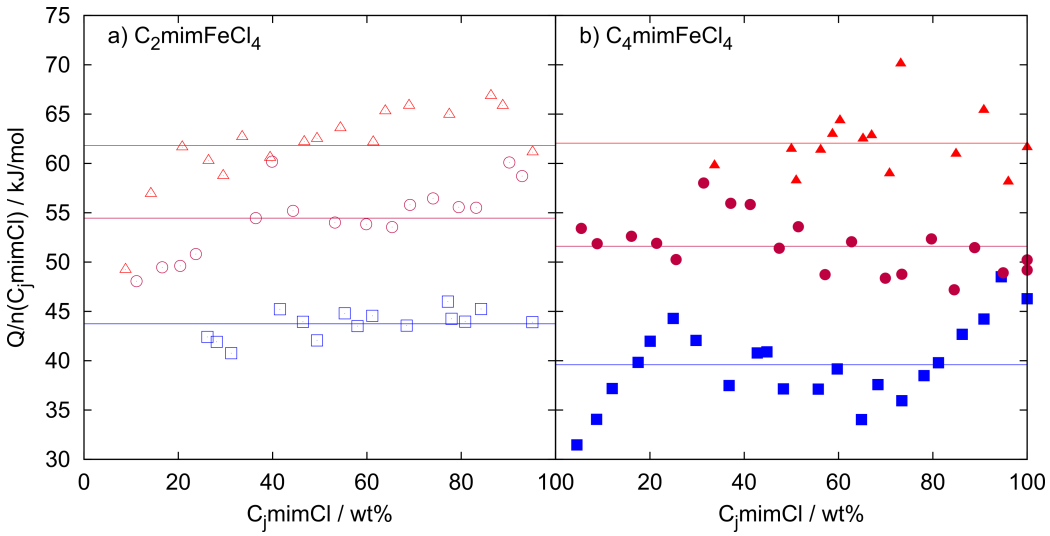

Figure 3.2 Integral over all peaks (excluding the low temperature peaks for the C_2mimFeCl$_4$-system originated by the solvent melting point, see Fig. 3.1) extracted from DSC-curves given in the appendix A.4 and normalized by the surfactant concentration for C_{14}mimCl (squares), C_{16}mimCl (circles) and C_{18}mimCl (triangles). The lines give the mean values from whose mean distance the heat per surfactant CH_2-unit can be deduced as $dQ/d(CH_2)\approx$5-6 kJ/mol, a value common for alkyl chain melting.

(but this could also be interpreted by difficulties to reach equilibrium in a kinetically slow solid→solid transition). The pure surfactant is known to have different solid structures (with the triclinic double bilayer as the most stable one) whose appearance and transformation strongly depends on thermal history and the amount of additional solvent.[81] Nevertheless it is difficult to elucidate this issue and this is not the subject of the actual study.

In both solvents the same trend can be observed, i. e., with longer surfactant chains the lamellar region is getting wider, shifted to lower concentrations, the Krafft knee is shifted to lower concentrations which allows a first estimation in amphiphilic strength in the order C_{18}mimCl>C_{16}mimCl> C_{14}mimCl as to be expected. An extraction of characteristic values is given in table 3.1 and will be furthermore discussed in section 3.2. In Fig. 3.3 the position of the triple point at which lamellar LC, isotropic solution and solid surfactant are in equilibrium is plotted and shows exemplary the men-

tioned dependency on surfactant chain length. The temperature increases with chain length as the whole phase diagram is shifted to higher temperatures while the mass fraction of surfactant ($\phi_{m,LC}$) decreases as the LC region is extended to lower surfactant concentrations.

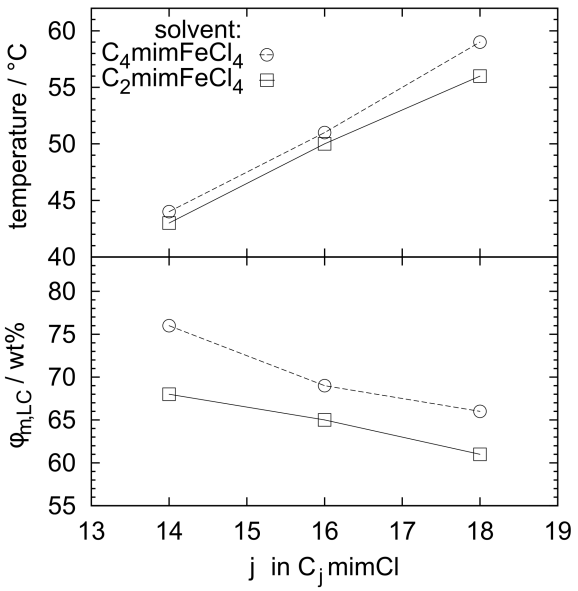

Figure 3.3 Position by means of temperature (top) and composition (bottom) of the triple point at which lamellar LC, isotropic solution and solid surfactant are in equilibrium as a function of the surfactant chain length. Values are extracted from Fig. 3.1

3.1.2 Surface tension measurements

As surface tension is a quantity that is intimately linked to the aggregation behaviour of amphiphilic systems it was also studied for our systems. It can be noted that the surface tensions of the pure ILs are 50 and 45 mN/m for C_2mimFeCl$_4$ and C_4mimFeCl$_4$, respectively, substantially lower than that of water and at the border where one may still expect the formation of aggregates. A first estimate of the *cmc* can be inferred from DSC measurements as discussed in section 3.1.1. To investigate the herein presented system on its aggregation behavior with common methods known from water systems

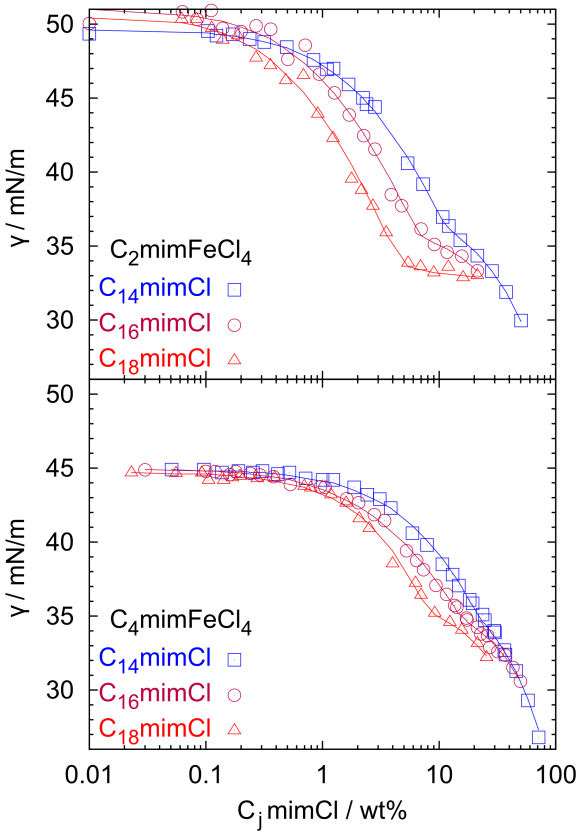

Figure 3.4 Surface tension measurements at 45 °C for binary mixtures of C_{14}mimCl (cubes), C_{16}mimCl (circles) and C_{18}mimCl (triangles) in C_2mimFeCl$_4$ (top) or C_4mimFeCl$_4$ (bottom) as solvent. Lines are fits performed with eq. 3.1a.

raises some practical problems: As UV and visible light is strongly absorbed by the iron ions[82] a very low transmission prohibits a *cmc* determination by light scattering, turbidity measurements or fluorescence/ dye uptake methods. Its high conductivity (20 and 9 mS/cm for C_2- and C_4mimFeCl$_4$)[65] makes the conductivity method unfavorable. Expected *cmc* values at relatively high concentrations give distractingly high diluting enthalpies for the isothermal titration calorimetry (ITC) method.

Accordingly we turned to surface tension measurements and Fig. 3.4 shows results as a function of surfactant concentration in C_2mimFeCl$_4$/$C_j$mimCl

(top) and C_4mimFeCl_4/$C_j$mimCl (bottom) binary mixtures. All measurements were done at 45 °C to have monophasic samples for each system.

Adding surfactant decreases the surface tension and a (more or less pronounced) discontinuity leading to a plateau (or less steep slope, depending on amphiphilicity) in surface tension vs. concentration can be observed. Qualitatively two trends can be noticed: Shortening the solvent's alkyl chain or lengthening the surfactant's one leads to a more pronounced knee which is located at lower concentrations. This can be interpreted as an enhancement in amphiphilic strength of the system by these molecular changes which is congruent with observations in section 3.1.1.

Compared to strong amphiphiles in water, which usually give a very sharp transition between the surface tension decrease and the plateau (which makes the extraction of the *cmc* value at this knee straightforward) in our system the finding is less clear. To extract quantitative information from the data points nonetheless, surface tension curves were fitted with a modification of the Szyszkowski equation:[83,84]

$$\gamma = \gamma^0 - RT \cdot \Gamma \cdot \ln\left[1 + K_1 \cdot \phi_{m,b} \cdot f\right] \tag{3.1a}$$

$$f = \exp\left(b \cdot \phi_{m,tot}\right) \tag{3.1b}$$

$$\phi_{m,tot} = K_2 \cdot N \cdot \phi_{m,b}^N + \phi_{m,b} \tag{3.1c}$$

with the monomer mass fraction in equilibrium ($\phi_{m,b}$) calculated by a simple mass action model (N[monomers] $\rightleftharpoons$ [Micelle], leading to eq. 3.1c). $\phi_{m,tot}$ is the total surfactant mass fraction. To correct the nonideal behaviour especially at high concentrations a coefficient f was introduced expressed by a simple exponential function (eq. 3.1b). This could be interpreted as an activity coefficient as it has a similar form as found for activity coefficients in mixed salt solutions.[85] Fit results are listed in table A.5 and in Fig. 3.5 the concentration dependent evolution of $\phi_{m,b}$ and $\phi_{m,mic}$ vs. $\phi_{m,tot}$ is plotted. From that the initial appearance of micelles was interpreted as cmc_γ (for details see appendix A). Apparently eq. 3.1a is describing the experimental situation rather well and the extracted *cmc* values describe a quantitative

trend as a function of the surfactant chain length which confirm the trend observed with the other methods. This model also yields that at concentrations above the *cmc* there is still a moderate increase of the molecularly dissolved surfactant (Fig. 3.5).

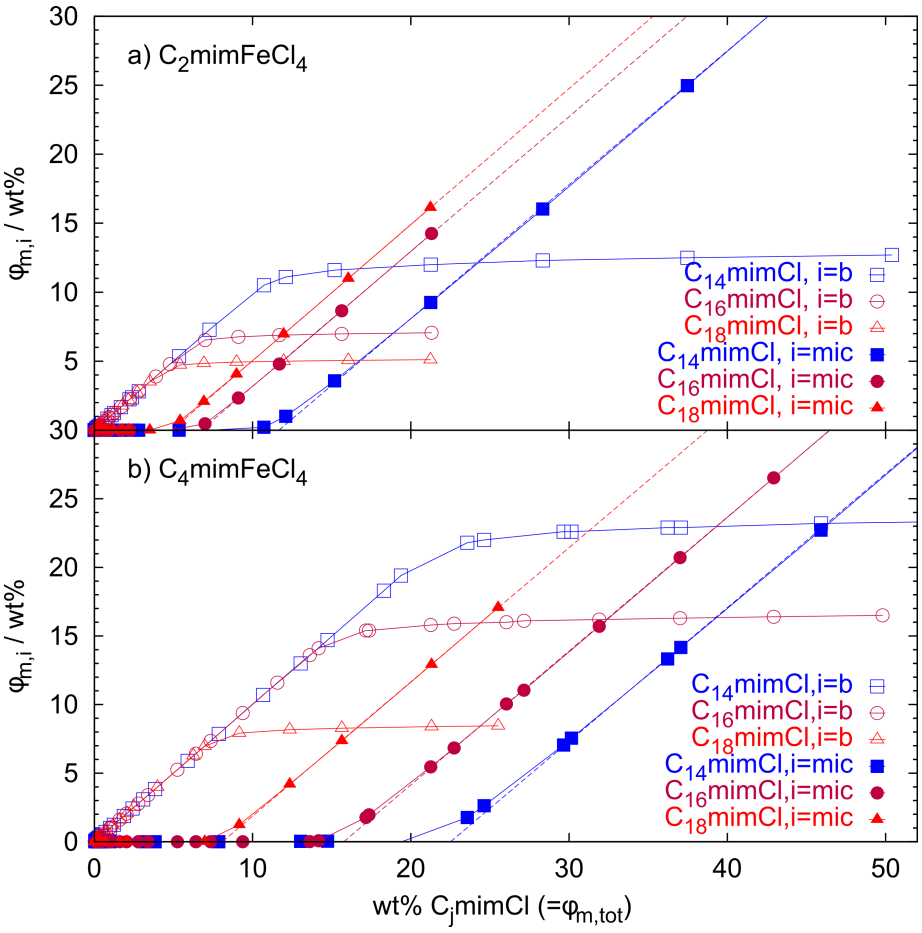

Figure 3.5 Values for monomeric surfactant (open symbols) and surfactant in micelles (filled symboles) derived from the modified Szyszkowski model. The cmc_γ was determined by linear regression (broken line) of data points in the linear regime at higher concentration and extrapolation to $\phi_{m,mic}$=0.

Alternatively in order to quantify the efficiency of different surfactants in the same solvent the surfactant concentration needed to lower the surface tension by 10 mN/m from the value of the pure solvent (c_{10}) can be extracted. All parameters are summarized in table 3.1 and show that the efficiency of

the surfactant is increasing by about a factor 1.5-2 per 2 CH_2-groups, i. e., the hydrophobic effect per CH_2 group is less than half the one in water,[2] which is also reflected in different CH_2 transfer energies for water and MRTIL which are given in table 3.2 and will be discussed later in section 3.2.2.

3.1.3 Small angle scattering

Micellization - SANS:

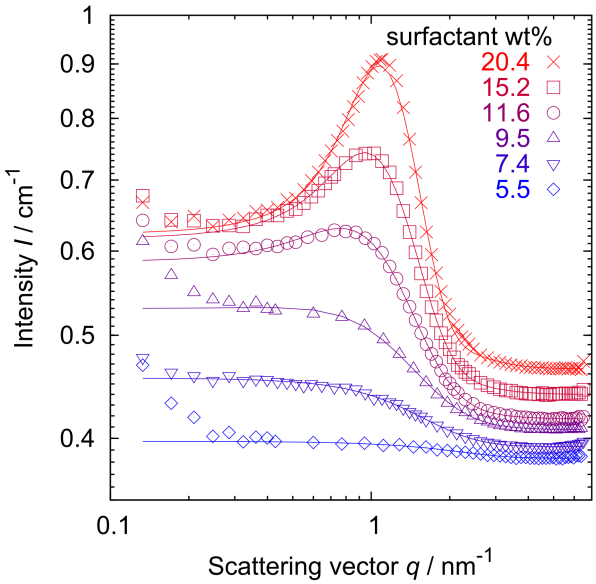

Figure 3.6 Small angle neutron scattering curves for the system C_{18}mimCl in C_2mim$FeCl_4$. Open symbols are data measured at 45°C. Concentration increases gradually from blue to red. Lines are fits according to eq. 3.4a.

Due to the knowledge gained from DSC and surface tension measurements, small angle neutron scattering (SANS) experiments were carried out in the low and mid concentration range to prove the existence of aggregates and characterize them structurally. SANS was necessary as the X-ray high absorbance of iron renders SAXS not a useful technique here. Fig. 3.6 gives the resulting curves exemplary for the system C_{18}mimCl in C_2mim$FeCl_4$ (for the complete set of curves see Fig. A.2 in the appendix). With the enhanced

Table 3.1 Summary of the values extracted from surface tension (cmc_γ and c_{10}), SANS invariant (cmc_{inv}), aggregation number (cmc_{agg}), DSC ($\phi_{m,LC}$ as the lowest concentration at which a LC phase occurs, $T_{m,surf}$ and $T_{Krafft,disc}$, $\Delta T = T_{m,surf} - T_{Krafft,disc}$) and SAXS measurements (d and Δd). For comparison values for comparable aqueous systems found in literature are listed.

$C_i$mim$FeCl_4$	$C_j$mimCl	$\frac{cmc_i(45\,^\circ\mathrm{C})}{\mathrm{wt\%}}$			extracted from Fig. 3.1					$\frac{d}{\mathrm{nm}}$		$\frac{\Delta d}{\mathrm{nm/CH_2}}$	
		$i=\gamma$	$i=inv$	$i=agg$	$\frac{c_{10}}{\mathrm{wt\%}}$	$\frac{\phi_{m,LC}}{\mathrm{wt\%}}$	$\frac{T_{Krafft,disc}}{^\circ\mathrm{C}}$	$\frac{T_{m,surf}}{^\circ\mathrm{C}}$	$\frac{\Delta T}{^\circ\mathrm{C}}$	75 °C	100 °C	75 °C	100 °C
2	14	11.66	9.00	19	6.36	68	19	53	34	3.478	3.406	↑	↑
2	16	6.75	6.50	13	3.51	65	36	64	28	3.746	3.657	0.141	0.131
2	18	4.90	4.00	8	1.91	61	43	70	27	4.043	3.932	↓	↓
4	14	22.51	13.00	25	21.96	76	16	53	37	3.355	3.288	↑	↑
4	16	15.76	9.60	18	15.44	69	29	64	35	3.597	3.521	0.129	0.122
4	18	8.09	6.20	12	9.60	66	36	70	34	3.870	3.775	↓	↓
H_2O	10	1.03[86]	1.05[86a]	—	—	—	—	—	—	—	—	—	—
H_2O	12	0.38,[86]0.35[66]	0.39[86a]	—	—	—	—	—	—	—	—	—	—
H_2O	14	0.09,[86] 0.11[66]	0.12[86a]	—	—	—	—	—	—	—	—	—	—
H_2O	16	0.03[86,87]	0,03[66,86a]	—	—	—	—	—	—	—	—	—	—

[a] measured by conductivity method at 25°C

scattering intensity in the observed q-range the existence of some kind of aggregate structure or at least aggregate-like density fluctuations is already proven.

Qualitatively all data sets have a similar appearance. With higher surfactant concentrations the scattering intensity grows due to more scattering aggregates in the sample. This as well enhances the interactions between aggregates which leads to a correlation peak. The increasing scattering intensity at low q-values could be due to attractive interactions but potentially also to errors in background subtraction. As a first approach to get quantitative information on the ratio of monomerically and micellar dissolved surfactant with a model independent approximation the experimental scattering invariant Q_{inv}^{ex} was compared with expectations calculated from the sample composition. Another advantage of this method is its nearly independence from very low q values which might bare some artifact problems as mentioned above. Errors are mainly produced by the Porod extrapolation and were estimated to be less than 10 % by choosing the data range for the extrapolation carefully. The experimental invariant is defined as

$$Q_{inv}^{ex} = \int_0^{+\infty} I(q) \cdot q^2 \mathrm{d}q \tag{3.2}$$

were the discrete data points were extrapolated to zero and $+\infty$ with standard methods by Guinier and Porod approximations, respectively. A theoretical two-level invariant Q_{inv}^{th} was calculated by considering having a bulk phase composed by the solvent with a quantity cmc_{inv} of monomeric dissolved surfactant plus all the surfactant head groups (-mimCl) and a second

phase composed by the remaining surfactant hydrophobic tails as

$$Q_{inv}^{th} = 2\pi^2 \phi_{bulk} \cdot \phi_{mic} \cdot \Delta SLD^2 \tag{3.3a}$$

$$\phi_{bulk} = (\frac{m_{IL}}{\rho_{IL}} + \frac{m_{surf,b}}{\rho_{surf}} + \frac{m_{surf} - m_{surf,b}}{a \cdot \rho_{mimCl}})/V_{tot} \tag{3.3b}$$

$$\phi_{mic} = 1 - \phi_{bulk} \tag{3.3c}$$

$$cmc_{inv} = \frac{m_{surf,b}}{m_{surf,b} + m_{IL}} \tag{3.3d}$$

with m_i as the masses of MRTIL ($i = IL$), total surfactant ($i = surf$) and surfactant in the bulk ($i = surf, b$), and ρ_i as the corresponding densities. V_{tot} is the resulting total volume of the sample and $1/a$ the mass ratio of mimCl in $C_j$mimCl. The volume ratios ϕ_{bulk} and ϕ_{mic} and the scattering length density difference (contrast) ΔSLD were calculated assuming ideal mixing. (For details see appendix A). As shown in Fig. 3.7 (top) it gives a quite good agreement with the experimental data with the mass ratio of surfactant dissolved in the bulk (cmc_{inv}) being the only free parameter. Only at very high concentration the experimental invariant has appreciable lower values. This could be explained with a general failure of the simple assumption of a fixed *cmc* but an increasing monomeric surfactant concentration which would lower the scattering contrast and with that Q_{inv}^{th}. Such a scenario is also indicated by the fact that the surface tension still decreases beyond the *cmc* (Fig. 3.4).

To get more detailed information on the aggregation behavior, model fitting was applied to the data with a spherical form factor $P(R)$. As most of the samples had high concentrations, a structure factor was necessary to simulate the correlation peak mentioned above. For this reason a hard sphere structure factor $S(R_{HS}, \phi_{HS})$[88] was introduced and implemented in the local

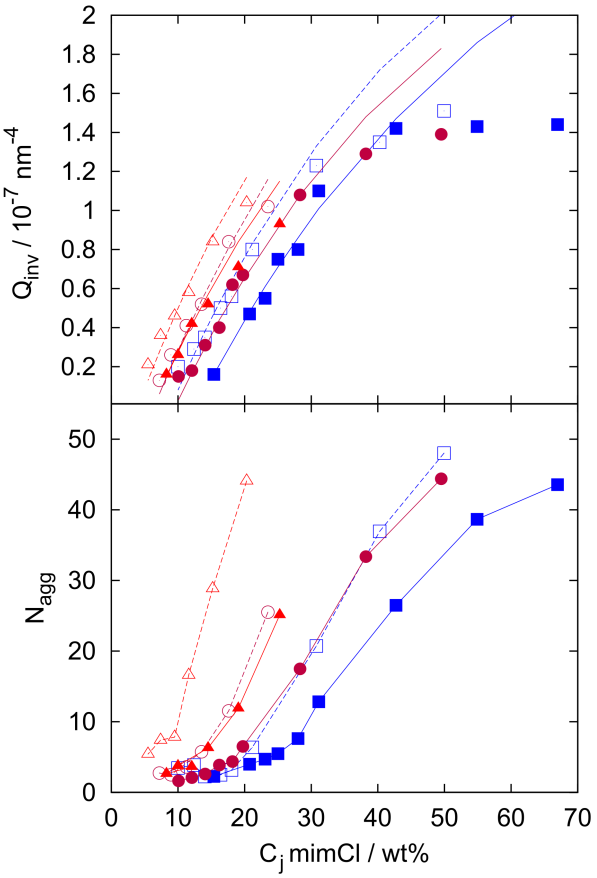

Figure 3.7 Top: Experimental (symbols) and theoretical (lines) invariants for all systems. **Bottom:** Aggregation numbers derived from spherical model fit. In both diagrams binary mixtures of C_{14}mimCl (cubes), C_{16}mimCl (circles) and C_{18}mimCl (triangles) in C_2mimFeCl$_4$ (open symbols, broken lines) or C_4mimFeCl$_4$ (filled symbols, solid lines) as solvent are shown. Data can be found in table A.3.

monodisperse approach (eq. 3.4a).

$$I(q) = BG + \int LN(R_0, \sigma) \cdot P(R) \cdot S(R_{HS}, \phi_{HS})\, \mathrm{d}R \tag{3.4a}$$

$$R_{HS} = R + \Delta R \tag{3.4b}$$

$$\phi_{HS} = \phi_{micelle} \frac{(R + \Delta R)^3}{R^3} \tag{3.4c}$$

By calculating the micelle volume fraction $\phi_{micelle}$ and scattering contrast from the sample composition the final set of fit parameters was reduced to the width (σ) and location (R_0) of the size distribution ($LN(R_0, \sigma)$), the "effective" interaction radius of the hard spheres ΔR, the volume ratio of MRTIL in micelles (α), the ratio of surfactant in bulk phase (y) and the background BG. It might be noted that here we imply that also some of the solvent (MRTIL) can be contained within the micellar core, which is quite a different situation compared to water based micelles. However, due to the much weaker amphiphilicity of the surfactants here, this might be a realistic scenario. A detailed description of the model fitting is given in the appendix A. From these the aggregation number (N_{agg}) can be extracted by comparing the aggregates mean volume with the surfactant hydrocarbon chain volume v_{HC}:

$$N_{agg} = \frac{4}{3}\pi \left\langle R^3 \right\rangle \frac{1}{v_{HC}} (1 - \alpha) \tag{3.5}$$

Here $\langle R^3 \rangle$ is the 3rd moment of the size distribution. Results are shown in Fig. 3.7 (bottom). From the plot one can extract an aggregation concentration (cmc_{agg}), where after an initial nearly constant single-digit aggregation number at low concentration the aggregation number rises. Apparently the aggregation here proceeds via a broad range of pre-aggregation and therefore in not such a sharp fashion as typically observed in aqueous systems. Several other SANS models have been examined and led to a qualitatively similar result for the aggregation number (see appendix A.1, table A.3). In general, the aggregation numbers increase with increasing length of the alkyl chain of

the surfactant and are higher in C_2mimFeCl$_4$ compared to C_4mimFeCl$_4$ as solvent.

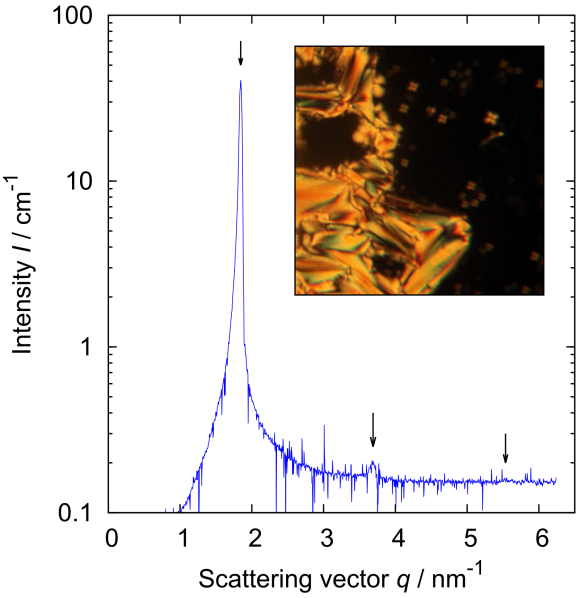

Figure 3.8 SAXS curve of 85 wt% C_{14}mimCl in C_2mimFeCl$_4$. Arrows indicate the peak positions at $q = n \cdot 1.84\,\mathrm{nm}^{-1}$, characteristic for lamellar structures. The inset shows a representative polarized microscopy image of the same system at 75°C.

The lamellar Phase - SAXS:

The liquid crystal region found in all six systems shown in Fig. 3.1 were furthermore characterized by polarized microscopy and small angle X-ray scattering (SAXS). Due to low X-ray transmission of the iron containing solvents, samples with solvent ratios above ≈25 wt% cannot be measured with the used setup. Therefore samples at surfactant concentrations of 85 wt% were investigated and are marked in Fig. 3.1 with crosses. Fig. 3.8 gives the SAXS curve for the system C_2mimFeCl$_4$/C_{14}mimCl (for others see appendix A). From the periodicity of the correlation peaks appearing at $q = n \cdot 1.84\,\mathrm{nm}^{-1}$ and the characteristic pattern (maltese crosses) in polarized microscopy the liquid crystals can clearly be identified as lamellar structures. Due to limitations in the temperature range offered by the SAXS machine it was difficult

to heat all measured samples to the isotropic state followed by a slow cooling to the desired liquid crystal state before scattering experiment to ensure a well ordered sample. Due to this limitation only the scattering curve of the here shown C_2mimFeCl$_4$/C_{14}mimCl system with a LC→isotropic transition at relatively low temperatures at 85 wt% C_{14}mimCl shows higher order peaks. Nevertheless all six systems could be identified by the characteristic polarized microscopy textures.

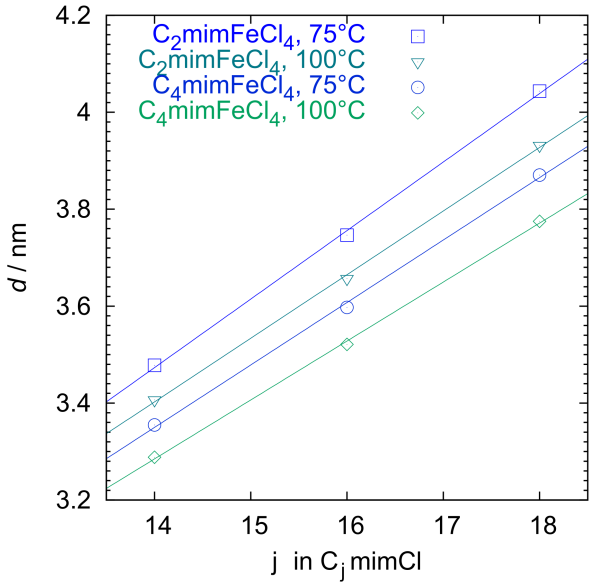

Figure 3.9 Lamellar spacing $d = 2 \cdot \pi / q_{max}$ extracted from the peak position q_{max} from SAXS measurements. Solid lines are giving linear regressions.

From the first correlation peak position, the periodic length $d = 2 \cdot \pi / q_{max}$ can be calculated as given in table 3.1 and is plotted in Fig 3.9 for the different surfactants at 75 and 100 °C. The change in d as a function of surfactant chain length (as derived by linear regression, plotted in Fig. 3.9, listed in table 3.1) gives a value of 0.12-0.14 nm per CH_2 group which is very close to the projection of one C-C-bond on the chain axis suggesting an interpenetration of the surfactant chains in a bilayer. This is in a good agreement with similar structures found in IL systems.[81,89–91] Changing the MRTIL from C_2mimFeCl$_4$ to C_4mimFeCl$_4$ leads to a reduced value for the domain size d

which is true for both temperatures. This can be due to a better solubility of the hydrocarbon chains in the MRTIL with the longer alkyl chain. This then would promote a deeper penetration of the solvent into the surfactant lamella leading to a bigger headgroup area which would force the lamella to become thinner (because the overall amount of surfactant chain stays constant). This interpretation is supported by surface tension and SANS results which both suggest a bigger headgroup area while using C_4- instead of C_2mim$FeCl_4$ as solvent (see table A.5 and Fig. A.1, respectively). Increasing the temperature as well reduces the size of d which can be interpreted analogously.

3.2 Discussion

3.2.1 Low and mid surfactant concentrations - critical aggregation conditions

The *cmc* values derived from the three different methods are rather scattered which indicates that the micellar transition is not so well-defined but instead occurs over a rather broad concentration range. This phenomenon is also known for water systems, especially for the case of rather low aggregation numbers.[92,93] In our system these deviations are rather broad as the relatively weak amphiphilicity leads to a correspondingly broad transition region of aggregate formation. The here obtained surface tension curves show similar critical aggregation concentrations compared to much shorter (C_6 or C_8) surfactants in water. In contrast at very high concentrations these systems show a surface tension plateau and not a smooth decrease after the *cmc* as observed in the here presented MRTIL systems.[93–95] For all systems the cmc_{inv} derived from the SANS invariant has always values lower than cmc_{agg} (from the surface tension) insofar as the scattering invariant is independent of the aggregate size or shape and detects therefore already the very small pre-aggregates formed by just a few molecules. Depending on the amphiphilic strength of the system (which follows the order C_{18}mimCl>C_{16}mimCl>C_{14}mimCl and C_2mim$FeCl_4$>C_4mim$FeCl_4$) cmc_γ lies closer to cmc_{inv} or cmc_{agg}. With information from these complementary methods we can draw a picture of a

broad transition range with a concentration dependent aggregation, having small pre-aggregates at lower concentration and continuously growing aggregates with growing surfactant concentration. Additionally the SANS model fitting suggest that the micelles are partly (∼30-40 vol%) swollen by the solvent. The ratio of solvent in the micelle continuously declines with surfactant concentration approaching zero at a concentration around the phase separation boundary at high concentration (see Fig. A.1). This observation can be related to the continuously increasing average aggregation number (Fig. 3.7) and only for the high aggregation numbers achieved towards the phase boundary really rather compact micellar aggregates can be formed that do not contain some of the solvent.

Table 3.2 Free enthalpies of micellization (ΔG_{mic}) and transfer energies for a CH_2-unit into the solvent (ΔG_{CH_2}), calculated from *cmc* and c_{10} values. Here *cmc* and c_{10} values are used in units of mole fractions. The last column shows the mean value of all four previous columns. For comparison values for comparable aqueous systems found in literature are listed.

$C_n$mim$FeCl_4$	$C_j$mimCl	$\frac{\Delta G_{mic}=RT\ln cmc_i}{RT}$				mean value
		$i=\gamma$	$i=inv$	$i=agg$	$\ln c_{10}$	$\frac{\Delta G_{CH_2}}{RT}$
2	14	-2.17	-2.43	-1.68	-2.77	↑
2	16	-2.79	-2.83	-2.13	-3.45	0.27
2	18	-3.19	-3.40	-2.70	-4.14	↓
4	14	-1.44	-1.98	-1.34	-1.46	↑
4	16	-1.86	-2.36	-1.73	-1.88	0.24
4	18	-2.60	-2.87	-2.21	-2.43	↓
H_2O	10	-12.56[86a]			—	↑
H_2O	12	-12.77[87a], -14.73[86a]			—	1.25[86a]
H_2O	14	-15.24[87a], -17.31[86a]			—	1.22[87a]
H_2O	16	-17.64[87a], -20.04[86a]			—	↓

[a] calculated from data measured with conductivity method at 25°C considering a partial degree of dissociation of micelle counter ions.

3.2.2 Quantitative results on solvent quality for self-assembly

An observation which can be made by all used techniques is an amphiphilic character much lower compared to similar water systems (compare table 3.1 and 3.2): Much higher concentrations are needed to form aggregates, and a relatively small lamellar phase is found, which is the only representative of LC-phases in these systems. For water the LC region is broader and includes more diversity e. g. an additional hexagonal phase.[96] In general the class of surfactants under investigation has a suppressed amphiphilic behavior in the IL solvents investigated here compared to water. To find the reason it is useful to consider separately the solvophilic and -phobic character. Qualitative information on the solvophilicity gives the ΔT value which is the difference between surfactant melting point and Krafft discontinuity. As in both transitions the surfactant melts the value gives the compensation of thermal energy by solvent attraction and can therefore directly be related to the solvophilicity (deviations originating from the appearance of solvated solids in the phase diagram are not considered here). Values for ΔT extracted from Fig. 3.1 are listed in Table 3.1. As expected the value is enhanced by shorter surfactant chains and larger alkyl substituents in the solvent molecule. The absolute values of around 30–40°C are comparable with similar water systems[97] and for that certify a good solvophilicity.

On the other hand quantitative values on the solvophobicity can be extracted from the *cmc* values. The free enthalpy of micellization (ΔG_{mic}) is proportional to $\ln cmc$ and furthermore the variation of ΔG_{mic} by the surfactant's chain length gives the transfer energy for a CH_2 unit into the solvent (ΔG_{CH_2}) and therewith a quantity for its solvophobicity. Table 3.2 gives the calculated values for both solvents. As expected C_2mimFeCl_4 gives a slightly higher value as its alkyl chain is shorter and therefore differs more strongly from the surfactants than is the case for C_4mimFeCl_4. Compared to water, where values of $1.2 - 1.4\,RT$ are usual,[66,86,98] this is much smaller and gives a quantitative value to explain the lower driving force to self-assembly. Polypropylene oxide (PO) is an example for a hydrophobic unit having a

transfer energy of 0.15 RT per PO unit into water[92] which is even less than the here found value for the IL-systems. This fits perfectly to the observation that PO units are normally used as long-chain polymer units and that the aggregate core is swollen with water[99,100] in the same manner as here the SANS model indicates micelles swollen with MRTIL.

For that reason it seems to be useful in future work to concentrate on the solvophobic part of the molecule to enhance its amphiphilic character. By introducing disturbances into the alkane chain like branching, or substituents like ester groups or unsaturated functions the crystalline ordering of the hydrocarbon chain will be suppressed and the Krafft discontinuity (as well as the melting point of pure surfactant) is expected to be shifted to lower temperatures. With that hidden mesoscopic phases (as observed in the C_{14}mimCl/C_4mim$FeCl_4$-system) could be discovered as thermodynamically stable states. As aggregates in the isotropic phase region and the LC as well contain fluid chains they are expected to be not effected by these actions.

3.3 Conclusion

In this chapter a systematic study on imidazolium-based surfactant in paramagnetic ionic liquids of the type $C_i$mim$FeCl_4$ was done. By using a variety of methods its phase and aggregation behavior was investigated. SANS experiments clearly demonstrate the formation of aggregates at higher surfactant concentrations but with rather low aggregation numbers. These micelles are partly swollen by solvent and this process occurs over a rather broad concentration range. They become larger and contain then less MRTIL solvent with increasing concentration. The tendency for micellization is higher the longer the alkyl chain of the surfactant and the shorter the alkyl chain of the solvent. At high concentration the only LC phase found is a lamellar phase. The ability of long chain $C_j$mimCl to self-assemble was proven and evaluated compared to common water systems, where the solvophobic effect of the alkyl chain in the MRTIL was determined to be only about a fifth of that in water.

From our analysis we were able to distinguish between the effects of the

solvophobic and -philic part of the surfactant. As a result it was quantitatively shown that deficits in the ability to self-assemble are mainly present in the surfactant's lipophobic tail which gives a good fingerpost on how to enhance the tendency for self-assembly for these kind of systems in future work.

4

Other Binary Mixtures

Compared to binary mixtures, microemulsions are self-assembled system with a higher complexity, indicated by its higher number of components. To discuss the driving force of self-assembly in these kind of systems it is helpful to know the location of all species in a mixture within the microstructure. As a preliminary work one can consider isolated binary mixtures as they give information about interactions between two species in an environment easier to analyze compared to multi-component systems. In chapter 3 it was already focused on the surfactant in binary mixtures and a result was a reasonable amount of monomerically dissolved surfactant molecules within the MRTIL-solvent dependent on surfactant and MRTIL chain length.

In chapter 5 four-component microemulsion systems including an alcohol as cosurfactant will be discussed and as a preliminary work for this, this chapter focuses on the interaction of the co-surfactant with both continuous phases present in the microemulsions: the MRTIL and the oil.

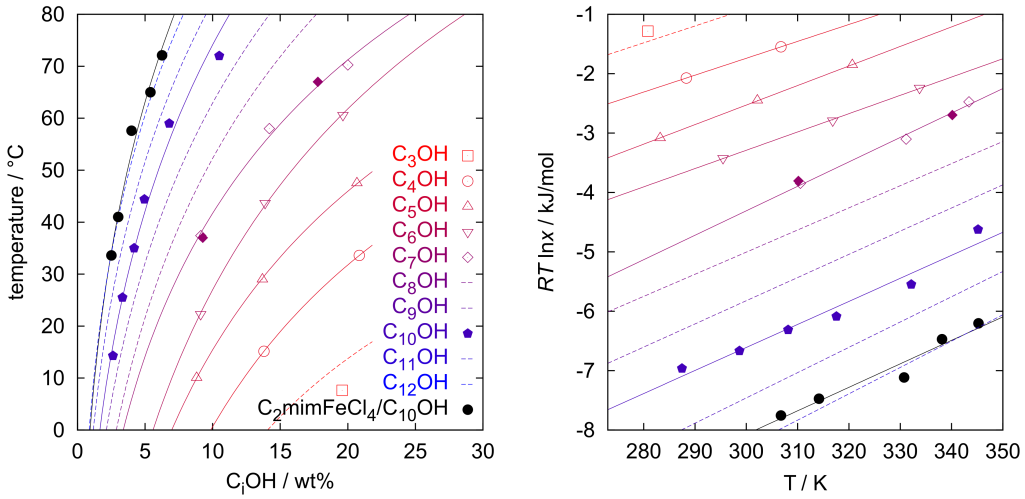

Figure 4.1 Solubility curves for binary mixtures C_4mimFeCl$_4$/C$_i$OH (colored symbols) and C_2mimFeCl$_4$/C_{10}OH (black symbols). Open symbols are data obtained by visual observation, filled symbols are data obtained by DSC measurements, solid lines are fits via $RT \ln x = -\Delta G_{mix} = T\Delta S - \Delta H$, broken lines are theoretical values obtained by extrapolating the measured results.

4.1 Binary Mixtures MRTIL/alkanol

Fig. 4.1 shows the solubility curves for different n-alkanols in C_4mimFeCl$_4$. To extract quantitative values for the interaction between alcohol and ionic liquid, the free enthalpy of mixing (ΔG_{mix}) was calculated using the mole fraction of alcohol (x). As already discussed in section 3.2.2, the dependency of the free enthalpy with respect to the alcohol chain length gives directly the transfer energy for one CH_2-unit into the MRTIL given by eq. 4.1.

$$\Delta G_{mix} = \Delta G_{\mathrm{CH_2}} \cdot i + \Delta G_{eg} \tag{4.1}$$

Here i is the number of CH_2-groups and ΔG_{eg} is the part of the free enthalpy of mixing which is originated by the endgroups OH and CH_3 in the alcohol molecule. A calculated value for 45 °C is listed in table 4.1 and is comparable to the value measured for binary MRTIL/surfactant mixtures (see. table 3.2). As expected the process of mixing is entropy driven as indicated by positive ΔS values and a cost in energy (positive ΔH values). In Fig.

4.1 additionally the solubility curve for decanol in C_2mimFeCl_4 is shown. As expected the solubility is lower compared to C_4mimFeCl_4. An extrapolation of the data for the shorter chain alcohols in C_4mimFeCl_4 to the theoretical curves for C_{11}OH and C_{12}OH shows that the solubility in C_2mimFeCl_4 is shifted by two CH_2-units compared to C_4mimFeCl_4, an observation which was as well also found for different quantities (e. g. *cmc*, ϕ_{LC}) in the binary MRTIL/surfactant mixtures (see chapter 3).

As *n*-alcohols are regarded to function as cosurfactant in microemulsion formulation it is important to see that there is only little solubility of decanol in the ionic liquid (around 1.7 wt% and 2.8 wt% for C_2mimFeCl_4 and C_4mimFeCl_4 at 20 °C, respectively). Furthermore it is possible that decanol is not dissolved monomerically but organizes in aggregates which would make it even more likely to find the decanol in the interface when one is offered, as it is the case in a microemulsion. For these reasons the solubility of decanol in the MRTIL was subsequently neglected.

Table 4.1 Free enthalpies of mixing (ΔG_{mix}) and transfer energies for a CH_2-unit into the solvent (ΔG_{CH_2}), calculated from the fit parameters ΔS and ΔH.

$C_x$mimFeCl_4 / C_iOH		fit parameter			mean value
		$\frac{\Delta S}{\mathrm{J(Kmol)^{-1}}}$	$\frac{\Delta H}{\mathrm{kJ(mol)^{-1}}}$	$\frac{\Delta G_{mix}(45\,^\circ\mathrm{C})}{\mathrm{RT}}$	$\frac{\Delta G_{CH_2}(45\,^\circ\mathrm{C})}{\mathrm{RT}}$
4	4	28.4	10.3	0.46	↑
4	5	32.9	12.4	0.73	
4	6	30.8	12.5	1.03	0.29
4	7	41.1	16.7	1.35	
4	10	38.8	18.2	2.23	↓
2	10	39.5	19.9	2.78	

4.2 Binary mixtures cyclohexane/decanol

With the oil (cyclohexane) decanol is miscible over a broad range of composition and therefore it has to be considered that maybe the decanol is monomerically dissolved in the oil instead of a location in the interface which would change a lot in the interpretation of microemulsion phase behaviour. A starting point is the investigation of binary mixtures of decanol with cyclohexane.

Fig. 4.2 gives SANS spectra of different decanol concentrations in D12-cyclohexane. As the incoherent scattering scales with the H/D-ratio in the sample which leads to very different background levels for each concentration, the background was subtracted to make the samples better comparable. For this purpose the background (BG) for each curve was calculated by the sum of the curve for pure D12-cyclohexane and 30 wt% decanol/H12-cyclohexane, weighted by the decanol volume fraction as given by eq. 4.2.

$$BG = (1 - \phi_{decanol}) \cdot I(q)_{D12-cyclo} + \phi_{decanol} \cdot I(q)_{H12-cyclo/decanol} \tag{4.2}$$

To get a first estimate for the size of the scattering objects, a Guinier plot was done giving the radius of gyration R_G and the zero angle intensity $I(0)$:

$$I(q) = I(0) \exp -\frac{R_G^2 q^2}{3} \tag{4.3a}$$

$$I(0) = V \cdot \phi \cdot \Delta SLD^2 \tag{4.3b}$$

The obtained results are listed in table 4.2. First of all it can be seen that R_G is similar for all four decanol concentrations. The sample at 20 wt% deviates from the Guinier-law at low q and this behaviour is even more pronounced for the sample at 30 wt%. This can be explained by interactions between the scattering objects for which case the Guinier law is not defined.

The results from the Guinier fits can be compared with theoretical val-

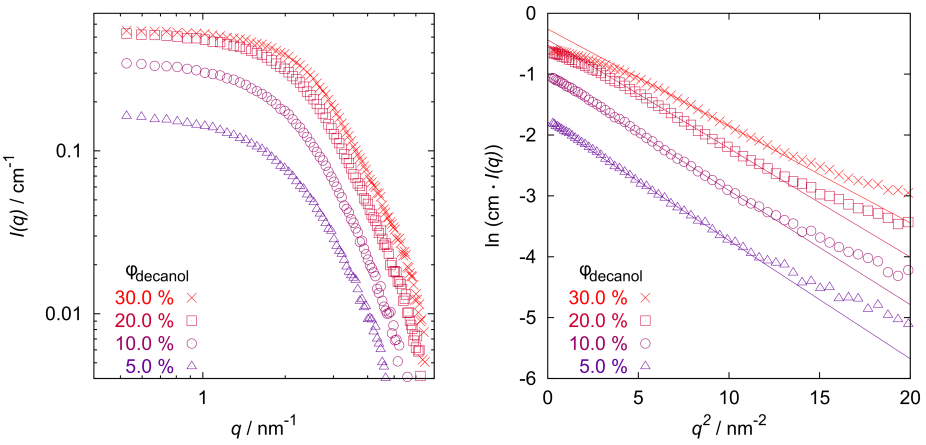

Figure 4.2 left: SANS curves for binary mixtures of decanol and D12-cyclohexane with a subtracted background as calculated by eq. 4.2, **right:** Guinier-plot, fit was done in the range $7\,\mathrm{nm}^{-2} \leq q^2 \leq 10\,\mathrm{nm}^{-2}$.

ues which are expected to be found for decanol molecules. For the case of completely collapsed spheres the radius of gyration can be expressed by eq. 4.4a.

$$R_g = \sqrt{\frac{3R^2}{5}} \tag{4.4a}$$

$$R = \sqrt[3]{\frac{3V}{4\pi}} \tag{4.4b}$$

$$V = N_{agg} \cdot 0.317\,\mathrm{nm}^3 \tag{4.4c}$$

Here $0.317\,\mathrm{nm}^3$ is the volume of one single decanol molecule and N_{agg} the number of decanol molecules per sphere. The resulting volume V of one sphere can additionally be used to calculate $I(0)$ via eq. 4.3b. The calculated values are listed in table 4.2. Comparing the values obtained by Guinier fits with the calculated ones it can be seen that $I(0)$ suggests aggregates of ≈ 2 and R_G of ≈ 12 decanol molecules. Although this lack in self-consistency expose the used simple model as insufficient, it is already demonstrated that scattering can not be explained solely by single decanol monomers.

Table 4.2 Results for Guinier fits shown in Fig. 4.2 and theoretical values for different decanol aggregation numbers, expressed by the sphere model.

	Guinier fit		Sphere model $N_{agg} = 1$		$N_{agg} = 2$		$N_{agg} = 12$	
$\phi_{decanol}$	$\frac{I(0)}{\mathrm{cm}^{-1}}$	$\frac{R_G}{\mathrm{nm}}$	$\frac{I(0)}{\mathrm{cm}^{-1}}$	$\frac{R_G}{\mathrm{nm}}$	$\frac{I(0)}{\mathrm{cm}^{-1}}$	$\frac{R_G}{\mathrm{nm}}$	$\frac{I(0)}{\mathrm{cm}^{-1}}$	$\frac{R_G}{\mathrm{nm}}$
0.30	0.772	0.691	0.466	0.328	0.932	0.413	5.592	0.750
0.20	0.647	0.731	0.311	0.328	0.621	0.413	3.728	0.750
0.10	0.355	0.750	0.155	0.328	0.311	0.413	1.864	0.750
0.05	0.167	0.764	0.078	0.328	0.155	0.413	0.932	0.750

To get a more detailed look on the distribution of molecules in the mixture (and as a prework to get access to the background of contrast variated microemulsion studies, see section 5.2.2) for each decanol concentration shown in Fig. 4.2 the scattering contrast was varied by using several different ratios of deuterated and hydrogenated cyclohexane as oil. The resulting spectra can be found in Fig. 4.3. Additionally shown in this figure are scattering curves of different D/H-ratios of oil without decanol. In contrast to studies based on H/D-water where the solvent background is flat, it can be clearly seen that this is not the case for the much bigger cyclohexane molecules who give a reasonable scattering form factor by itself, visible at high q. This leads to a superposition of the scattering of single cyclohexane molecules in cyclohexane and decanol aggregates in cyclohexane.

The scattering profiles of the binary mixtures of D12/H12-cyclohexane as shown in Fig. 4.3 can be fitted with a simple sphere form factor were the radius is given by a lognormal size distribution. For a description of the model see appendix A.1.1. The results are listed in table 4.3. The obtained average radius is in a good agreement with the expected theoretical hard sphere radius of a single cyclohexane molecule of around 0.27 nm. The size distribution did not improve the fit results reasonably for which reason the width was set to $\sigma = 10^{-6}$ which makes the size distribution quasi monodisperse.

To substract the scattering of cyclohexane molecules from the contrast

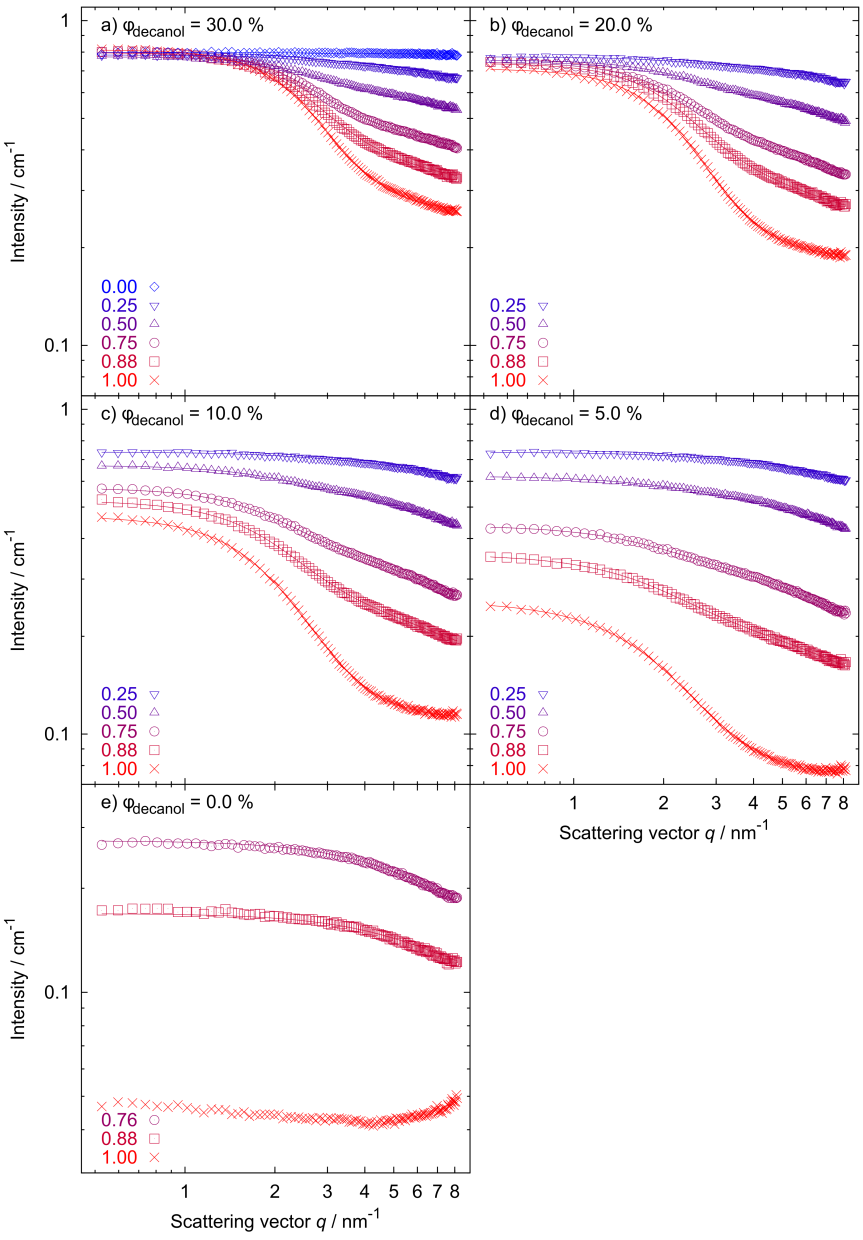

Figure 4.3 a-d: SANS curves for different decanol concentrations in cyclohexane (symbols) and fits with eq. 4.5 (lines). **e:** Different D12/H12-cyclohexane mixtures without decanol (symbols) and fits with a spherical form factor (lines, see table. 4.3). In all graphes the key indicates the volume fraction of deuterated cyclohexane in the oil phase.

Table 4.3 Fit results for cyclohexane mixtures using a spherical form factor. Volume fractions and SLD were calculated from sample composition, σ and R_0 was simultaneously fitted for both samples, $\sqrt[3]{< R^3 >}$ was then calculated as the average radius.

$\phi_{\text{D12-cyclo}}$	σ	R_0/nm	$\Delta SLD/10^{-4}\,\text{nm}^{-2}$	$BG/\,\text{cm}^{-1}$	$\sqrt[3]{< R^3 >}$/nm
0.88	10^{-6}	0.305	7.00	0.109	0.305
0.76		0.292		0.155	0.292

variation data shown in Fig. 4.3 a-d, the same spherical model was used. Accordingly the SANS curves were fitted as expressed by eq. 4.5 with a summation of a constant incoherent background (BG), a spherical form factor to express the cyclohexane monomers and a summand to express the decanol aggregates ($TS(q)_{dec}$). The cross-terms between these two were assumed to be negligible.

$$I(q) = TS(q)_{dec} + \int LN(R_0, \sigma) \cdot P(q)_{sphere} \mathrm{d}R + BG \tag{4.5}$$

As summand to describe the scattering originated from the decanol, the Teubner-Strey model (see eq. 5.2a) was used. This model was used because it expresses the data by two length scales (the quasiperiodic repeat distance D_s and the correlation length ξ) and one parameter related to the scattering invariante ($\langle\eta^2\rangle$), but without making any restriction to the structural shape. For each decanol concentration ξ and D were hold constant and fitted simultaneously as the structure of decanol in cyclohexane should not be effected by the grade of oil deuteration. The fit results are listed in table 4.4. The parameters which were obtained for the sphere summand are in good agreement with the values obtained for pure oil samples (see table 4.3) which supports that by the used fit method the Teubner-Strey summand now represents solely the scattering contribution of decanol in oil. Here it can be seen that the domain size D is far too high compared to the dimensions for single decanol moelcules which is in a good agreement with the results from the Guinier analysis and speaks for a decanol aggregation. ξ shows relative

Table 4.4 Fit parameters due to eq. 4.5 for decanol/cyclohexane mixtures with different scattering contrasts. ξ and D were fitted simultaneously for each decanol concentration, σ was fixed at 10^{-6} to prevent overfitting, f_p and ΔSLD were calculated from the sample composition ($f_p = \phi_{\mathrm{D12}}$ or ϕ_{H12}).

composition				TS summand				sphere summand				
ϕ_{dec}	ϕ_{D12}	ϕ_{H12}	$x_{\mathrm{D12\text{-}cyclo}}$	$\frac{\xi}{\mathrm{nm}}$	$\frac{D}{\mathrm{nm}}$	$\frac{\langle\eta^2\rangle}{\mathrm{cm^{-1}\,nm^{-3}}}$	$\frac{BG}{\mathrm{cm^{-1}}}$	f_p	σ	$\frac{R_0}{\mathrm{nm}}$	$\frac{\Delta SLD}{10^{-4}\mathrm{nm^{-2}}}$
0.30	0.70	0.00	1.00	0.5269	3.4816	0.5481	0.2582	0.0000	—	—	—
0.30	0.61	0.09	0.87	”	”	0.4104	0.3173	0.0800	10^{-6}	0.3400	7.00
0.30	0.53	0.17	0.75	”	”	0.3232	0.3823	0.1700	”	0.2971	”
0.30	0.35	0.35	0.50	”	”	0.1471	0.4800	0.3500	”	0.2724	”
0.30	0.18	0.52	0.25	”	”	0.0310	0.6408	0.1800	”	0.3120	”
0.30	0.00	0.70	0.00	”	”	0.0089	0.7899	0.0000	—	—	—
0.20	0.80	0.00	1.00	0.5694	3.9335	0.3795	0.1860	0.0000	—	—	—
0.20	0.69	0.11	0.87	”	”	0.2925	0.2535	0.1000	10^{-6}	0.3408	7.00
0.20	0.60	0.20	0.75	”	”	0.2247	0.3043	0.2000	”	0.3165	”
0.20	0.40	0.40	0.50	”	”	0.0996	0.4281	0.4000	”	0.2852	”
0.20	0.20	0.60	0.25	”	”	0.0211	0.6178	0.2000	”	0.3139	”
0.10	0.90	0.00	1.00	0.5652	4.5316	0.2067	0.1115	0.0000	—	—	—
0.10	0.78	0.12	0.87	”	”	0.1555	0.1761	0.1100	10^{-6}	0.3259	7.00
0.10	0.68	0.22	0.75	”	”	0.1192	0.2314	0.2200	”	0.3106	”
0.10	0.45	0.45	0.50	”	”	0.0547	0.3699	0.4500	”	0.2821	”
0.10	0.23	0.67	0.25	”	”	0.0094	0.5807	0.2300	”	0.3107	”
0.05	0.95	0.00	1.00	0.4892	5.2409	0.1123	0.0747	0.0000	—	—	—
0.05	0.82	0.13	0.87	”	”	0.0870	0.1449	0.1100	10^{-6}	0.3165	7.00
0.05	0.71	0.24	0.75	”	”	0.0676	0.1963	0.2400	”	0.2999	”
0.05	0.47	0.47	0.50	”	”	0.0357	0.3567	0.4700	”	0.2784	”
0.05	0.24	0.71	0.25	”	”	0.0068	0.5692	0.2400	”	0.3176	”

low values for all decanol concentrations due to a very loosely structured system without any long-range ordering.

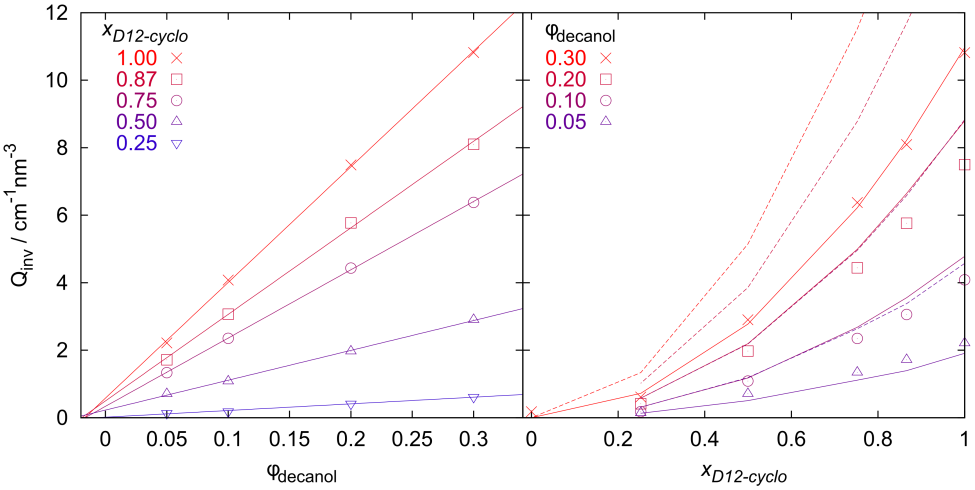

Figure 4.4 Scattering invariant $Q_{inv} = 2\pi^2 \langle \eta^2 \rangle$ calculated from the Teubner-Strey fit parameter listed in table 4.4 for different scattering contrasts and decanol concentrations (symbols). Solid lines are giving linear fits (left graph) or calculated values for a two-level model with a volume ratio of 0.30 cyclohexane in decanol and 0.02 decanol in cyclohexane domain (right graph). For comparison the values for domains of pure cyclohexane and decanol without a mutual miscibility are given in the right graph as broken lines.

Furthermore from the amplitude parameter ($\langle \eta^2 \rangle$) the scattering invariant can be calculated due to eq. 5.2d which is plotted in Fig. 4.4 for all D/H-cyclohexane ratios. Compared to the MRTIL/surfactant binary systems, where a kink in the concentration dependent development of Q_{inv} indicates a critical aggregation concentration (compare Fig. 3.7), here the trend is strictly linear going approximately through the origin. When calculating (as well analog to eq. 5.2d) a simple theoretical two-level invariant with sharply separated decanol and oil domains, this gives much too high values. Instead when considering an appropriate constant solubility of oil in the decanol domain and decanol in the oil, a very good agreement with the experimental results is obtained as shown in Fig. 4.4 (right). This model only gives comparable values when just a little amount of decanol is dissolved in the oil

domain but a bigger amount of oil in the decanol which is quite intuitive as the decanol has long enough alkyl chains to host the oil while the OH-groups would find a strictly hydrophobic environment in the cyclohexane domain which is less favorable. In total this gives a picture of a solution were the two components are not simply statistically mixed but where loosely associated domains are present. In view of decanol as a cosurfactant in microemulsion formulation this speaks, on the mesoscopic scale, for a driving force of decanol molecules into an amphiphilic interface although macroscopic observations show a broad miscibility of decanol and cyclohexane.

5

Microemulsions

The conditions for forming microemulsions based on non-aqueous solvents are not really well understood and accordingly this point will be investigated in detail in this chapter by using several different alcohols as cosurfactant, an imidazolium chloride based surfactant with different alkyl chain lengths and a systematic variation in composition with respect to the oil and cosurfactant employed. In a second part the system is restricted to one representative oil and cosurfactant (cyclohexane and 1-decanol, respectively) but instead the MRTIL alkyl chain length will be varied giving information on the influence of the solvent polarity on microemulsion formation. In total this extends the concept of structural control by variation of the chain length of the surfactant and the solvent and gives a more complete view on the system providing thereby the possibility to draw more general conclusions on self-assembly in non-aqueous media. Hereby the main focus lies on elucidating the role of the surfactant chain length in stabilizing microemulsions with MRTILs.

5.1 Microemulsions based on C_4mimFeCl$_4$

5.1.1 Micellization with decanol

In a first step we investigated the binary or pseudo-binary (containing cosurfactant in addition) systems in order to elucidate their potential as a basis for microemulsion formation. As shown earlier by recording temperature dependent binary phase diagrams (see chapter 3), the Krafft points of the pure surfactants in C_4mimFeCl$_4$ are, dependent on the chain length, above or around 24 °C and with that no microemulsion formation is expected at ambient conditions. Fig. 5.1 shows surface tension measurements at 45 °C as a function of surfactant+decanol concentration of solutions of $C_j$mimCl/decanol in C_4mimFeCl$_4$. While in the decanol free binary systems (Fig. 5.1 top) the reduction of the surface tension depends on the surfactant chain length (as already discussed in chapter 3), by adding decanol this effect is first damped (1 mol decanol per 1 mole surfactant, Fig. 5.1 middle) and vanishes completely by adding more cosurfactant (Fig. 5.1 bottom) what could be explained by the rather high amount of decanol used, i. e., the decanol is effectively determining the amphiphilic strength in these mixtures.

In the following microemulsion systems at ambient conditions (24 °C) will be discussed, which works out despite the Krafft point issue, as all formulations studied contain rather large amounts of cosurfactant which reduce the Krafft temperature correspondingly. Although these surface tension measurements shown here were recorded at higher temperatures (to avoid problems with the Krafft point) we may conclude from that data to the aggregation behavior at room temperature as it does not change much in this temperature range. This was concluded from surface tension measurements at room temperature (Fig. B.12, with systems including enough decanol to lower the Krafft point below room temperature) and having obtained comparable SANS spectra at 24 and 36 °C (see Fig. B.11 in the appendix B). The surface tension measurements at ambient conditions also show a significant decrease of the Krafft point by adding alcohol which makes it possible to formulate systems at room temperature.

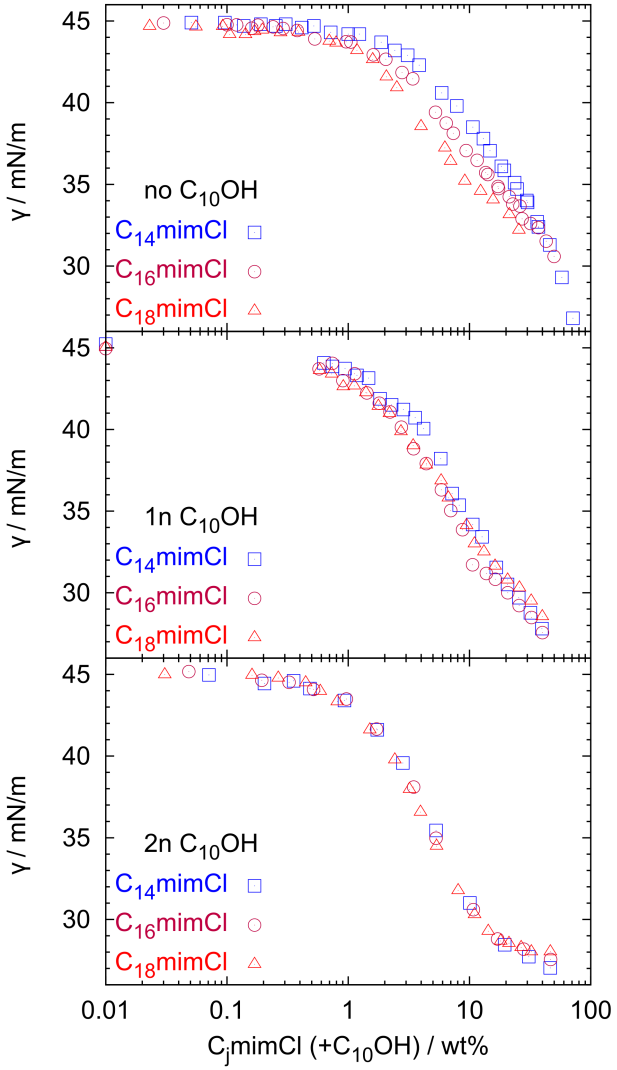

Figure 5.1 Surface tension measurements at 45 °C for binary mixtures of C_4mimFeCl$_4$/$C_j$mimCl (top), C_4mimFeCl$_4$/$C_j$mimCl+1 mol decanol (middle) and C_4mimFeCl$_4$/$C_j$mimCl+2 mol decanol (bottom) by using C_{14}mimCl (cubes), C_{16}mimCl (circles) or C_{18}mimCl (triangles) as surfactant.

5.1.2 Microemulsions

Adding an oil (which is insoluble in the MRTIL) to the system IL/$C_j$mimCl can lead to the formation of microemulsions if the amphiphilic strength of the surfactant $C_j$mimCl is high enough to stabilize the MRTIL/oil interface. As discussed in section 5.1.1 surface tension measurements predict no microemulsion formation with pure surfactant at room temperature as the *cmc* goes beyond the solubility of the surfactant. However, by adding the cosurfactant decanol micelle formation is much facilitated and accordingly they might be swollen by adding an oil, thereby leading to the formation of microemulsions.

Macroscopic observations.

The main characteristics of a microemulsion system can already be noticed by the simple observation of macroscopic phase separation. Fig. 5.2 shows the ability to solubilize C_4mim$FeCl_4$ in cyclohexane at 24 °C dependent on the alcohol/C_{16}mimCl ratio for different aliphatic alcohols as cosurfactant. For our experiments we chose cyclohexane as oil as it demands a reduced need of surfactant to form monophasic systems and shows a higher solubilisation capacity compared to other oils, such as isooctane and several linear alkanes, see Fig. 5.3. As clearly seen by extrapolating to an alcohol free system, the ability of MRTIL uptake is zero which means that no microemulsion formation takes place. Adding alcohol supports an uptake of MRTIL what can be interpreted as the formulation of microemulsions. Independent on which alcohol was used qualitatively the uptake capacity is first enhanced by enhancing the alcohol ratio in the mixture and then passes through a maximum which indicates an optimum cosurfactant/surfactant ratio. This phenomenon could be explained either by entropy/synergism effects due the preferred solubility of surfactant and alcohol mainly in the MRTIL and oil, respectively, as proposed by Huibers et al. for mixed surfactant systems[101] or by geometric considerations, as the surfactant/cosurfactant ratio influences the packing parameter and the maxima in MRTIL-uptake shown in Fig. 5.2 are located at the resulting optimal interfacial curvature for MRTIL uptake.

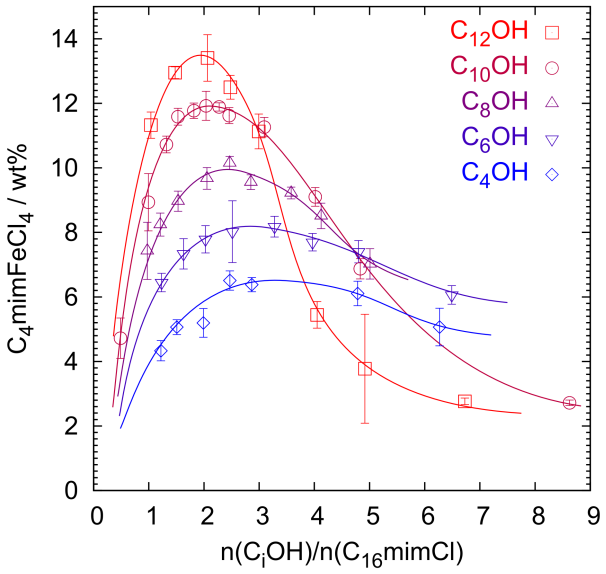

Figure 5.2 Maximum MRTIL uptake at a constant ratio of cyclohexane/(cyclohexane+alcohol+C_{16}mimCl) of 86.4 wt%. for different aliphatic alcohols as cosurfactant as a function of alcohol/C_{16}mimCl mole ratio at 24 °C. Lines are guides to the eye. Details can be found in experimental section 2.2.

The shift of the maximum to higher alcohol content for shorter chain alcohols can on one side be explained by a growing solubility in the MRTIL and with that a growing part of alcohol which is not acting as a cosurfactant but is solubilized monomerically (or at least as aggregates too small for a solvent uptake) in the MRTIL. In addition, for conventional microemulsions it has been observed before that the rigidity of the amphiphilic monolayer becomes substantially reduced by the addition of shorter chain alcohols but not so for longer alcohols like octanol or decanol.[102] As for the stability of the microemulsions a certain rigidity of the amphiphilic film is required which is better achieved for the longer chain alcohols. Both effects (maximum shift and lower efficiency) are consistent with both proposed explanations for the maximum: A growing solubility of alcohol in the MRTIL will as well reduce the entropy/synergism effect mentioned before (leading as well to a lower

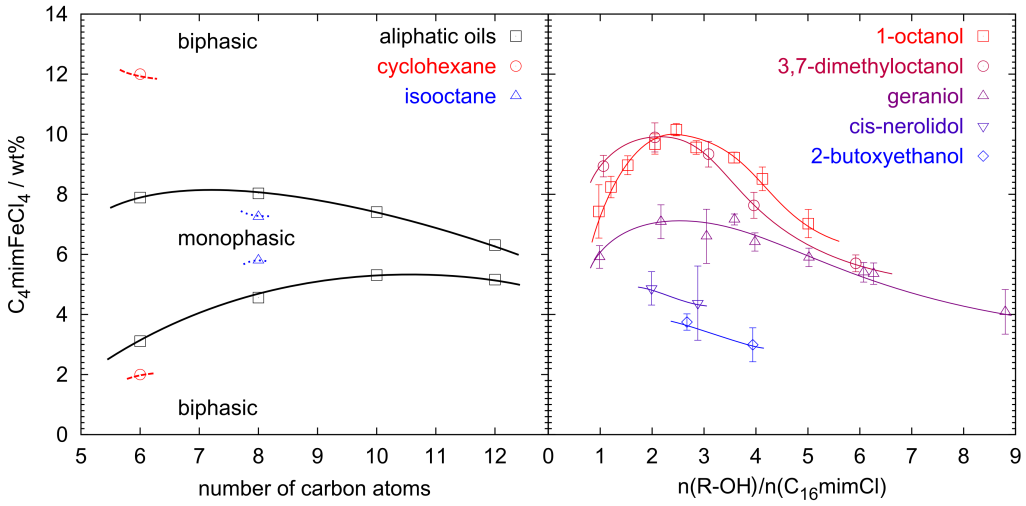

Figure 5.3 left: Effect of different oils on the ability to form monophasic systems by using decanol as cosurfactant. **right:** Effect of different alcohols on the ability to form monophasic systems by using cyclohexane as oil. Both graphs were recorded as described in the experimental section for pseudo binary phase diagrams. Starting with homogeneous samples formulated with alcohol, C_{16}mimCl and a starting amount of 86.4 wt% oil, C_4mimFeCl$_4$ was added dropwise. In the left graph all samples have a constant mol ratio of decanol/C_{16}mimCl=2 (13.6 wt%).

amplitude) and lowers the effective content in the interface (maximum shift to higher concentrations). Similarly the packing parameter will be shifted less by a shorter alcohol and therefore a larger amount would be needed to achieve a balanced microemulsion (where one expects the peak of solubility). In addition, with increasing alcohol chain length the amphiphilic system is rendered more hydrophobic and having a stiffer monolayer, which apparently favors oil solubilisation.[102] At higher alcohol/surfactant ratios the uptake ability declines due to a lack of amphiphilicity as decanol itself is not a feasible amphiphile in this system.

In addition to the linear aliphatic alcohols several other alcohols (3,7-dimethyloctanol, geraniol, *cis*-nerolidol, 2-butoxyethanol) were tested but gave no improvements in MRTIL solubilization (see Fig. 5.3), only the 3,7-dimethyloctanol had a similar performance as the 1-octanol. Due to its good ability to function as cosurfactant, decanol was used for further investiga-

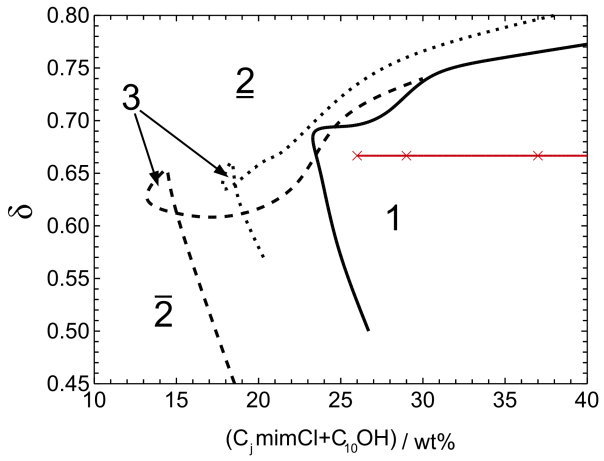

Figure 5.4 Phase digrams observed by plotting surfactant/cosurfactant ratio δ (eq. 5.1) vs. wt% surfactant+cosurfactant at equal cyclohexane and MRTIL volumes (Kahlweit fish) for C_{14}mimCl (straight line), C_{16}mimCl (dotted line) and C_{18}mimCl (broken line) at 24 °C. The red line gives the experimental path for SANS experiments done at the C_{14}mimCl system shown in Fig. 5.6.

tions. Although dodecanol enhances even more the MRTIL uptake it was not taken into account as its melting point is above/around room temperature and caused solubility problems which lead to solid precipitate at low MRTIL concentrations (not shown in Fig. 5.2). Employing alkanes of different chain length as oils was also investigated and showed that the extent of the monophasic microemulsion region becomes smaller with increasing chain length (Fig. 5.3).

Fig. 5.4 shows Kahlweit-fish diagrams for C_4mim$FeCl_4$/cyclohexane systems for all three surfactant chain lengths. As a control parameter to modulate the packing parameter not the temperature was used (as known for nonionic surfactants in water) but the cosurfactant/surfactant molar ratio δ (as similarly done when investigating the effect of medium chain alcohols as cosurfactants on the phase behavior of nonionic surfactants.[103]

$$\delta = \frac{n(\mathrm{C_{10}OH})}{n(\mathrm{C_{10}OH}) + n(\mathrm{C_j mimCl})} \tag{5.1}$$

As already shown in Fig. 5.2 for C_{16}mimCl, one finds for all three surfac-

tant systems that the presence of alcohol to form microemulsions is crucial. The efficiency decreases from C_{18}- over C_{16}- to C_{14}mimCl due to a rising monomeric surfactant solubility in the MRTIL. Nevertheless the formation of microemulsions instead of pure molecular solutions is definitely proven by observing a three phase region. Characteristic parameters for the position of the fishtail (minimum amount of amphiphilic material and surfactant/-cosurfactant ratio δ required for forming a single phase microemulsion) are summarized in table 5.1. For the C_{14}mimCl system no three phase system was observed but SANS measurements (Fig. 5.6, along the path shown in Fig. 5.4) proof the existence of mesoscopic structuring. Apparently the C_{14}mimCl is a much weaker structuring amphiphile and the 3-phase region was either too small to be detected (hindered also by the rather high concentrations and corresponding slowness of the phase separation) or is simply no longer appearing.

Table 5.1 Characteristic parameters extracted from Fig. 5.4 giving the fishtail position (lowest surfactant amount needed to form the monophasic region) and the required cosurfactant content δ (eq. 5.1).

$C_j$mimCl	14	16	18
C_{10}OH+$C_j$mimCl [wt%]	23	19	15
δ	0.68	0.64	0.61

Beside the phase behavior induced by surfactant/cosurfactant variation, in addition compositions with different oil/MRTIL ratios were investigated. Fig. 5.5 shows the pseudo ternary phase diagram of these systems with a constant $C_j$mimCl/decanol mole ratio of 1:2 (equals to $\delta = 0.67$), this value being chosen as here maximum solubilization occurs according to Fig. 5.2. With a solid precipitate at low MRTIL-content, a multi-phase region in the low surfactant region and a broad mono-phasic region above a certain surfactant concentration all three surfactants show similarities. An increasing need of MRTIL to dissolve all surfactant in the oil rich region with longer surfactant chain is due to a decreasing solubility in C_4mim$FeCl_4$. The re-

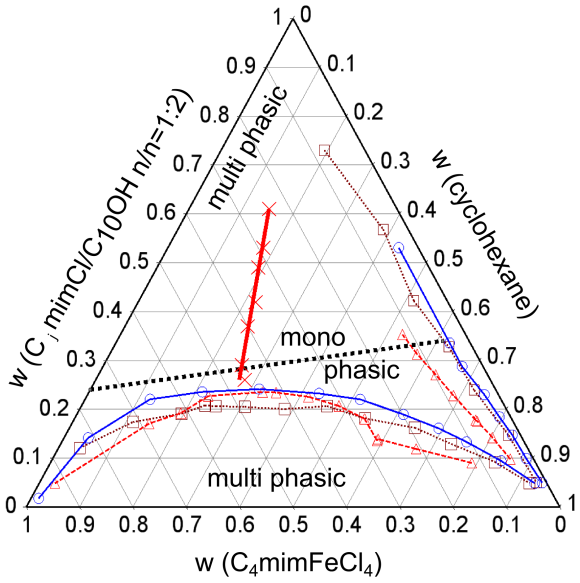

Figure 5.5 Ternary phase diagrams for C_{14}mimCl (straight line, circles), C_{16}mimCl (dotted line, squares) and C_{18}mimCl (broken line, triangles) at $(24.0 \pm 0.1)\,^{\circ}$C by weight. Thick red line/crosses gives the sample position/experimental path for SANS experiments done with the C_{14}mimCl system shown in Fig. 5.6, thick dotted line for SANS experiments done at all three surfactant system shown in Fig. 5.8

gion at high surfactant and MRTIL concentrations was not investigated in detail but gives qualitatively a multi-phase region increasing in size with longer surfactant chain. The only small differences in the size of the multi phase region at low surfactant concentrations could be misinterpreted as only a weak enhancement of the ability to form microemulsions with longer alkyl chains. However a comparison with Fig. 5.4 can explain this phenomenon with the fact that a $C_j$mimCl/decanol mole ratio of 1:2 ($\delta = 0.67$) is rather ideal for the C_{14}mimCl but becomes increasingly less so for the longer chain surfactants which illustrates the essential need of both MRTIL/oil- and surfactant/cosurfactant-ratio variation to get a full picture of the surfactant efficiency.

Mesoscopic structure.

Low viscosities of samples located in the single-phasic region of the phase diagram (see appendix B.9) already hints at the presence of a microemulsion in this range and against formation of a liquid crystalline phase, which is further confirmed by the fact of optical isotropy. Additionally by conductivity measurements a percolation point can be observed (see appendix B.8), which is typical of microemulsion systems.[51] To investigate the system on the mesoscopic scale SANS measurements were done, one of the key methods to study microemulsions.[104] The scattering curves in Fig. 5.6 show that the intensity increases largely upon reducing the content of amphiphile in the system and for the highest amphiphile content only very little coherent scattering is seen. Also interesting to note is that only at intermediate amphiphile concentration a correlation peak is seen that vanishes again upon further dilution. In order to deduce quantitative structural information from the SANS curves we applied the phenomenological Teubner-Strey (TS) model,[105] in which the scattering intensity is given by eq. 5.2a and is basically determined by the quasiperiodic repeat distance D_s (eq. 5.2b) and the correlation length ξ (eq. 5.2c) of the structural units. Here $\langle\eta^2\rangle$ is directly related to the scattering invariant (Q_{inv}) and accounts for the contrast $\Delta\rho$ and volume fractions Φ of the oil and MRTIL phase (eq. 5.2d).

$$I(q) = \frac{8 \cdot \pi \cdot c_2 \cdot \langle\eta^2\rangle / \xi}{a_2 + c_1 \cdot q^2 + c_2 \cdot q^4} + BG \tag{5.2a}$$

$$\frac{D_s}{2\pi} = \left[\frac{1}{2}\sqrt{\frac{a_2}{c_2}} - \frac{1}{4}\frac{c_1}{c_2}\right]^{-1/2} \tag{5.2b}$$

$$\xi = \left[\frac{1}{2}\sqrt{\frac{a_2}{c_2}} + \frac{1}{4}\frac{c_1}{c_2}\right]^{-1/2} \tag{5.2c}$$

$$\langle\eta^2\rangle = \Phi_{IL} \cdot \Phi_{oil} \cdot (\Delta\rho)^2 = Q_{inv}/2\pi^2 \tag{5.2d}$$

Next to the background, D_s, ξ and $\langle\eta^2\rangle$ were free parameters during fitting even though the latter value derives directly from the sample composition and the distribution of the components in the two phases. As the distribution of

surfactant and decanol between polar, oily and interface domains is not clear this approach is justified. More details on this are given in the last part of this chapter. From the fit parameters the amphiphilicity factor f_a and the renormalized mean bending modulus κ were calculated according to eqs. 5.3 and 5.4, respectively.[106,107]

$$f_a = c_1/\sqrt{4a_2c_2} \tag{5.3}$$

$$\frac{\kappa}{k_BT} = \frac{10\sqrt{3}\pi}{64}\frac{\xi}{D_s} \tag{5.4}$$

The amphiphilicity factor quantifies the amphiphilic strength of the system whereby a value of -1 corresponds typically to a highly structured lamellar phases while higher values are due to a decreasing amphiphilicity. Well structured ("good") microemulsions are normally found to have negative values near -1 the Lifshitz line is defined at $f_a = 0$ and the disorder line at $f_a = +1$. Above this the triclinic point can be found.[108]

Table 5.2 Teubner-Strey fit parameter derived from SANS measurements shown in Fig. 5.6 and calculated amphiphilicity factor f_a and bending rigidity κ.

C_{14}mimCl $+C_{10}$OH [wt%]	ξ [nm]	D_s [nm]	$\langle\eta^2\rangle$ $[\frac{1}{\text{cm nm}^3}]$	BG $[\frac{1}{\text{cm}}]$	f_a	κ [kT]
61	1.31	3.66	0.02	0.69	-0.67	0.31
53	1.34	3.86	0.04	0.66	-0.65	0.30
49	1.43	4.04	0.06	0.65	-0.67	0.30
42	1.50	4.63	0.11	0.64	-0.61	0.28
37	1.50	5.38	0.16	0.64	-0.51	0.24
29	1.55	8.64	0.26	0.61	-0.12	0.15
26	1.51	16.26	0.30	0.59	0.49	0.08

Fig. 5.6 shows SANS measurements at constant oil/MRTIL volume ratio of 1:1 along the experimental path shown in Fig. 5.4 and 5.5. Decreasing the amphiphile amount while keeping the oil/MRTIL ratio constant at 1:1

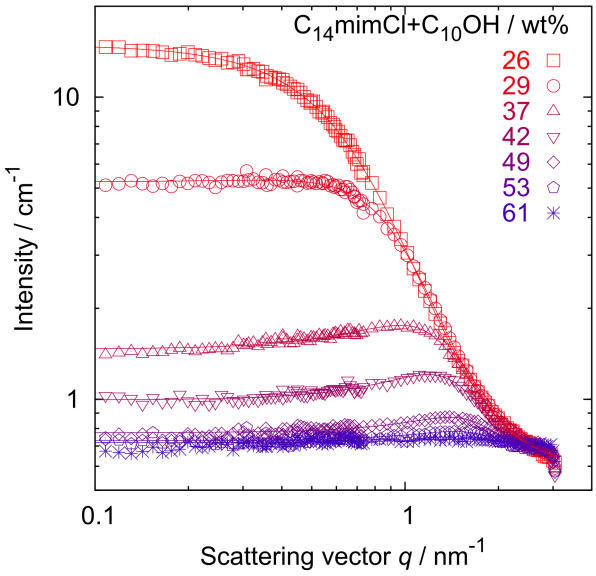

Figure 5.6 SANS data (symbols) for microemulsions formulated with C_{14}mimCl and a constant volume ratio oil/MRTIL=1:1. For sample positions see Fig. 5.4. Straight lines are results from fits with eq. 5.2a.

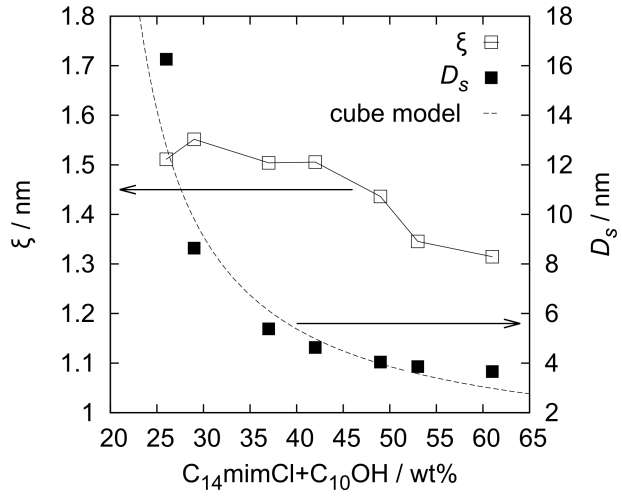

Figure 5.7 Teubner-Strey fit parameters ξ (open squares) and D_s (filled squares) for C_{14}mimCl derived from curves displayed in Fig. 5.6. Dashed line displays the cube model (eq. 5.6) with $\Sigma = 1.0\,\mathrm{nm}^2$, $c_{mon} = 0.17$ and $x_c = 0.5$. For details see the appendix B.10.

leads to an increase in scattering intensity due to an increase of the size of the structures present. The data were fitted with the TS model (eq. 5.2a) and the obtained parameters are summarized in Fig. 5.7 and Table 5.2. The domain size D_s increases with decreasing surfactant concentration which can be explained such that less amphiphile per fluid is available to form an oil/MRTIL interface and with that the oil and MRTIL domains have to grow to house the volume of the two solvents with less surfactant stabilized interface available. D_s increases largely upon reaching the emulsification failure (cf. Fig. 5.4 and 5.5) and appears to be diverging there. A simple geometrical model to estimate the domain size D_s was proposed by Jouffroy et al.[109] describing the microemulsion by a lattice of cubes filled with either polar (water) or apolar (oil) solvent and a separating surfactant layer between differently filled cubes leading to eq. 5.5

$$D_s = \frac{6\omega\phi_p\phi_{ap}}{\Sigma\phi_s} \tag{5.5}$$

with ϕ_s, ϕ_p, ϕ_{ap} as the volume fractions of surfactant in the interface, polar and apolar phase, respectively, the molecular volume of one surfactant molecule (ω) and the surfactant headgroup area (Σ). As several assumptions done here (i. e. vanishing interfacial surfactant layer thickness compared to the cube length, location of all surfactant molecules in the interface, very small surfactant concentration) are not valid for our actual system, eq. 5.5 was modified in such a way that the surfactant was partly allowed to be monomerically dissolved in the MRTIL phase and the surfactant interface was divided between the apolar and polar phase, whereby the volume fraction of the surfactant head (ϕ_{mimCl}) and decanol head (ϕ_{OH}) was added to the polar phase and the location of the alkyl chains (ϕ_{C14} and ϕ_{C10}) was defined by the ratio x_c which is added to the polar phase. This model can be expressed by the following set of equations:

$$
\begin{aligned}
D_s &= \frac{6\omega_{C14}\phi_p\phi_{ap}}{\Sigma\phi_{C14,i}} && (5.6)\\
\phi_{C14,i} &= \phi_{C14} - \phi_{IL}c_{mon} && (5.7)\\
\phi_p &= \phi_{IL} + \phi_{mimCl} + \phi_{OH} + (\phi_{C10} + \phi_{C14,i})x_c + \phi_{IL}c_{mon} && (5.8)\\
\phi_{ap} &= \phi_{oil} + (\phi_{C10} + \phi_{C14,i}) \cdot (1 - x_c) && (5.9)\\
c_{mon}[\mathrm{wt\%}] &= 100 \cdot \left[1 + \frac{\rho_{IL}}{\rho_{C14}} \frac{M_{C14}}{M_{C14} + M_{mimCl}} \frac{1}{c_{mon}}\right]^{-1} && (5.10)
\end{aligned}
$$

Here $\omega_{C14} = 0.4051\,\mathrm{nm}^3$ is the volume of one C_{14}-chain, ϕ_{IL} and ϕ_{oil} are the volume fractions of MRTIL and oil, respectively. c_{mon} gives the amount of surfactant chains not present in the interface but dissolved monomerically in the MRTIL. With eq. 5.10 it can be expressed in a form which makes it comparable to the definitions of the *cmc* which were made earlier (see Fig. 3.5 and eq. 3.3d). Here ρ and M are the density and molar mass, respectively. Σ gives the average area occupied by one surfactant+decanol unit. The model with suitable parameters is plotted in Fig. 5.7. (For curves with different parameters see Fig. B.15 in the appendix B.10. Despite its simplicity it suffices to describe the experimental values quite well with values for Σ around $1\,\mathrm{nm}^2$ which is a reasonable value for the size of the surfactant head group. For comparison the same surfactant was found to have a minimum headgroup area of $0.7\,\mathrm{nm}^2$ at the water/air and EAN/air interface.[66] Similarly the monomeric concentration of 14 wt% surfactant in the MRTIL which is needed to describe the data corresponds well to the *cmc* measurements described before (cf. table 3.1). This findings accord with the preliminary made interpretations and yields a coherent model. ξ increases as well by lowering the amphiphile amount explained by more defined aggregates with a lower polydispersity. Calculated values for the amphiphilicity factor and the mean bending modulus as listed in table 5.2 are as well in a good agreement with the here proposed trends. κ increases with increasing surfactant concentration as the structures are expected to become stiffer, f_a is located well under the Lifshitz-line[108] as expected for microemulsion structures at higher surfactant concentrations. Only near the phase boundary at low surfactant

concentration a positive value points to a less structured system.

To compare structures formed with the different surfactants additional SANS measurements were done along the experimental path shown in Fig. 5.5 (thick dotted line). For all samples the ratio between the molar quantity of amphiphile and the solvent volume was held at a constant value of $n(\mathrm{C_j mimCl})/(V_{MRTIL}+V_{oil}) = 0.68\,\mathrm{mol/L}$. Then the only parameter varying is the ratio between oil and MRTIL volume defined as

$$x_{MRTIL} = \frac{V_{MRTIL}}{V_{MRTIL} + V_{oil}} \tag{5.11}$$

In Fig. 5.8 the obtained SANS curves are shown and it is interesting to note that the overall scattering intensity becomes lower with increasing length of the surfactant. So apparently the structural units are the largest for the shortest chain surfactant. In contrast, the correlation peak at intermediate mixing ratio of MRTIL/oil becomes more prominent with increasing surfactant chain length, which indicates that the degree of ordering increases correspondingly.

Teubner-Strey fits as described above were carried out and the results are summarized in table 5.3. In all three surfactant systems the amplitude (quantitatively expressed by $\langle\eta^2\rangle$) is decreasing with increasing x_{MRTIL} due to a vanishing contrast by substituting deuterated cyclohexane with hydrogenated MRTIL. Following the picture of an inversion of mean curvature while going from the oil-rich to the MRTIL-rich side of the phase diagram a maximum in domain sizes D_s is expected for intermediate x_{MRTIL} and can indeed be observed for all three surfactants as seen in Fig. 5.9.

Surprisingly the correlation length ξ is not following simultaneously the same trend as known from water systems.[105,110] Instead after a similar rise up to $x_{MRTIL} \approx 0.3$, ξ decreases again for higher MRTIL content. This can be interpreted by a more flexible and interpenetrating mesoscopic structure in the MRTIL-dominated region which is supported by an increasing value for f_a. A second observation not being in accordance with common water systems is the fact that the structures are getting bigger by shortening the alkyl chains. Intuitively one would expect stiffer and bigger domains with

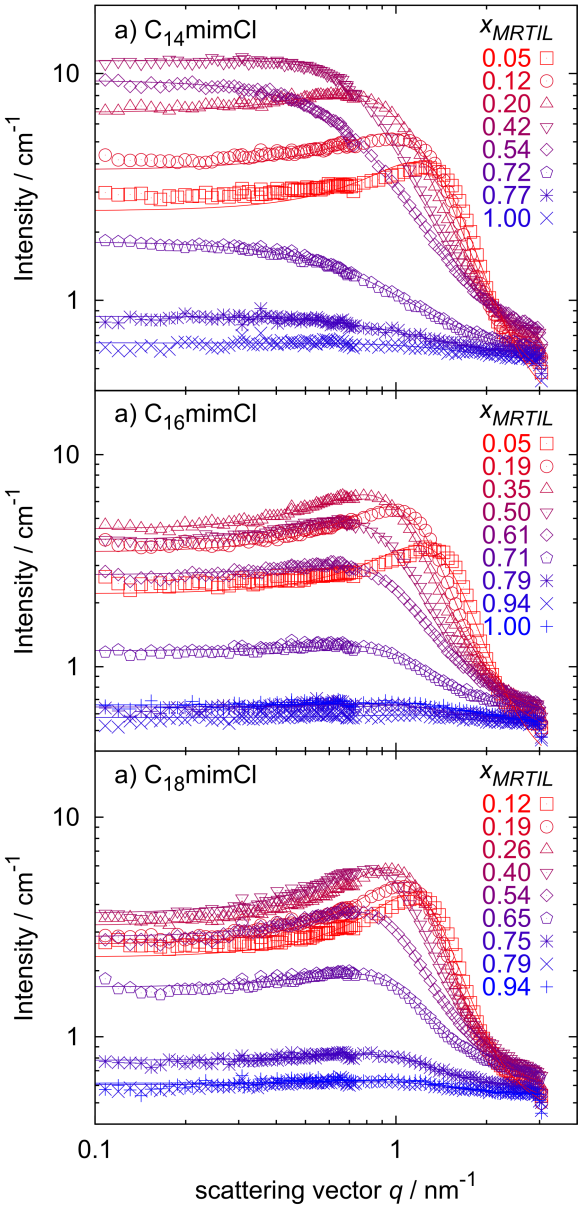

Figure 5.8 Selected SANS data (symbols) for microemulsions formulated with C_{14}mimCl (a), C_{16}mimCl (b) and C_{18}mimCl (c) along the experimental path displayed in Fig. 5.5. Straight lines are fits with eq. 5.2a. Further spectra can be found in Fig. B.7, appendix B.

Table 5.3 Teubner-Strey fit parameters (see eq. 5.2a) derived from SANS measurements shown in Fig. 5.8 and calculated amphiphilicity factor f_a and bending rigidity κ calculated with eq. 5.3 and 5.4, respectively.

	x_{MRTIL}	ξ [nm]	D_s [nm]	$\langle\eta^2\rangle$ $[\frac{1}{\text{cm nm}^3}]$	BG $[\frac{1}{\text{cm}}]$	f_a	κ [kT]
C_{14}mimCl	0.05	1.67	4.86	0.60	0.29	-0.65	0.29
	0.12	1.74	5.67	0.57	0.38	-0.58	0.26
	0.19	1.79	6.15	0.54	0.48	-0.54	0.25
	0.20	1.82	7.19	0.51	0.54	-0.43	0.21
	0.37	1.77	8.82	0.44	0.59	-0.23	0.17
	0.42	1.69	9.88	0.41	0.63	-0.07	0.15
	0.49	1.54	10.77	0.33	0.65	0.11	0.12
	0.54	1.36	12.48	0.30	0.70	0.36	0.09
	0.60	1.27	13.85	0.22	0.66	0.50	0.08
	0.72	0.90	16.04	0.08	0.60	0.78	0.05
	0.77	0.87	8.95	0.03	0.58	0.45	0.08
	1.00	0.78	5.41	0.03	0.54	0.10	0.12
C_{16}mimCl	0.05	1.69	4.76	0.56	0.29	-0.67	0.30
	0.12	1.91	5.38	0.51	0.41	-0.66	0.30
	0.19	2.05	5.91	0.46	0.47	-0.65	0.29
	0.27	2.20	6.42	0.43	0.57	-0.65	0.29
	0.35	2.15	6.90	0.36	0.58	-0.59	0.27
	0.42	2.11	7.24	0.30	0.62	-0.54	0.25
	0.50	1.95	7.54	0.24	0.63	-0.45	0.22
	0.55	1.87	7.57	0.21	0.68	-0.41	0.21
	0.61	1.71	7.45	0.15	0.66	-0.35	0.19
	0.71	1.53	6.84	0.05	0.63	-0.32	0.19
	0.79	1.56	5.96	0.01	0.57	-0.46	0.22
	0.94	1.41	4.85	0.01	0.54	-0.54	0.25
	1.00	1.07	4.80	0.03	0.55	-0.33	0.19
C_{18}mimCl	0.12	2.09	5.21	0.44	0.44	-0.73	0.34
	0.19	2.27	5.70	0.38	0.48	-0.72	0.34
	0.26	2.37	6.11	0.38	0.57	-0.71	0.33
	0.33	2.35	6.51	0.32	0.59	-0.67	0.31
	0.40	2.36	6.81	0.29	0.68	-0.65	0.29
	0.47	2.19	7.12	0.24	0.68	-0.58	0.26
	0.54	2.03	7.07	0.19	0.68	-0.53	0.24
	0.59	1.92	7.18	0.14	0.68	-0.48	0.23
	0.65	1.77	6.89	0.09	0.67	-0.44	0.22
	0.75	1.58	6.14	0.03	0.59	-0.45	0.22
	0.79	1.57	5.75	0.01	0.55	-0.49	0.23
	0.94	1.52	5.52	0.01	0.55	-0.50	0.23

longer chains. While a higher stiffness is indeed confirmed by higher values for ξ and κ, the contrary behavior of the domain size can be explained by a better molecular solubility of C_{14}mimCl compared to the longer chain surfactants in C_4mimFeCl$_4$ leading to a smaller interface to volume ratio and a tendency for building bigger structures.

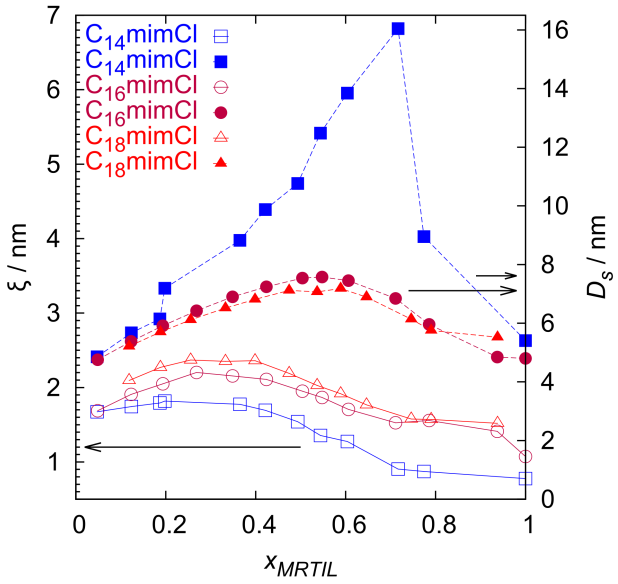

Figure 5.9 Teubner-Strey fit parameters ξ (correlation length, open symbols) and D_s (quasiperiodic repeat distance, filled symbols) for C_{14}mimCl (squares), C_{16}mimCl (circles) and C_{18}mimCl (triangles) as a function of x_{MRTIL} derived from curves displayed in Fig. 5.8.

Again some limitations of comparability may arise from the fact that the samples have different positions relatively to the fishtail position (compare Fig. 5.4), a complication not to be avoided as within a 4-component system such compromises regarding the composition have to be done, in order to have better comparability for other aspects. While the C_{16}- and C_{18}mimCl containing systems are placed in a region relatively far from the fishtail, the C_{14}mimCl containing system is located very close to its optimal δ-value to produce bigger structures.

To get an even more detailed insight into the microemulsion structure,

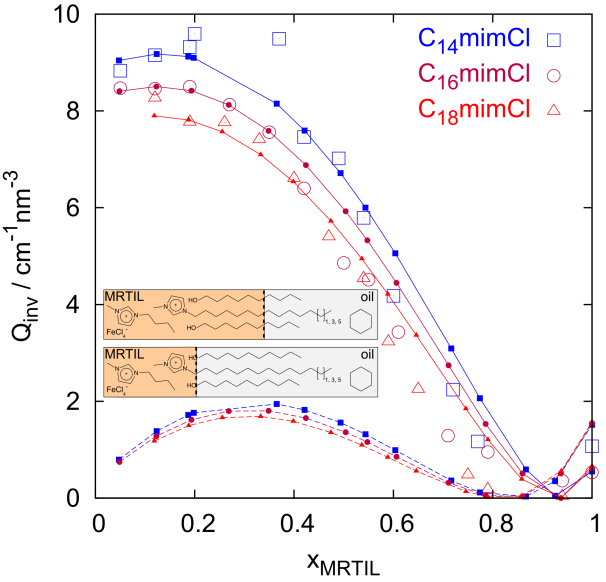

Figure 5.10 Scattering invariant Q_{inv} (open symbols) for C_{14}mimCl (squares), C_{16}mimCl (circles) and C_{18}mimCl (triangle) as a function of x_{MRTIL} derived from curves displayed in Fig. 5.8 with eq. 5.12. Small filled symbols are values calculated from sample composition with eq. 5.2d for the two cases of all (broken line) and only parts (straight lines) of the surfactant/alcohol CH_2-units counted to the oil phase. Inset cartoons illustrate the separation between oily and aqueous phase for these two cases.

values of the theoretical invariant Q_{inv} were calculated with eq. 5.2d. Although the sample compositions are fixed, the result is highly dependent on the assumption of the partitioning of the surfactant/cosurfactant chains between MRTIL and oil domain as this effects volume ratio and average scattering length density of both domains. Different possible distributions were calculated (for details see appendix B.3.1) that differ with respect to how much of the alkyl chain of the surfactant is counted into the hydrophobic part, and a comparison with experimental values is shown in Fig. 5.10. As the invariant value obtained by the Teubner-Strey fit is strongly effected by the fit quality, instead the experimental invariant was calculated by integration of the measured data by

$$Q_{inv} = \int_0^\infty I(q) q^2 \, \mathrm{d}q \tag{5.12}$$

where extrapolation to zero and infinity was done by the Guinier and Porod approximation, respectively (see appendix B.3.1 for details). In the oil rich region (small x_{MRTIL} values) a very good agreement is obtained for the case were the surfactant/alcohol alkyl chains are divided almost equally (6 and 7 C atoms of decanol and $C_j$mimCl surfactant, respectively, are counted into the polar phase; solid lines in Fig. 5.10). These results were confirmed by data recorded in a second SANS experiment (see description in appendix B.4) Going to the MRTIL richer region ($x_{MRTIL} \geq 0.4$) the experimental values start to deviate and have smaller values as predicted by this model. This can be explained by a less and less defined interface caused by a weaker mesoscopic structuring which is in good agreement with findings for ξ discussed above. For x_{MRTIL} values near 1 the experimental values can be better described by a model which counts all CH_2-groups to the oil phase. This is plausible as the portion of cyclohexane is getting more and more negligible compared to the amount of surfactant/decanol.

Additionally to the Teubner-Strey model a clipped random wave (CRW) model[111,112] was applied to the data. As the derived values for the lengthscale parameters D_s and ξ are nearly identical with the ones obtained by TS it is only described in detail in the appendix B.2. Nevertheless applying this model to the scattering data gives additional information as it delivers a third lengthscale (c) which accounts for the interfacial roughness. In the oil rich region (low x_{MRTIL}) this roughness parameter shows values comparable to water systems[112–114] (in our system they are slightly higher due to a higher surfactant concentration) and the trend of a growing roughness value with longer surfactant chains is as expected. Increasing the MRTIL content in the system gives continuously bigger c-values for all three systems which fits well to the general picture of a weakening of the mesoscopic structuring by increasing the MRTIL ratio. Above $x_{MRTIL} \approx 0.4$ the CRW-fits give random high numbers for c. This is due to the fact that the roughness parameter is not necessary anymore to simulate the SANS data (i. e. the fit quality is

independent from c) as the TS-model itself gives already excellent fit results. Also remarkable is the fact that the simple two phase model to explain the invariant (compare Fig. 5.10) as well fails above $x_{MRTIL} \approx 0.4$ which gives a hint to structural changes at this point.

5.1.3 Conclusion

The here presented study gives a detailed view on the phase behavior of C_4mimFeCl_4 containing microemulsions. As surfactants we employed different 1-alkyl-3-methylimidazolium chlorides with C_{14}, C_{16} and C_{18} chains, but as alone its amphiphilic strength was not high enough to form microemulsions, it was employed in a 1:2 ($C_i$mimCl/decanol) molar ratio with decanol as cosurfactant. Studies of the phase behavior showed that alcohols become increasingly effective as cosurfactants with increasing chain length, while the range of having monophasic microemulsions becomes at the same time smaller upon increasing the chain length of the oil. The variation of the surfactant chain length shows on the one hand a classical behavior expressed by an enhancement of solubilization strength or film rigidity with increasing chain length. On the other hand the effect is damped by the influence of the high amount of cosurfactant so that the surfactant chain length has nearly no effect on surface tension.
The SANS data can be well described with the Teubner-Strey model and show that microemulsion structures form most prominently in the region of $x_{MRTIL} = 0.2 - 0.6$. The degree of structuring increases with increasing chain length of the surfactant and the size of the structural domains increases largely upon approaching the emulsification failure. Values for κ, c (mean bending modulus and roughness parameter from the CRW model) and ξ are comparable with water systems in the oil rich region. With an increasing content of MRTIL all this parameters point to less and less structured systems with interpenetrating phases leading to a rough and less stiff interface with less pronounced long range ordering.
The here presented broad investigation yields quantitative information on the composition-structure relationship and therefore gives recipes to design

magnetic microemulsions with optimised properties and structures, as it has not yet been done for such systems that can be manipulated by a magnetic field. These findings are useful for designing strategies for formulating microemulsions of a given structure with MRTILs as polar component. This is important as such microemulsions could in the future be employed as interesting reaction media which contain also a component for separation via magnetic forces.

5.2 Microemulsions containing different MRTIL

In the following chapter the influence of MRTIL chain length on the microemulsion formation is investigated. To enhance clearity the number of varied compounds is reduced to one oil (cyclohexane) and one cosurfactant (1-decanol) as these two showed the best ability to form microemulsions in the C_4mimFeCl_4 system. Instead the chain length of the surfactant (n = 12, 14, 16 or 18) and MRTIL (n = 2, 4 or 6) were varied to have insight into the dependency of microemulsion phase behavior on molecule chain length in a more broad fashion.

5.2.1 Macroscopic observations

In Fig. 5.11 the resulting Kahlweit-fish phase diagrams are shown. The system based on C_4mimFeCl_4 was already discussed in detail in section 5.1.2 revealing that the ability to form microemulsions increases with longer surfactant alkyl chains expressed by a bigger three-phase region, a lower need of amphiphile, and a lower ratio of cosurfactant needed. The same trend can be observed in the C_2mimFeCl_4 based microemulsions when lengthening the surfactant chain from C_{12} to C_{18}. Additionally, when focussing on the effect of the MRTIL alkyl chain one can see a reverse trend of these quantities: For the microemulsion systems formulated with C_{18}mimCl as surfactant, the obtained three-phase region is getting bigger, less amphiphile is needed and

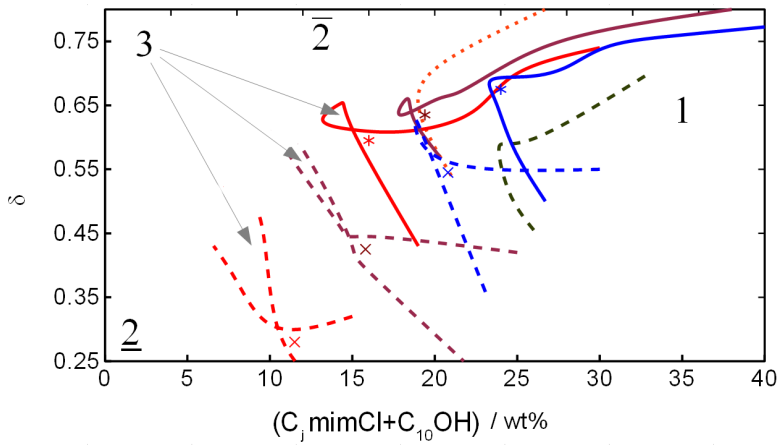

Figure 5.11 Kahlweit fish diagrams (volume ratio MRTIL/cyclohexane = 1:1) of all investigated microemulsion systems with C_2mimFeCl$_4$ (dashed lines), C_4mimFeCl$_4$ (straight lines) or C_6mimFeCl$_4$ (dotted lines) as polar phase and C_{12}mimCl (black), C_{14}mimCl (blue), C_{16}mimCl (purple) or C_{18}mimCl (red) as surfactant. For details see Appendix B. The crosses (for C_2mimFeCl$_4$ systems) and stars (for C_4mimFeCl$_4$ systems) show the sample positions for SANS investigation.

the ratio of cosurfactant is lower to obtain single phasic systems when shortening the alkyl chain from C_6 over C_4 to C_2 (red curves in Fig. 5.11). The same trend can be observed by using C_{16}mimCl (purple curves) or C_{14}mimCl (blue curves).

As a working hypothesis the effects provoked by surfactant and MRTIL chain length can be summarized in a dependency of the ability to self-assemble in the following form:

$$\propto j - i \tag{5.13}$$

where j and i are the alkyl chain length of the surfactant and MRTIL, respectively. Indeed this relation is valid for the fishtail position and is shown in Fig. 5.12 c. In general as well a few other values characterizing the aphiphilicity of the binary systems discussed in chapter 3, namely the *cmc*, the critical concentration to form liquid crystals (ϕ_{LC}) or the position of the Krafft discontinuity ($T_{Krafft,disc}$) can be described by the same relation as

plotted in Fig. 5.12, too.

The linear dependency of the free energy of micellization (which is proportionoal to $\ln cmc$) on the surfactant chain length was already mentioned in chapter 3.2.2 and was explained to have its origin in the transfer energy for one CH_2-group into the solvent. When this is true it is not surprising that the amount of lipophilic moieties in the solvent, quantified by the number of CH_2 groups in the solvent molecule, has the same effect but with opposite sign. It is now straightforward to link also the other values plotted in Fig. 5.12 to this transfer energy. Consequently the solubility of aliphatic alcohols in MRTIL as discussed in section 4.1 follows the same law (see table 4.1).

5.2.2 Mesoscopic structure

To investigate the mesoscopic structure, SANS measurements were done for samples whose positions within the phase diagrams are marked in Fig. 5.11. The positions were chosen to be in the monophasic regime close to the fish tail position to have a comparable mean curvature and as less excess amphiphile as possible for all systems. In Fig. 5.13 the resulting curves for all systems are shown. The findings here underline the trends which were concluded from the phase diagrams. The system C_2mim$FeCl_4$/C_{18}mimCl is expected to show the strongest amphiphilicity and indeed this system shows a well defined correlation peak. By shortening the surfactant alkyl chain, the peak first decreases and then completely vanished for C_{14}mimCl. Lengthening the MRTIL chain length gives a similar effect with respect to the surfactant chain length but in general the peak feature is damped as it is expected for systems with less long-range ordering. To extract quantitative values fits were done with the CRW model (for the model description see appendix B.2) and the resulting curves are additionally plotted in Fig. 5.13. The underlying parameters are listed in table 5.4. Here one can see that the trend expressed by eq. 5.13 is supported by the length parameter ξ which indicates the long range correlation between the microemulsion domains and which is increasing with surfactant and decreasing with MRTIL chain length. The trend for the domain size D_s is counter intuitive as it was already observed for the

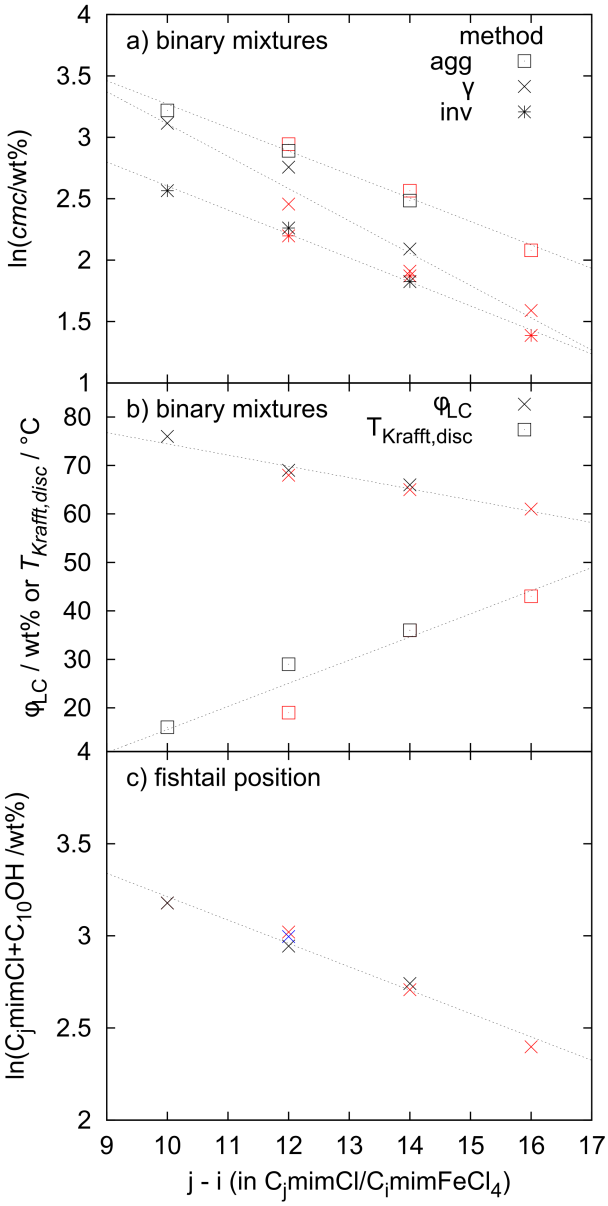

Figure 5.12 *cmc* derived from SANS arregation number (agg), scattering invariante (inv) and surface tension (γ) as summarized in table 3.1 (top), characteristic values derived from DSC-measurements in binary mixtures (middle) and the fishtail position in microemulsions (bottom) as a function of the alkyl chain length difference between surfactant and MRTIL. The colors indicate the solvent being C_2mimFeCl$_4$ (red), C_4mimFeCl$_4$ (black) or C_6mimFeCl$_4$ (blue). The lines are linear fits.

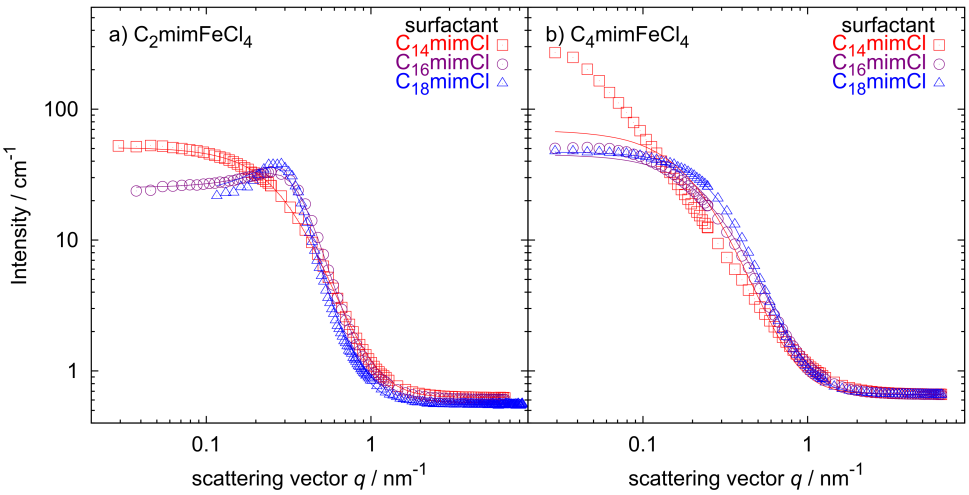

Figure 5.13 Scattering curves for all microemulsion systems, formulated with H12-cyclohexane as oil, The MRTIL is C_2mimFeCl$_4$ (left) or C_4mimFeCl$_4$ (right). For sample positions see Fig. 5.11. Straight lines are fits with the CRW-model. The underlying parameters are listed in table 5.4.

C_4mimFleCl$_4$ system earlier (see chapter 5.1.2) showing bigger structures for shorter surfactant chain length. For the C_4mimFeCl$_4$/C_{14}mimCl systems this leads even to sizes beyond the observation limit making it impossible to fit with the CRW-model.

Contrast variation

To evaluate the mesoscopic structure of the microemulsions in a more detailed fashion, for the sample positions given in Fig. 5.11 a contrast variation study was performed. For this reason for each position five different levels of oil deuteration were measured (pure H12-, 25% D12-, 50% D12-, 75% D12- and pure D12-cyclohexane). The resulting spectra are plotted in Fig. 5.14.

With the present number of components and consequential high number of degrees of freedom in the present systems, to get quantitative information on the distribution of the different compunds (i. e. the surfactant and cosurfactant) it would be deemed necessary to have a reliable value for $I(q \to 0)$ and the scattering invariant for each system.[115,116] The first requirement is

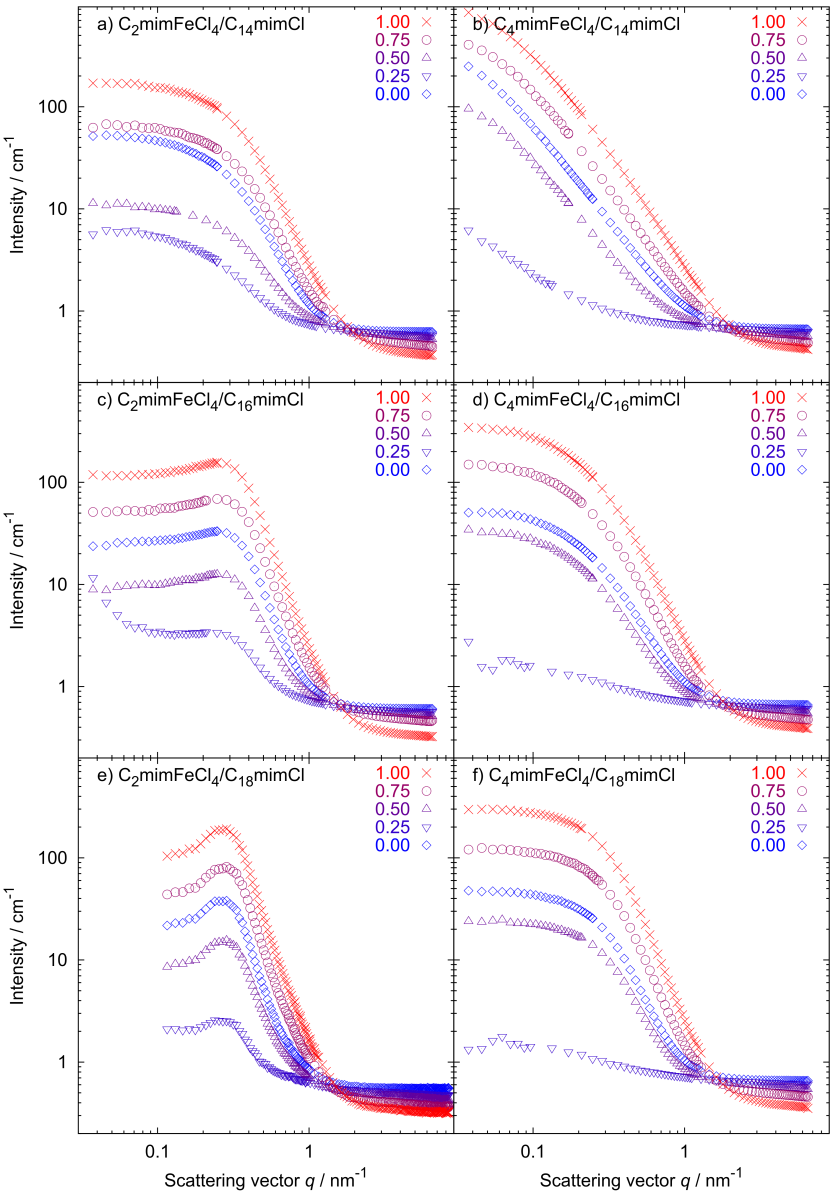

Figure 5.14 SANS curves for samples at positions in the phase diagram as indicated in Fig. 5.11. In all graphs the key indicates the ratio of deuterated cyclohexane in the oil phase.)

Table 5.4 Results from CRW-fits for curves shown in Fig. 5.13. Values for the system C_4mimFeCl$_4$/C_{14}mimCl are set in brackets due to its bad matching with experimental data.

$C_x$mimFeCl$_4$	$C_y$mimCl	CRW-Model					Porod/Guinier
		ξ/nm	D_s/nm	Q_{inv}/cm^{-1}nm^{-3}	c/nm	BG/cm^{-1}	Q_{inv}/cm^{-1}nm^{-3}
4	14	(3.89)	(300)	(0.83)	(5)	0.664	1.83
4	16	2.98	529	1.25	12	0.663	1.88
4	18	3.88	37	1.31	> 25	0.658	1.55
2	14	3.24	44	1.64	15	0.626	1.51
2	16	5.50	21	1.67	> 25	0.606	1.45
2	18	7.20	22	1.25	> 25	0.551	0.85

at least difficult for the system C_4mimFeCl$_4$/C_{14}mimCl as the measured intensities do not converge to a plateau for low q-values. To extract the latter one, additionally to this an extrapolation to high q-values is necessary. As already discussed in chapter 4.2 and 5.1.2, this is as well difficult due to distracting scattering from cyclohexane on the one hand and eventually present monomerically decanol dissolved in the oil phase. Due to these difficulties the results of the contrast variation experiments are analyzed only qualitatively to avoid an over-interpretation of the data.

As one can see for all six systems, a variation of the cyclohexane scattering length density from $6.68 \cdot 10^{-4}\,\mathrm{nm}^{-2}$ (100 % D12-cyclohexane) to $-0.28 \cdot 10^{-4}\,\mathrm{nm}^{-2}$ (100 % H12-cyclohexane) lets pass the scattering intensity through a minimum as to be expected around the value for the MRTIL ($1.83{\cdot}10^{-4}\,\mathrm{nm}^{-2}$ and $1.55 \cdot 10^{-4}\,\mathrm{nm}^{-2}$ for C_2mimFeCl$_4$ and C_4mimFeCl$_4$, respectively). For the case of a well defined interface of hydrocarbon chains between the oil and MRTIL domains, different parts of the microstructure would be visible as a function of the oil SLD. As illustrated schematically in Fig. 5.15 for three different cases, using pure H12-cyclohexane nearly matches the surfactant interface (left), adjusting MRTIL and oil to the same density would make only the interface visible (middle) and the use of pure D12-cyclohexane gives

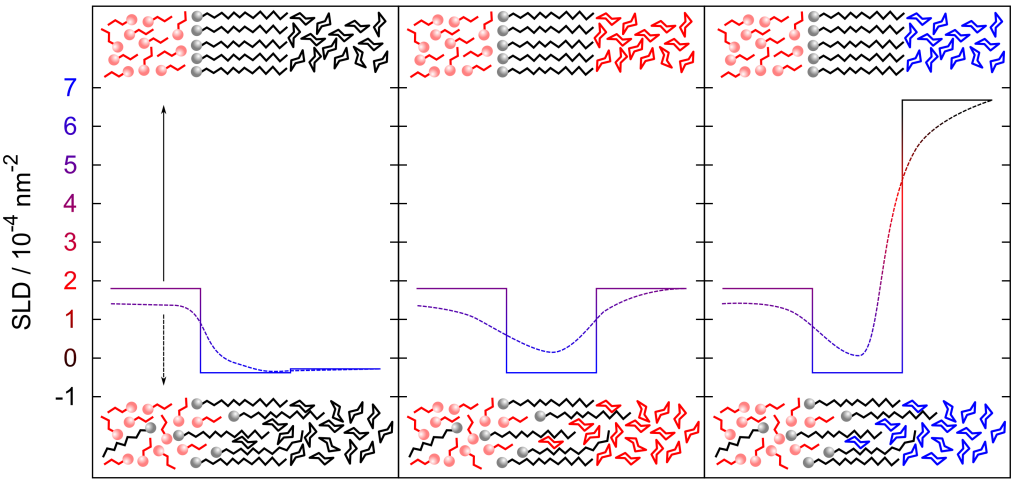

Figure 5.15 Scattering length density profile of the interfacial film for three cases: The surfactant is contrast matched by the pure H12-cyclohexane (left), oil and MRTIL are contrast matched (middle) and different levels for oil, MRTIL and interface when using pure D12-cyclohexane (right). The profiles are given for the assumption of sharply separated domains (straight lines, illustrated by the cartoons above the graphs) and a partly interpenetration (broken lines, illustrated by the cartoons under the graphs)

a 3-level profile of oil, MRTIL and interface domain (right). Consequently this results in completely differently appearing SANS spectra as a function of the oil SLD variation, which is indeed commonly observed for microemulsions.[117–119] The data presented in Fig. 5.14 do not show any variation beside the scattering originating by the cyclohexane molecules at high q and a scaling factor due to the overall contrast. This suggest a lack of well defined microphases. In Fig. 5.15 the SLD-profile is additionally shown assuming a partial monomerical solubility of the surfactant in the MRTIL (which lowers the SLD of the polar domain) and a partial interpenetration of the interface by MRTIL and oil. This smearing out of the interface results in a SLD profile which would then accord with the measured data. This findings underline the picture drawn in the earlier sections which characterizes the microemulsions by oil and MRTIL domains separated by a rough and poorly sharp interface.

5.3 Magnetic behaviour

5.3.1 Field Gradient

Due to its paramagnetic nature, the MRTIL is per definition attracted by a magnetic field, a behavior which was already discussed in the introduction and this is demonstrated by the ability to move a macroscopic MRTIL phase with a magnet. Going from a macroscopic portion to micron-sized MRTIL droplets as it is given in an emulsion, this driving force is still valid, although the forces which stabilize an emulsion are now appearing as opponents.

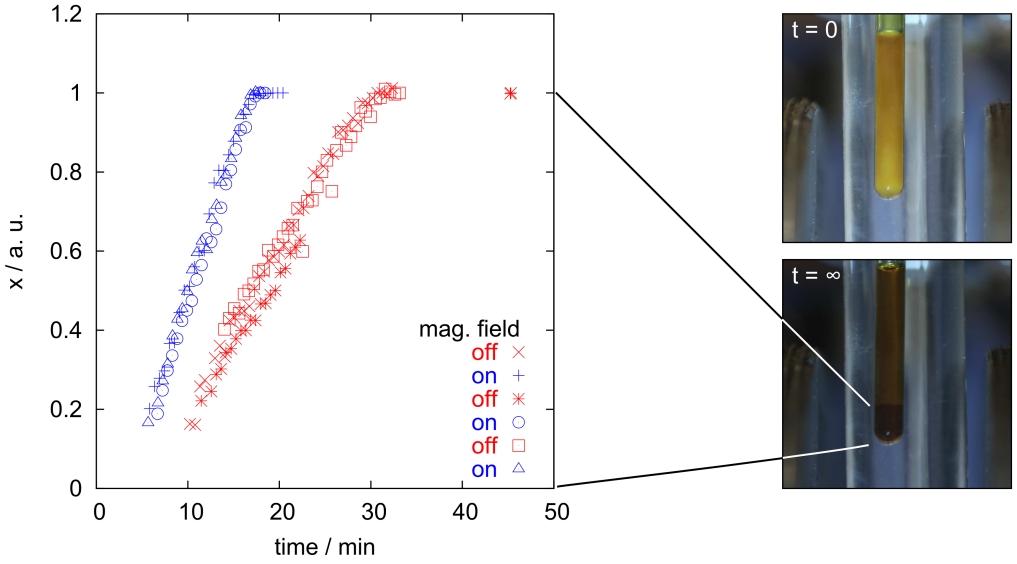

Figure 5.16 Left: Sedimentation measurements with (blue) and without (red) a magnetic field gradient to investigate the emulsion stability. The emulsion is composed of cyclohexane (17.4 wt%) , C_4mimFeCl$_4$ (60.4 wt%), decanol (11.2 wt%) and C_{18}mimCl (11.0 wt%). **Right:** Image of the emulsion directly after dispersion with a vortex mixer (top) and after complete demixing (bottom).

Fig. 5.16 shows an emulsion formed by immiscible cyclohexane and C_4mimFeCl$_4$, stabilized by C_{18}mimCl. This emulsion is only weakly kinetically stable as indicated by a relatively fast phase separation into a lower MRTIL phase and an upper microemulsion phase. Under ambient conditions at zero magnetic field this process is completed after around 30 min. The

phase separation velocity (v_{sep}) was measured quantitatively by measuring the height of the precipitate phase as a function of time.

$$v_{sep} = \frac{\mathrm{d}V}{\mathrm{d}t} = A\frac{\mathrm{d}x}{\mathrm{d}t} \tag{5.14}$$

with V and x being the volume and relative height of the lower MRTIL phase, respectively, and A being the cross-section of the sample vial. This sedimentation is in a simple approximation related to Stokes law which describes the sedimentation velocity v_s as a function of droplet radius R, solvent viscosity η and the density difference between them ($\rho_{drop} - \rho_{solv}$):

$$v_s = \frac{2R^2(\rho_{drop} - \rho_{solv})g}{9\eta} \tag{5.15}$$

The underlying force can be expressed as:

$$F_{grav} = \frac{4}{3}\pi R^3(\rho_{drop} - \rho_{solv})g \tag{5.16}$$

Here g is the acceleration due to gravity. By exposing to a field gradient the separation kinetic is enhanced by a factor of around 2. This can be expressed by a second force term (F_{mag}) added to F_{grav} which is dependent on the difference in volume magnetic suszeptibility χ and the magnetic field gradient (∇B):

$$F_{mag.} = \frac{4}{3}\pi R^3(\chi_{drop} - \chi_{solv})\frac{B(\nabla B)}{\mu_0} \tag{5.17}$$

The mentioned enhancement of the separation kinetics by a factor of 2 consequently is due to the condition $F_{grav} = F_{mag}$ which indeed can be calculated for the given system as demonstrated in the appendix B.11.

A MRTIL containing microemulsion still keeps a paramagnetic behaviour which can be seen by the fact that the meniscus can be manipulated by a magnetic field gradient as shown in Fig. 5.17 and this applies to the whole microemulsion range that contains at least a few percent of MRTIL. This is due to the paramagnetic behaviour of the complete macroscopic sample and can be explained analogously to the pure MRTIL. The magnitude of

the meniscus deformation scales with the average susceptibility of the whole sample and makes no statement about the microstructure. Nevertheless the stabilizing forces of the microstructure are far higher than in an unstable emulsion (see eq. 5.17 where the sedimentation force induced by a field gradient scales with R^3) and at the given fields the microemulsion can not be broken.

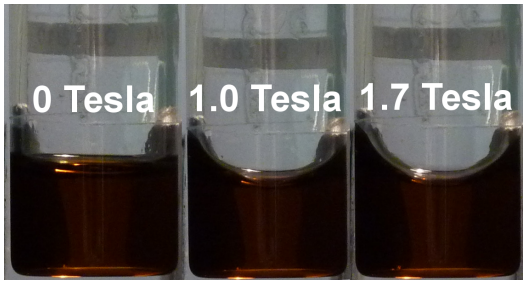

Figure 5.17 Response of the MRTIL containing microemulsion to the field gradient of an electromagnet. The sample shown consists of 31.2 wt% D12-cyclohexane, 46.1 wt% C_4mimFeCl$_4$, 11.8 wt% C_{16}mimCl and 10.9 wt% decanol. The magnetic field is oriented parallel to the liquid surface.

5.3.2 Homogeneous field

A quantitative insight in the magnetic behaviour of the microemulsions has been gained by measurements of the magnetic susceptibility, which were done along the dashed line given in Fig. 5.18 covering the full range from the pure oil to pure MRTIL as solvent. All samples show a paramagnetic behavior indicated by a linear field dependence of the magnetization plotted in Fig. 5.18. The magnetic susceptibility shown in Fig. 5.19 increases in almost perfect linear fashion with the increasing weight content of the MRTIL, which means that the magnetic properties of the microemulsion are not affected by its mesoscopic structure which confirms the findings under a field gradient discussed in section 5.3.1. Extrapolation to pure C_4mimFeCl$_4$ gives a magnetic susceptibility of $40 \cdot 10^{-6}$ emu/g. For comparison the initial susceptibility of ferrofluids can be found to be of the order of 10^4 times higher.[120] In fact the magnetic susceptibility is dimensionless but can be defined by

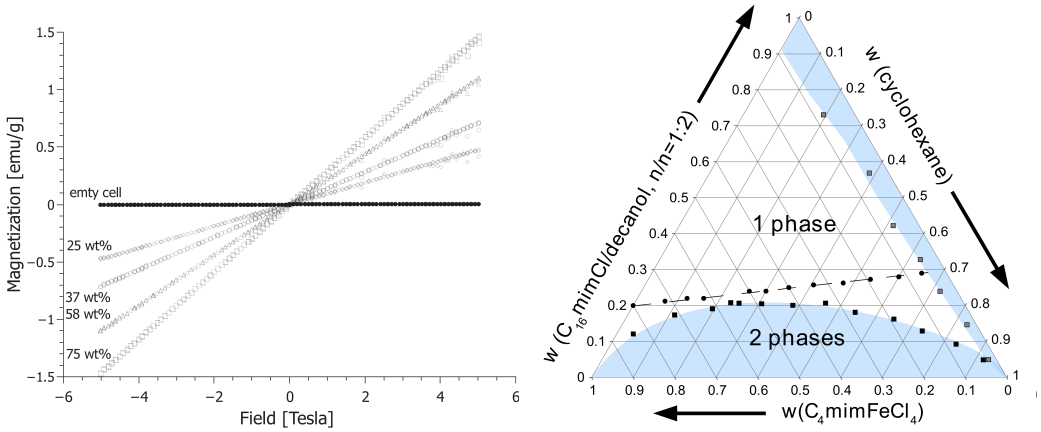

Figure 5.18 left: Example SQUID measurements of the microemulsions and the emty cell at 300 K. The labels indicate the wt% of MRTIL in the sample. **right:** Location within the phase diagram (dots) of the samples given the results showed on the left.

different systems of units and related to mole, mass or volume, which is often not clearly labeled in literature, and this can lead to some confusion. For this reason in table 5.5 the magnetic suszeptibility is given for different definitions.

Table 5.5 Magnetic suszeptibility calculated due to the definitions given by the SI and EMU system of units, with respect to the sample mass (χ_g), volume (χ_v) or molar amount (χ_m) with the relation $\chi_v = \chi_g\rho = \chi_m\rho/M$, whereby ρ and M are the density and molar mass, respectively. Values for cyclohexane are taken from literature.[121]

	χ_g		χ_m		χ_v	
	SI	EMU	SI	EMU	SI	EMU
C_4mimFeCl$_4$	$5.0 \cdot 10^{-7}$	$4.0{\cdot}10^{-5}$	$1.7{\cdot}10^{-7}$	$1.4{\cdot}10^{-2}$	$6.8{\cdot}10^{-4}$	$5.4{\cdot}10^{-5}$
cyclohexane	$-1.0{\cdot}10^{-8}$	$-8.1{\cdot}10^{-7}$	$-8.6{\cdot}10^{-10}$	$-6.8{\cdot}10^{-5}$	$-7.9{\cdot}10^{-6}$	$-6.3{\cdot}10^{-7}$

Considering the orientation of microscopic domains in a homogeneous magnetic field this can be described by two different mechanisms:[122]

1. With the existence of an **intrinsic anisotropy** of the magnetic suscep-

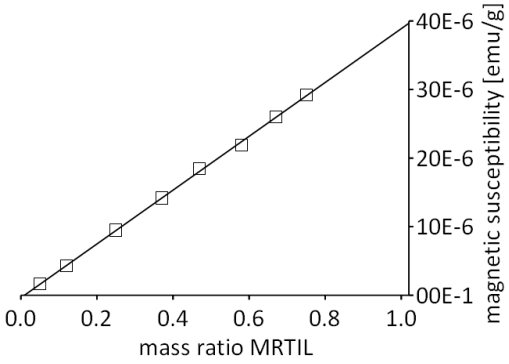

Figure 5.19 Mass magnetic susceptibility as a function of wt% MRTIL. Measurements were done along the experimental path shown in Fig. 5.18.

tibility of the material. (For that χ has to differ at least for two geometrical axes.) the orientation of the highest susceptibility parallel to the magnetic field minimizes the magnetic energy by $E = 0.5V\Delta\chi\frac{B^2}{\mu_0}cos^2\theta$, with θ as the angle between the axis of the lowest susceptibility and the applied magnetic field.

2. When having objects with a **shape anisotropy**, orientation of the longest axis parallel to the magnetic field minimizes the magnetic energy due to the so-called demagnetization effect.

To find out if the mesoscopic structure of the microemulsion systems can be manipulated by a magnetic field, neutron scattering was done under magnetic field. In case of an influence of the magnetic field on the microemulsion domain size, spontaneous curvature or film rigidity this should be seen in a change in the (isotropic) spectra shape. A complete destabilization (passing the phase boundary to a multi-phase region) would not imperatively be seen in the scattering pattern. Instead of that due to the slow remixing of a phase separated system in a cuvette of 1 mm thickness, this case is believed to be at least recognized after a measurement cycle during sample changing. In case of an orientation parallel or perpendicular to the field the two-dimensional detector image would show an anisotropic pattern. In Fig. 5.20 the location of the samples in the phase diagram are shown. These samples were scanned

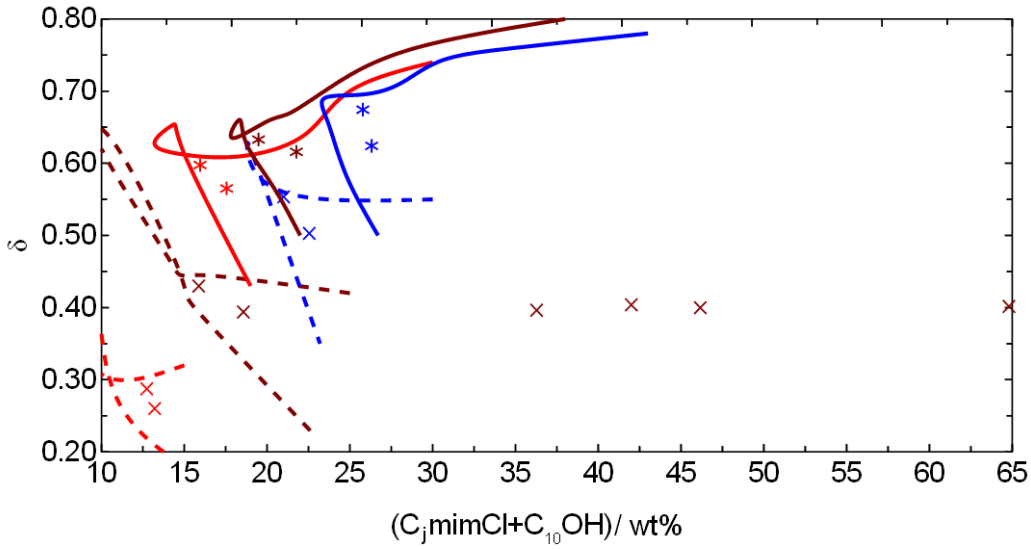

Figure 5.20 Kahlweit fish diagrams of all investigated microemulsion systems with C_2mimFeCl$_4$ (dashed lines) or C_4mimFeCl$_4$ (straight lines) as polar phase and C_{14}mimCl (blue), C_{16}mimCl (purple) or C_{18}mimCl (red) as surfactant. The crosses (for C_2mimFeCl$_4$ systems) and stars (for C_4mimFeCl$_4$ systems) show the sample positions for samples investigated with SANS under magnetic field. δ accounts for the ratio between cosurfactant and surfactant and is defined by eq. 5.1.

at fields of 0, 2, 4 and 8 T. The location within the phase diagram were mainly chosen to be near the fish tail to have as little excess surfactant as possible and to have as big structures as possible. Additionally several samples in the oil rich region were measured. All samples measured under magnetic field can be found in the appendix B.6. Because these samples and all the microemulsion samples showed no effect by the applied magnetic fields, the spectra are not discussed furthermore here. As shown in Fig. 5.20, for the system C_2mimFeCl$_4$/C_{16}mimCl a series at constant surfactant/decanol-ratio and with different surfactant ratios was done. In the following this series is described in more detail.

At a starting point the mesoscopic structure along this experimental path at zero magnetic field was investigated and a first insight into that is already given by a simple observation with crossed polarizers which is shown in Fig. 5.21. While the samples at lower surfactant concentrations are opti-

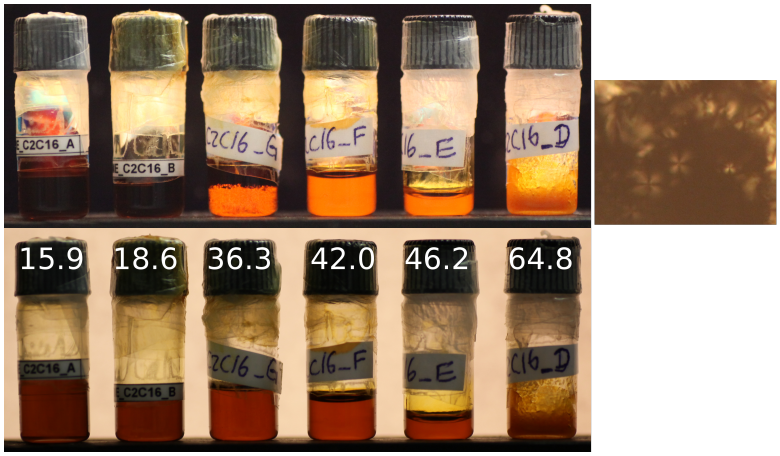

Figure 5.21 Photographs of samples for the system C_{16}mimCl/C_2mimFeCl$_4$ between (top) and without (bottom) cross-polarizers. for position in the phase diagramm see Fig. 5.20. The Labels indicate the wt% of surfactant+decanol in the sample. It should be mentioned that the sample at 64.8 wt% shows a macroscopic phase separation. The sample at 36.3 wt% is only partly birefringent due to an ongoing slow transition after shaking. The picture on the right is a polarized microscopy image of the sample at 42.0 wt%.

cal isotropic and easy-flowing which points to microemulsion structures, the higher concentrated samples are gels and optically birefringent. Observation of these samples in thin layers under polarized microscopy identifies these samples as lamellar liquid crystals. The sample at 36.3 wt% shows birefringence which vanished by shaking the sample and the structure is reversibly build up again after some minutes of resting. This is a hint to a thixotropic behaviour, or a shear induced phase transition. It should be mentioned that usually surfactant systems are known to show a shear induced transition from an isotropic to a lamellar phase and the here reported behaviour shows the reverse direction.[123,124]

The observed SANS spectra of these samples at zero magnetic field are shown in Fig. 5.22. All samples show a correlation peak which becomes sharper and is shifted to higher q values with increasing surfactant concentration. Including the macroscopically observed behaviour (fluidity, birefringence) this can be interpreted as a smooth transition from a low viscous, optically isotropic microemulsion at low surfactant concentration to a high

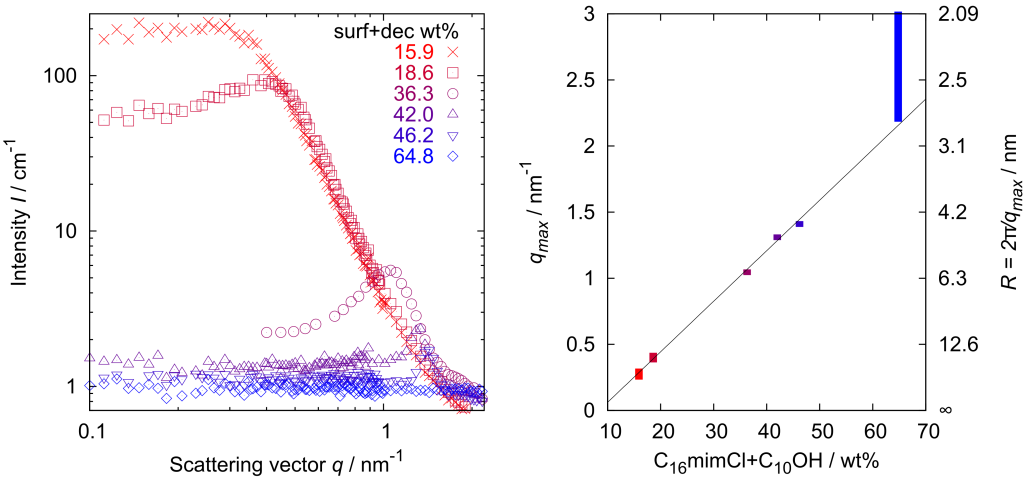

Figure 5.22 left: SANS curves for microemulsion systems C_{16}mimCl/C_2mimFeCl$_4$, for the location in the phase diagram see Fig. 5.20 **right:** peak position vs. surfactant concentration. (The symbol for 64.8 wt% expresses $q \geq 2.1\,\mathrm{nm}^{-1}$ because no peak was observed within the observation range ending at this q-value.)

viscous (gelly), birefringent (lamellar) liquid crystal phase at high concentration. From the peak position q_{max} a length scale $R = 2\pi/q_{max}$ for these structures can be calculated and is as well shown in Fig. 5.22. Of high interest is the transition area between these two well defined structures because next to the sample with a shear dependent structuring (observed by polarized microscopy) at 36.3 wt%, the sample at 42.0 wt% is the only mixture responding to the exposed magnetic field. The 2D detector image at 2 m of this sample under a magnetic field of 8 Tesla is shown in Fig. 5.23 and shows a clear orientation in the magnetic field.

To get a quantitative value for the anisotropy of the scattering pattern (which is a measure of the degree of orientation in the magnetic field), the detector image was averaged slice-wise as shown in Fig. 5.23. The shown resulting 1D-spectra for an isotropic sample (at 0 Tesla) are identically independent on the azimuthal angle, an orientation (8 Tesla) leads to spectra with different peak amplitudes dependent on the azimuthal angle while the peak position is not affected and stays constant for different azimuthal angles. In

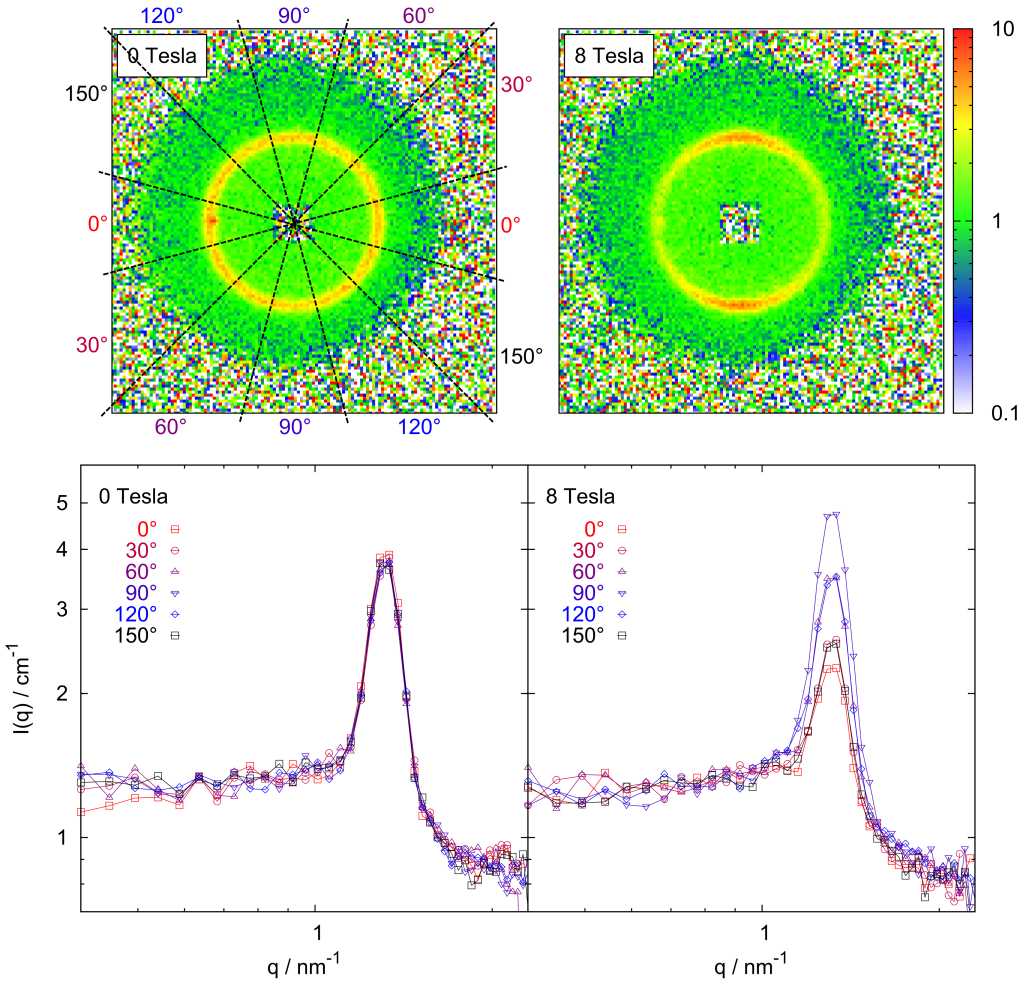

Figure 5.23 upper row: 2D-detector images (2 m sample to detector distance) of the sample with 42.0 wt% surfactant+decanol (for the position in the phase diagram see Fig. 5.20) at different times during the field-ramp experiment. Triangles indicate the pixels which were averaged. **bottom row:** Resulting q dependent 1D-spectra by performing a slice-wise averaging.

Fig. 5.24 (inset) the intensity of the scattering peak (at $q = 1.3\,\mathrm{nm}^{-1}$) is plotted for different magnetic fields and accordingly shows no variation with respect to the azimuthal angle at a field of 0 T. Two maxima appear with increasing magnetic field at an angle of 90° and 270° due to the orientation in the magnetic field. Additionally several alternative values to estimate the relative anisotropy were calculated with the help of the program SASET[73] (for details see chapter 2.7.1).

The freshly homogenized sample (by heat) was then investigated while applying different magnetic fields. Results are shown in Fig. 5.24. At an inital field free measurement the sample shows spectra whose peak amplitudes are independent from the analyzed detector angle which indicates a statistical random distribution. Rising the magnetic field in a rate of 0.2 T/min first doesn't change this behavior which indicates that the force on the mesoscopic domaines induced by the magnetic field is to weak. Above a critcal field of around 5.5 T (here, of course, a small temporal retardation might be present) the sample starts to become more and more anisotropic and this effect is proportional to the rising field. Holding then the field constant at a value of 8 T the anisotropy still increases but on a much smaller timescale. When then applying a field ramp back to 0 T, a slow relaxation of the anisotropy is visible but even after hours the sample still shows an anisotropy. This behaviour can be interpreted by three different processes: Starting above the critical field strength, the resulting magnetic force is strong enough to overcome the (sterical) hindrance to move domains, this process (I) is fast and proportional to the magnetic field. At a constant field above the critical field (in our experiment 8 T) a second process (II) of orientation is visible which has a much slower kinetic rate. Finally the relaxation below the critical field value back to the isotropic state (III) should be due to thermal fluctuations and is therefore much slower. For process I it is difficult to extract quantitative kinetic values as the magnetic field is not constant, for II and III, by applying a simple single-exponential law as done with eq. 5.18 and 5.19, respectively, one can estimate the range of characteristic times for these processes.

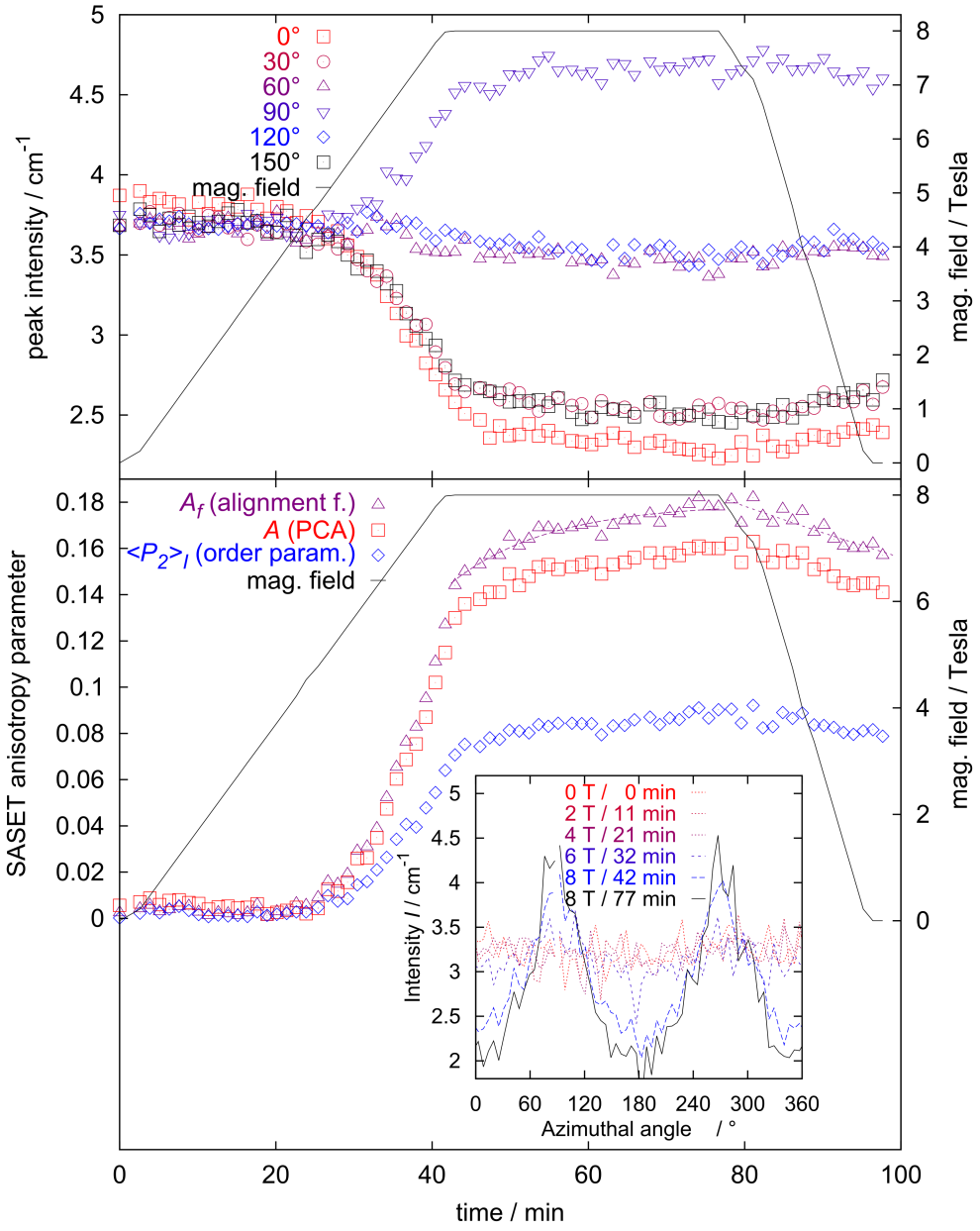

Figure 5.24 Parameters to represent a change in sample anisotropy vs. time while applying a magnetic field profile. **top:** Peak-maxima from 1D-spectra extracted by a slicewise analysis of the 2D-detector images as described in Fig. 5.23. **bottom:** Different parameters quantifying the anisotropy as determined with the program SASET. Details are described in chapter 2.7.1. Lines are fits with eq. 5.18 (broken line) and 5.19 (dotted line) with parameters listed in table 5.6. **inset:** Averaged intensity for the radial segment of $1.25\,\mathrm{nm}^{-1} \leq q \leq 1.43\,\mathrm{nm}^{-1}$ as a function of the azimuthal angle for selected magnetic fields.

$$\text{II:} \quad A = A_\infty - (A_\infty - A_0) \cdot \exp\left[\frac{t_0 - t}{\tau_2}\right] \tag{5.18}$$

$$\text{III:} \quad A = A_0 \cdot \exp\left[\frac{t_0 - t}{\tau_3}\right] \tag{5.19}$$

Here it is assumed that the alignment factor A_f is proportional to the amount of aligned domains, A_0 and A_∞ are the alignment factor at time t_0 and infinity, respectively. Fit results are given in table 5.6. Although the underlying data is quite incomplete to make substantiated statements, it gives an estimate for the maximum alignment at 8 T (A_∞) and a difference in the rate of process II and III of about a factor of 10.

Table 5.6 Fit parameters derived when applying eq. 5.18 and 5.19 to the alignment factor (A_f) shown in Fig. 5.24.

	fit range/min	t_0/min	A_0	A_∞	τ/min
II	$42 - 77$	42	0.14	0.18	12.6
III	$77 - 100$	77	0.18	–	150.2

Process III can be interpreted as a rotational diffusion of the aligned domains back to the random isotropic state. The corresponding rotational diffusion coefficient ($D_r^\perp$) can be calculated via eq. 5.20. Assuming a simple cylindrical or disk-like shape of the rotating domains, characterized by a width length (L) and a diameter (d), the order of the size of the domains can be estimated via eq. 5.21.[125]

$$D_r^\perp = \frac{1}{6\tau_3} = 1.85 \cdot 10^{-5}\,\mathrm{s}^{-1} \tag{5.20}$$

$$= 3\frac{kT(\ln p - 0.662 + 0.917/p - 0.050/p^2)}{\pi\eta_0 L^3} \tag{5.21}$$

Here $p = L/d$ is the aspect ratio and η_0 is the viscosity of the solvent. In Fig. 5.25, values for L and d are plotted for different aspect ratios, which

fulfill eq. 5.21. It can be seen that from this model domain sizes in the range of micrometers are predicted.

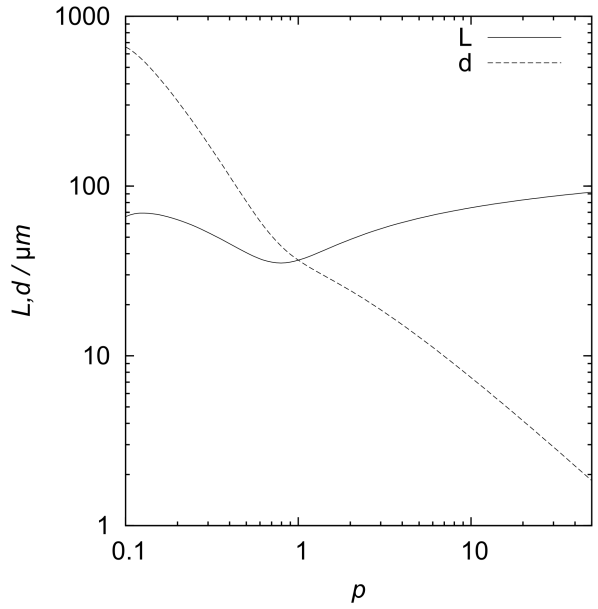

Figure 5.25 Values for L and d as a function of the aspect ratio p, which are fulfilling eq. 5.21. As solvent viscosity the value for cyclohexane $\eta_0 = 0.89\,\mathrm{mPas}$ was used.[126]

The fact that only the sample at 42.0 wt% was able to orient in the field could be explained due to a coincide of structure domains which are big and stiff enough to produce a reasonable field induced force which can compete against Brownian motion with a not to viscous sample (due to not too big domains) to make the domains still able to move and orient in the magnetic field in a reasonable time. Naturally although these conclusions are based on a weak empirical foundation and the experiments should be verified by a more detailed study, the results can be seen as a starting point and a working hypothesis on which ongoing research can build up in the field of systems based on MRTILs, where the orientation of a LC phase and thereby the optical properties are controlled by the magnetic field.

6

Conclusion

In this work the surfactant self-assembly in a nonaqueous system was investigated, realized by using different alkylmethylimidazolium tetrachloroferrates ($C_i$mimFeCl_4 with i = 2, 4, 6) as solvent and imidazolium based surfactants ($C_j$mimCl with j=12, 14, 16, 18) as amphiphile.

In a systematic fashion the phase behavior was studied. For this purpose we started with the simplest case of binary IL/surfactant mixtures where the alkyl chain length of surfactant and IL was varied over a broad temperature range and the complete range of compositions. In this way it was possible to find classical mesoscopic structures like micelles and liquid crystalline structures. The complexity was extended by adding oil and cosurfactant to the system which enabled us to formulate microemulsions. Again the influence of surfactant and IL alkyl chain lengths on the phase behavior was investigated and additionally the investigation was broadened by a wide variation of the structure and amount of the cosurfactant and oil. To ensure an as substantive and reliable picture as possible it was made use of many comple-

mentary methods as calorimetry (DSC), polarized microscopy, neutron and X-ray scattering (SANS/SAXS), and surface tension.

In general it was proven that it is possible to form typical self-assembled structures in this IL-based matrix like micelles, liquid crystals, emulsions and microemulsions as they are common for classical aqueous systems. However in difference to the latter ones it was shown that the ability to self-assemble is weaker which is expressed e. g. by higher critical aggregation concentrations leading to micelles with rather low aggregation numbers and which are partly swollen by the solvent, or smaller tri-phasic regions for microemulsions, in which the mesoscopic domains show a less pronounced long range ordering.

For the formulated microemulsions it was found that they were only to be formed when adding a cosurfactant. Here a broad range of different branched and aliphatic alcohols was investigated whereby the efficiency to form single-phasic systems was found to scale with the alkyl chain length of the alcohol while the range of having monophasic microemulsions becomes at the same time smaller upon increasing the chain length of the used aliphatic oil. Furthermore cyclohexane showed outstanding quality for the microemulsion formulation. The variation of the surfactant chain length shows a classical behavior expressed by an enhancement of solubilization strength and film rigidity with increasing chain length. Values for κ, c (mean bending modulus and roughness parameter from the CRW model, respectively) and ξ are comparable with water systems in the oil rich region. With an increasing content of MRTIL all this parameters point to less and less structured systems with interpenetrating phases leading to a rough and less stiff interface with less pronounced long range ordering. The local separation between the hydrophilic and hydrophobic domains in the microemulsion was found to be along a surface which divides the surfactant/alcohol alkyl chains almost equally between them.

The weakness in self-assembly was quantified by the solvophobic effect of the alkyl chain which is in the MRTIL only about a fifth of that in water. It was distinguished between the effects of the solvophobic and -philic part of the surfactant and as a result it was quantitatively shown that deficits in the ability to self-assemble are mainly present in the surfactant's solvophobic

tail. Two opposed trends for the amphiphilic strength could be pointed out given on the one hand by the length of surfactant alkyl chains which quantifies the solvophobicity of the amphiphile, and on the other hand by the length of MRTIL alkyl chains, which quantifies the solvent polarity. It could be shown, that this can be expressed by the working hypothesis $\propto j - i$ (with j and i as the number of methylene groups in the surfactant and MRTIL chains, respectively) whose proportionality is followed by a lot of values characterizing the amphiphilicity of the different systems, such as the *cmc*, the critical concentration to form liquid crystals or the fish tail position in microemulsions.

As for this study ionic liquids with paramagnetic properties were chosen, it was proven that this property is still present in the formulated microemulsion systems. As a second result it was possible to orient mesoscopic structures in an external magnetic field. However this was only possible for certain locations in the phase diagrams where a lamellar phase was present and at rather high magnetic fields of ≥ 5.5 Tesla.

In summary, the here presented broad investigation yields quantitative information on the composition-structure relationship and therefore gives recipes to design magnetic self-assembled structures with optimised properties and structures, as it has not yet been done for such systems that can be manipulated by a magnetic field. These findings are useful for designing strategies for formulating microemulsions of a given structure with MRTILs as polar component. This is important as such microemulsions or emulsions could in the future be employed as interesting reaction media which contain also a component for separation via magnetic forces.

References

[1] Tanford, C. *Science* **1978**, *200*, 1012–1018.

[2] Tanford, C. *The hydrophobic effect: formation of micelles and biological membranes*, 2nd ed.; Wiley Interscience Publications; Wiley, 1980.

[3] Griffin, W. C. *J. Soc. Cosmet. Chem.* **1949**, *1*, 311–326.

[4] Salager, J.-L.; Marquez, N.; Graciaa, A.; Lachaise, J. *Langmuir* **2000**, *16*, 5534–5539.

[5] Helfrich, W. *Z. Naturforsch.* **1973**, *28c*, 693–703.

[6] Kunz, W.; Testard, F.; Zemb, T. *Langmuir* **2008**, *25*, 112–115.

[7] Kumar, P. In *Handbook of microemulsion science and technology*; Kumar, P., Mittal, K. L., Eds.; Dekker, 1999; p 849.

[8] Duvail, M.; Dufreche, J.-F.; Arleth, L.; Zemb, T. *Phys. Chem. Chem. Phys.* **2013**, *15*, 7133–7141.

[9] Handy, S. T. *Curr. Org. Chem.* **2005**, *9*, 959–988.

[10] Chen, Y.; Zu, Y.; Fu, Y.; Zhang, X.; Yu, P.; Sun, G.; Efferth, T. *Molecules* **2010**, *15*, 9486–9495.

[11] Duan, Z.; Gu, Y.; Deng, Y. *Catal. Commun.* **2006**, *7*, 651–656.

[12] Olivier-Bourbigou, H.; Magna, L.; Morvan, D. *Appl. Catal., A* **2010**, *373*, 1–56.

[13] Yoshida, Y.; Saito, G. *Phys. Chem. Chem. Phys.* **2010**, *12*, 1675–84.

[14] Mallick, B.; Balke, B.; Felser, C.; Mudring, A. V. *Angew. Chem., Int. Ed.* **2008**, *47*, 7635–7638.

[15] Chen, Z.; Zhang, S.; Qi, X.; Liu, S.; Zhang, Q.; Deng, Y. *J. Mater. Chem.* **2011**, *21*, 8979–8982.

[16] Hayashi, S.; Hamaguchi, H. *Chem. Lett.* **2005**, *34*, 740–740.

[17] Del Sesto, R. E.; McCleskey, T. M.; Burrell, A. K.; Baker, G. A.; Thompson, J. D.; Scott, B. L.; Wilkes, J. S.; Williams, P. *Chem. Commun.* **2008**, 447–449.

[18] Krieger, B. M.; Lee, H. Y.; Emge, T. J.; Wishart, J. F.; Castner, E. W., Jr. *Phys. Chem. Chem. Phys.* **2010**, *12*, 8919–8925.

[19] Peppel, T.; Kockerling, M.; Geppert-Rybczynska, M.; Ralys, R. V.; Lehmann, J. K.; Verevkin, S. P.; Heintz, A. *Angew. Chem., Int. Ed.* **2010**, *49*, 7116–7119.

[20] Plechkova, N. V.; Seddon, K. R. *Chem. Soc. Rev.* **2008**, *37*, 123–150.

[21] Kokorin, A., Ed. *Ionic Liquids: Theory, Properties, New Approaches*; InTech, 2011; p 748.

[22] Welton, T. *Coord. Chem. Rev.* **2004**, *248*, 2459–2477.

[23] Ray, A. *J. Am. Chem. Soc.* **1969**, *91*, 6511–6512.

[24] Ward, A. J.; du Reau, C. In *Surface and Colloid Science*; Matijevic, E., Ed.; Surface and Colloid Science; Plenum Press, New York, 1993; Vol. 15; Chapter 4.

[25] Singh, H. N.; Saleem, S. M.; Singh, R. P.; Birdi, K. S. *J. Phys. Chem.* **1980**, *84*, 2191–2194.

[26] Seguin, C.; Eastoe, J.; Clapperton, R.; Heenan, R. K.; Grillo, I. *Colloids Surf., A* **2006**, *282–283*, 134–142.

[27] Hildebrand, J. *Solubility of Non-electrolytes*; ACS monograph; Reinhold Publishing Corporation, 1936.

[28] Gordon, J. E. *The organic chemistry of electrolyte solution*; Wiley, New York, 1975; pp 158–162.

[29] Evans, D. F. *Langmuir* **1988**, *4*, 3–12.

[30] Welton, T. *Chem. Rev.* **1999**, *99*, 2071–2083.

[31] Wasserscheid, P.; Keim, W. *Angew. Chem., Int. Ed.* **2000**, *39*, 3772–3789.

[32] Huddleston, J. G.; Visser, A. E.; Reichert, W. M.; Willauer, H. D.; Broker, G. A.; Rogers, R. D. *Green Chem.* **2001**, *3*, 156–164.

[33] Evans, D.; Yamauchi, A.; Roman, R.; Casassa, E. Z. *J. Colloid Interface Sci.* **1982**, *88*, 89–96.

[34] Greaves, T. L.; Drummond, C. J. *Chem. Soc. Rev.* **2008**, *37*, 1709–1726.

[35] Hao, J. C.; Zemb, T. *Curr. Opin. Colloid Interface Sci.* **2007**, *12*, 129–137.

[36] Sharma, S. C.; Atkin, R.; Warr, G. G. *J. Phys. Chem. B* **2013**, *117*, 14568–14575.

[37] Chaudhary, G. R.; Bansal, S.; Mehta, S.; Ahluwalia, A. *J. Chem. Thermodyn.* **2012**, *50*, 63–70.

[38] Anderson, J. L.; Pino, V.; Hagberg, E. C.; Sheares, V. V.; Armstrong, D. W. *Chem. Commun.* **2003**, 2444–2445.

[39] Araos, M. U.; Warr, G. G. *Langmuir* **2008**, *24*, 9354–9360.

[40] Fletcher, K. A.; Pandey, S. *Langmuir* **2003**, *20*, 33–36.

[41] Patrascu, C.; Gauffre, F.; Nallet, F.; Bordes, R.; Oberdisse, J.; de Lauth-Viguerie, N.; Mingotaud, C. *ChemPhysChem* **2006**, *7*, 99–101.

[42] Inoue, T.; Yamakawa, H. *J. Colloid Interface Sci.* **2011**, *356*, 798–802.

[43] Atkin, R.; Bobillier, S. M. C.; Warr, G. G. *J. Phys. Chem. B* **2010**, *114*, 1350–1360.

[44] Kimizuka, N.; Nakashima, T. *Langmuir* **2001**, *17*, 6759–6761.

[45] López-Barrón, C. R.; Li, D.; DeRita, L.; Basavaraj, M. G.; Wagner, N. J. *J. Am. Chem. Soc.* **2012**, *134*, 20728–20732, PMID: 23030359.

[46] Rao, K. S.; So, S.; Kumar, A. *Chem. Commun.* **2013**, *49*, 8111–8113.

[47] Li, J.; Zhang, J.; Zhao, Y.; Han, B.; Yang, G. *Chem. Commun.* **2012**, *48*, 994–996.

[48] Li, J.; Zhang, J.; Han, B.; Zhao, Y.; Yang, G. *J. Colloid Interface Sci.* **2012**, *368*, 395–399.

[49] Zech, O.; Thomaier, S.; Kolodziejski, A.; Touraud, D.; Grillo, I.; Kunz, W. *J. Colloid Interface Sci.* **2010**, *347*, 227–232.

[50] Eastoe, J.; Gold, S.; Rogers, S. E.; Paul, A.; Welton, T.; Heenan, R. K.; Grillo, I. *J. Am. Chem. Soc.* **2005**, *127*, 7302–7303.

[51] Li, N.; Zhang, S. H.; Zheng, L. Q.; Gao, Y.; Yu, L. *Langmuir* **2008**, *24*, 2973–2976.

[52] Mehta, S. K.; Kaur, K. *Anal. Chem. Indian Journal of Chemistry, Section A: Inorganic, Bio-inorganic, Physical, Theoretical & Analytical Chemistry* **2010**, *49*, 662–684.

[53] Zech, O.; Kunz, W. *Soft Matter* **2011**, *7*, 5507–5513.

[54] Liu, L.; Bauduin, P.; Zemb, T.; Eastoe, J.; Hao, J. *Langmuir* **2009**, *25*, 2055–2059.

[55] Rojas, O.; Koetz, J. *J. Surface Sci. Technol.* **2010**, *26*, 173–196.

[56] Gao, Y.; Hilfert, L.; Voigt, A.; Sundmachert, K. *J. Phys. Chem. B* **2008**, *112*, 3711–3719.

[57] Atkin, R.; Warr, G. G. *J. Phys. Chem. B* **2007**, *111*, 9309–9316.

[58] Seth, D.; Chakraborty, A.; Setua, P.; Sarkar, N. *Langmuir* **2006**, *22*, 7768–7775.

[59] Gao, Y.; Li, N.; Zheng, L. Q.; Zhao, X. Y.; Zhang, S. H.; Han, B. X.; Hou, W. G.; Li, G. Z. *Green Chem.* **2006**, *8*, 43–49.

[60] Behera, K.; Kumar, V.; Pandey, S. *ChemPhysChem* **2010**, *11*, 1044–1052.

[61] Gao, H.; Li, J.; Han, B.; Chen, W.; Zhang, J.; Zhang, R.; Yan, D. *Phys. Chem. Chem. Phys.* **2004**, *6*, 2914–2916.

[62] Kahlweit, M.; Strey, R. *Angew. Chem., Int. Ed.* **1985**, *24*, 654–668.

[63] Zech, O.; Thomaier, S.; Bauduin, P.; Ruck, T.; Touraud, D.; Kunz, W. *J. Phys. Chem. B* **2009**, *113*, 465–473.

[64] Rabe, C.; Koetz, J. *Colloids Surf., A* **2010**, *354*, 261–267.

[65] Yoshida, Y.; Saito, G. *J. Mater. Chem.* **2006**, *16*, 1254–1262.

[66] Thomaier, S. Formulation and characterization of new innovative colloidal systems involving ionic liquids for the application at high temperatures. Ph.D. thesis, University of Regensburg, 2009.

[67] Sivia, D. *Elementary Scattering Theory*; Oxford University Press, 2011.

[68] Lindner, P., Zemb, T., Eds. *Neutrons, X-rays and Light: Scattering Methods Applied to Soft Condensed Matter*, 1st ed.; Elsevier Science B.V., 2002.

[69] Keiderling, U. *Appl. Phys. A: Mater. Sci. Process.* **2002**, *74*, s1455–s1457.

[70] Kohlbrecher, J.; Bressler, I. http://kur.web.psi.ch/sans1/SANSSoft/sasfit.html.

[71] Richard, D.; Ferrand, M.; Kearley, G. J. *J. Neutron Res.* **1996**, *4*, 33–39.

[72] Zhang, F.; Ilavsky, J.; Long, G. G.; Quintana, J. P. G.; Allen, A. J.; Jemian, P. R. *Metall. Mater. Trans. A* **2010**, *41*, 1151–1158.

[73] Muthig, M.; Prevost, S.; Orglmeister, R.; Gradzielski, M. *J. Appl. Crystallogr.* **2013**, *46*, 1187–1195.

[74] Heintz, A.; Lehmann, J. K.; Kozlova, S. A.; Balantseva, E. V.; Bazyleva, A. B.; Ondo, D. *Fluid Phase Equilib.* **2010**, *294*, 187–196, Ionic Liquids Special Issue.

[75] Łuczak, J.; Jungnickel, C.; Joskowska, M.; Thöming, J.; Hupka, J. *J. Colloid Interface Sci.* **2009**, *336*, 111–116.

[76] Galgano, P. D.; Seoud, O. A. E. *J. Colloid Interface Sci.* **2011**, *361*, 186–194.

[77] Laughlin, R. G. *The Acqueous Phase Behaviour of Surfactants*; Colloid Science; Academic Press Inc., 1996.

[78] Greaves, T. L.; Weerawardena, A.; Fong, C.; Drummond, C. J. *Langmuir* **2007**, *23*, 402–404.

[79] Dirand, M.; Bouroukba, M.; Briard, A.-J.; Chevallier, V.; Petitjean, D.; Corriou, J.-P. *J. Chem. Thermodyn.* **2002**, *34*, 1255–1277.

[80] Mosselman, C.; Mourik, J.; Dekker, H. *J. Chem. Thermodyn.* **1974**, *6*, 477–487.

[81] Li, L.; Groenewold, J.; Picken, S. J. *Chem. Mater.* **2005**, *17*, 250–257.

[82] Hayashi, S.; Saha, S.; Hamaguchi, H. O. *IEEE T. Magn.* **2006**, *42*, 12–14.

[83] Meissner, H. P.; Michaels, A. S. *Ind. Eng. Chem. Res.* **1949**, *41*, 2782–2787.

[84] Szyszkowski, B. *Z. physik. Chemie* **1908**, *64*, 385.

[85] Harned, H. S.; Owen, B. B. *The physical chemistry of electrolytic solutions*, 3rd ed.; Reinhold Publishing corporation, New York, 1958; Chapter 14, p 603.

[86] Seoud, O. A. E.; Pires, P. A. R.; Abdel-Moghny, T.; Bastos, E. L. *J. Colloid Interface Sci.* **2007**, *313*, 296–304.

[87] Thomaier, S.; Kunz, W. *J. Mol. Liq.* **2007**, *130*, 104–107.

[88] Ashcroft, N. W.; Lekner, J. *Phys. Rev.* **1966**, *145*, 83–90.

[89] Bowlas, C. J.; Bruce, D. W.; Seddon, K. R. *Chem. Commun.* **1996**, 1625–1626.

[90] Bradley, A. E.; Hardacre, C.; Holbrey, J. D.; Johnston, S.; McMath, S. E. J.; Nieuwenhuyzen, M. *Chem. Mater.* **2002**, *14*, 629–635.

[91] Li, C.; He, J.; Chen, J.; Liu, J.; Zhang, Q.; Yu, Z. *J. Colloid Interface Sci.* **2011**, *359*, 474–480.

[92] Watson, L. In *Encyclopedia of Surface and Colloid Science*, 2nd ed.; Hubbart, A. T., Somasundaran, P., Eds.; Encyclopedia of Surface and Colloid Science; Taylor & Francis, 2006; Vol. 2; pp 1014 – 1025.

[93] Vaghela, N. M.; Sastry, N. V.; Aswal, V. K. *Colloids Surf., A* **2011**, *373*, 101 – 109.

[94] Sastry, N. V.; Vaghela, N. M.; Macwan, P. M.; Soni, S. S.; Aswal, V. K.; Gibaud, A. *J. Colloid Interface Sci.* **2012**, *371*, 52 – 61.

[95] Gómez-Díaz, D.; Navaza, J. M.; Sanjurjo, B. *J. Chem. Eng. Data* **2007**, *52*, 889–891.

[96] Wu, F.-G.; Wang, N.-N.; Zhang, Q.-G.; Sun, S.-F.; Yu, Z.-W. *J. Colloid Interface Sci.* **2012**, *374*, 197–205.

[97] Laughlin, R. G. In *Cationic Surfactants: Physical Chemistry*, 2nd ed.; Rubingh, D., Holland, P., Eds.; Surfactant Science; Taylor & Francis, 1990; Vol. 37; pp 1–40.

[98] Rosen, M. J. *Surfactants and Interfacial Phenomena*, 3rd ed.; John Wiley & Sons, Inc., 2004; Chapter 3, pp 105–177.

[99] Pedersen, J. S.; Gerstenberg, M. C. *Colloids Surf., A* **2003**, *213*, 175–187.

[100] Yang, L.; Alexandridis, P.; Steytler, D. C.; Kositza, M. J.; Holzwarth, J. F. *Langmuir* **2000**, *16*, 8555–8561.

[101] Huibers, P. D. T.; Shah, D. O. *Langmuir* **1997**, *13*, 5762–5765.

[102] Gradzielski, M. *Langmuir* **1998**, *14*, 6037–6044.

[103] Penders, M. H. G. M.; Strey, R. *J. Phys. Chem.* **1995**, *99*, 10313–10318.

[104] Gradzielski, M. *Curr. Opin. Colloid Interface Sci.* **2008**, *13*, 263–269.

[105] Teubner, M.; Strey, R. *J. Chem. Phys.* **1987**, *87*, 3195–3200.

[106] Gradzielski, M.; Langevin, D.; Sottmann, T.; Strey, R. *J. Chem. Phys.* **1996**, *104*, 3782–3787.

[107] Gompper, G.; Endo, H.; Mihailescu, M.; Allgaier, J.; Monkenbusch, M.; Richter, D.; Jakobs, B.; Sottmann, T.; Strey, R. *Europhys. Lett.* **2001**, *56*, 683–689.

[108] Schubert, K. V.; Strey, R.; Kline, S. R.; Kaler, E. W. *J. Chem. Phys.* **1994**, *101*, 5343–5355.

[109] Jouffroy, J.; Levinson, P.; de Gennes, P. G. *J. Physique* **1982**, *43*, 1241–1248.

[110] Sottmann, T.; Strey, R.; Chen, S. H. *J. Chem. Phys.* **1997**, *106*, 6483–6491.

[111] Chen, S.-H.; Lee, D.; Chang, S.-L. *J. Mol. Struct.* **1993**, *296*, 259–264.

[112] Chen, S.-H.; Choi, S.-M. *J. Appl. Crystallogr.* **1997**, *30*, 755–760.

[113] Choi, S.; Chen, S.; Sottmann, T.; Strey, R. *Physica A* **2002**, *304*, 85–92, Scattering Studies of Mesoscopic Scale Structure and Dynamics in Soft Matter.

[114] Chen, S.-H.; Choi, S.-M. *Physica A* **1997**, *236*, 38–51, Proceedings of the Workshop on Current Problems in Complex Fluids.

[115] Kotlarchyk, M. *Physica B & C* **1986**, *136*, 274–280.

[116] Auvray, L.; Cotton, J. P.; Ober, R.; Taupin, C. *J. Phys. Chem.* **1984**, *88*, 4586–4589.

[117] Arleth, L.; Pedersen, J. S. *Phys. Rev. E: Stat., Nonlinear, Soft Matter Phys.* **2001**, *63*, 061406.

[118] Klostermann, M.; Foster, T.; Schweins, R.; Lindner, P.; Glatter, O.; Strey, R.; Sottmann, T. *Phys. Chem. Chem. Phys.* **2011**, *13*, 20289–20301.

[119] Balogh, J.; Olsson, U.; Pedersen, J. S. *J. Phys. Chem. B* **2007**, *111*, 682–689.

[120] Odenbach, S. *J. Phys.: Condens. Matter* **2004**, *16*, R1135–R1150.

[121] Kumar, M.; Gupta, R. In *Diamagnetic Susceptibility of Organic Compounds, Oils, Paraffins and Polyethylenes*; Gupta, R., Ed.; Landolt-Börnstein - Group II Molecules and Radicals; Springer Berlin Heidelberg, 2008; Vol. 27B; pp 1190–1190.

[122] Rikken, R. S. M.; Nolte, R. J. M.; Maan, J. C.; van Hest, J. C. M.; Wilson, D. A.; Christianen, P. C. M. *Soft Matter* **2014**, *10*, 1295–1308.

[123] Porcar, L.; Hamilton, W. A.; Butler, P. D.; Warr, G. G. *Phys. Rev. Lett.* **2004**, *93*, 198301.

[124] Léon, A.; Bonn, D.; Meunier, J.; Al-Kahwaji, A.; Kellay, H. *Phys. Rev. Lett.* **2001**, *86*, 938–941.

[125] Ortega, A.; Garciá de la Torre, J. *J. Chem. Phys.* **2003**, *119*, 9914–9919.

[126] Wohlfarth, C. In *Supplement to IV/18*; Lechner, M., Ed.; Landolt-Börnstein - Group IV Physical Chemistry; Springer Berlin Heidelberg, 2009; Vol. 25; pp 377–380.

[127] Sears, V. F. *Neutron News* **1992**, *3*, 26–37.

[128] Lagourette, B.; Peyrelasse, J.; Boned, C.; Clausse, M. *Nature* **1979**, *281*, 60–62.

A

Appendix — Binary Systems

A.1 SANS model fitting

A.1.1 Spherical model as used in section 3

$$I(q) = BG + \int LN(R, R_0, \sigma) \cdot P(R) \cdot S(R_{HS}, \phi_{HS})\,\mathrm{d}R \tag{A.1}$$

where BG is the background. The polydisperse form factor is given by a spherical model:

$$P(q, R) = \left[\frac{4}{3}\pi R^3 \Delta SLD\, 3\frac{\sin qR - qR\cos qR}{(qR)^3}\right]^2 \tag{A.2}$$

with ΔSLD as the scattering contrast between micelles and bulk phase and where R is expressed by the lognormal distribution:

$$LN(R, R_0, \sigma) = \frac{N}{\sigma R\sqrt{2\pi}} \exp(-\frac{\ln(R/R_0)^2}{2\sigma^2}) \tag{A.3}$$

The n^{th} moment $\langle R^n \rangle$ of the micelle radius can be calculated as

$$\langle R^n \rangle = R_0^n \exp \frac{1}{2}\sigma^2 n^2 \tag{A.4}$$

$S(q, R_{HS}, \phi_{HS})$ is given by the structure factor of a hard sphere[88] whereby its number density is equal to the form factor which is ensured by its radius and volume fraction defined as

$$R_{HS} = R + \Delta R \tag{A.5a}$$

$$\phi_{HS} = \phi_{micelle} \frac{(R + \Delta R)^3}{R^3} \tag{A.5b}$$

Scattering contrast and volume fraction were calculated from the sample composition whereby it was assumed that the micelles are partly swollen by solvent (given by the ratio x of the total MRTIL volume located in the micelles) and the surfactant is partly monomerically dissolved in the bulk phase (given by the ratio y of the total surfactant chains located in the micelles). The surfactant head groups are assumed to be counted to the bulk phase. This is quantified by the following set of equations:

$$x = \phi_{MRTIL,m}/\phi_{MRTIL} \tag{A.6a}$$

$$y = \phi_{C_n,b}/\phi_{C_n} \tag{A.6b}$$

$$w = \phi_{C_n}/\phi_{surfactant} \tag{A.6c}$$

$$\phi_{bulk} = \phi_{MRTIL}(1-x) + \phi_{surfactant}(1-w) + \phi_{surfactant} wy \tag{A.6d}$$

$$\phi_{micelle} = 1 - \phi_{bulk} \tag{A.6e}$$

$$\begin{aligned} SLD_{bulk} = [&sld_{MRTIL}\phi_{MRTIL}(1-x) + sld_{mimCl}\phi_{surfactant}(1-w) \\ &+ sld_{C_n}\phi_{surfactant} wy]/\phi_{bulk} \end{aligned} \tag{A.6f}$$

$$SLD_{micelle} = [sld_{MRTIL}\phi_{MRTIL}x + sld_{C_n}\phi_{surfactant} w(1-y)]/\phi_{micelle} \tag{A.6g}$$

$$\alpha = \frac{x\phi_{MRTIL}}{\phi_{micelle}} \tag{A.6h}$$

with sld_i as the scattering length density for the pure molecule (part) indicated by i (see table A.2). ϕ_{MRTIL}, $\phi_{surfactant}$ and ϕ_{C_n} are the total volume fractions of MRTIL, surfactant and the surfactant alkyl chain in a sample, respectively. $\phi_{MRTIL,m}$ is the total volume fraction of MRTIL located in micelles and $\phi_{C_n,b}$ is the total volume fraction of alkyl chains located in the bulk (continuous solvent). The volume fraction of ionic liquid in the micelle relative to the micelle volume is then given by α. Used densities are listed in table A.1. The average aggregation number N_{agg} of surfactant molecules per micelle is then

$$N_{agg} = \frac{4}{3}\pi \left\langle R^3 \right\rangle \frac{1}{v_{HC}}(1-\alpha) \tag{A.7}$$

The average headgroup spacing a_s is then given by

$$a_s = \frac{4\pi \left\langle R^2 \right\rangle}{N_{agg}} \tag{A.8}$$

Table A.1 Densities used for the SANS model fitting.

compound	$\frac{density}{g\,cm^{-3}}$
C_2mimFeCl$_4$	1.440
C_4mimFeCl$_4$	1.360
C_{14}mimCl	0.970
C_{16}mimCl	0.960
C_{18}mimCl	0.952
C_{14}	0.809
C_{16}	0.812
C_{18}	0.820
mimCl	1.452

Fig. A.2 shows the measured SANS curves including the fits and table A.2 gives the underlying fit parameters. The calculated aggregation numbers, surfactant headgroup spacings and solvent ratio in the micelles show a coherent picture of the surfactant concentration dependent aggregation be-

haviour (see Fig. 3.7 and A.1): At very low concentrations the aggregates contain only a few surfactant molecules swollen by a great amount of solvent leading to more loosely packed micelles with high headgroup spacings. With increasing surfactant concentration the aggregation number increases which favors more compact micelles with less solvent inside and smaller surfactant headgroups. Finally at high surfactant concentrations (near the phase boundary) α approaches zero and a_s reaches values comparable to the results from surface tension measurements (see table A.5) and values known from water systems.

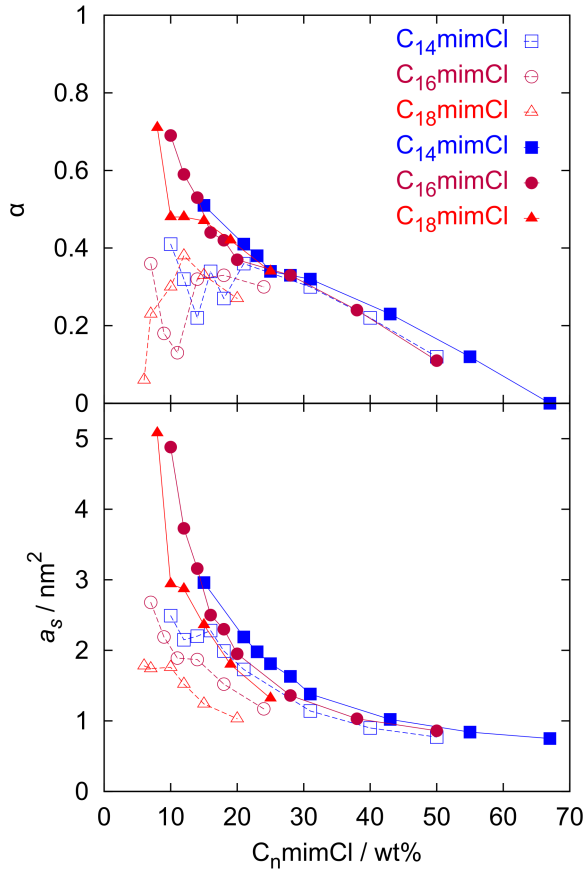

Figure A.1 Volume ratio of MRTIL in micelles (α) and headgroup area (a_s) as derived from SANS data described in section A.1.1 for systems with C_2mimFeCl$_4$ (open symbols) and C_4mimFeCl$_4$ (filled symbols) as solvent.

Table A.2 Input parameters and fit results for the model described in section A.1.1 for all SANS samples.

C_2mim$FeCl_4$	$C_j$mimCl	given by sample composition				$\frac{sld_i}{10^{-4}\mathrm{nm}^{-2}}$ given by literature			fit parameter						calculated	
		$\frac{\phi_{m,surf}}{\mathrm{wt\%}}$	ϕ_{IL}	$\phi_{surf.}$	w	$i = MRTIL$	$i = \mathrm{C}_n$	$i = \mathrm{mimCl}$	x	y	σ	$\frac{R_0}{\mathrm{nm}}$	$\frac{\Delta R}{\mathrm{nm}}$	$\frac{BG}{\mathrm{cm}^{-1}}$	α	$\frac{a_s}{\mathrm{nm}^2}$
2	14	50	0.40	0.60	0.751	1.64	-0.38	2.41	0.18	0.11	0.159	1.675	0.174	0.610	0.12	0.77
2	14	40	0.50	0.50	0.751	1.64	-0.38	2.41	0.29	0.00	0.201	1.566	0.047	0.546	0.22	0.90
2	14	31	0.60	0.40	0.751	1.64	-0.38	2.41	0.28	0.00	0.256	1.286	0.024	0.503	0.30	1.14
2	14	21	0.72	0.28	0.751	1.64	-0.38	2.41	0.20	0.10	0.323	0.845	0.000	0.460	0.36	1.73
2	14	18	0.75	0.25	0.751	1.64	-0.38	2.41	0.09	0.23	0.333	0.634	0.006	0.451	0.27	1.99
2	14	16	0.77	0.23	0.751	1.64	-0.38	2.41	0.11	0.24	0.345	0.598	0.002	0.442	0.34	2.28
2	14	14	0.80	0.20	0.751	1.64	-0.38	2.41	0.04	0.50	0.286	0.576	0.000	0.430	0.22	2.20
2	14	12	0.83	0.17	0.751	1.64	-0.38	2.41	0.04	0.62	0.135	0.800	0.000	0.423	0.32	2.15
2	14	10	0.86	0.14	0.751	1.64	-0.38	2.41	0.04	0.64	0.063	0.825	0.000	0.411	0.41	2.49
2	16	24	0.68	0.32	0.774	1.64	-0.37	2.41	0.20	0.00	0.254	1.442	0.039	0.478	0.30	1.17
2	16	18	0.76	0.24	0.774	1.64	-0.37	2.41	0.15	0.09	0.306	1.076	0.001	0.442	0.33	1.52
2	16	14	0.81	0.19	0.774	1.64	-0.37	2.41	0.08	0.27	0.332	0.828	0.003	0.422	0.32	1.87
2	16	11	0.84	0.16	0.774	1.64	-0.37	2.41	0.01	0.53	0.296	0.674	0.000	0.419	0.13	2.19
2	16	9	0.87	0.13	0.774	1.64	-0.37	2.41	0.01	0.63	0.318	0.595	0.021	0.398	0.18	2.68
2	16	7	0.90	0.10	0.774	1.64	-0.37	2.41	0.03	0.59	0.178	0.739	0.003	0.393	0.36	1.89
2	18	20	0.72	0.28	0.792	1.64	-0.37	2.41	0.14	0.01	0.223	1.810	0.125	0.465	0.27	1.03
2	18	15	0.79	0.21	0.792	1.64	-0.37	2.41	0.14	0.00	0.261	1.575	0.057	0.440	0.33	1.24
2	18	12	0.83	0.17	0.792	1.64	-0.37	2.41	0.12	0.02	0.313	1.285	0.000	0.417	0.38	1.52
2	18	10	0.86	0.14	0.792	1.64	-0.37	2.41	0.05	0.33	0.348	0.927	0.005	0.408	0.30	1.74
2	18	7	0.89	0.11	0.792	1.64	-0.37	2.41	0.01	0.60	0.287	0.931	0.000	0.393	0.23	1.78
2	18	6	0.92	0.08	0.792	1.64	-0.37	2.41	0.00	0.81	0.184	0.848	0.091	0.383	0.06	1.76

(Continues on next page.)

(Continued from previous page.)

$C_i$mim$FeCl_4$ $C_j$mimCl		given by sample composition				$\frac{sld_i}{10^{-4}\mathrm{nm}^{-2}}$ given by literature			fit parameter						calculated	
		$\frac{\phi_{m,surf}}{\mathrm{wt\%}}$	ϕ_{IL}	$\phi_{surf.}$	w	$i = MRTIL$	$i = \mathrm{C}_n$	$i = \mathrm{mimCl}$	x	y	σ	$\frac{R_0}{\mathrm{nm}}$	$\frac{\Delta R}{\mathrm{nm}}$	$\frac{BG}{\mathrm{cm}^{-1}}$	α	$\frac{a_s}{\mathrm{nm}^2}$
4	14	67	0.26	0.74	0.751	1.55	-0.38	2.41	0.00	0.22	0.130	1.581	0.262	0.683	0.00	0.75
4	14	55	0.37	0.63	0.751	1.55	-0.38	2.41	0.21	0.08	0.153	1.570	0.122	0.639	0.12	0.84
4	14	43	0.49	0.51	0.751	1.55	-0.38	2.41	0.31	0.00	0.200	1.411	0.097	0.597	0.23	1.02
4	14	31	0.61	0.39	0.751	1.55	-0.38	2.41	0.30	0.01	0.257	1.112	0.116	0.559	0.32	1.38
4	14	28	0.65	0.35	0.751	1.55	-0.38	2.41	0.27	0.01	0.288	0.915	0.088	0.555	0.33	1.63
4	14	25	0.68	0.32	0.751	1.55	-0.38	2.41	0.24	0.00	0.309	0.809	0.110	0.543	0.34	1.81
4	14	23	0.70	0.30	0.751	1.55	-0.38	2.41	0.25	0.00	0.312	0.781	0.110	0.530	0.38	1.98
4	14	21	0.73	0.27	0.751	1.55	-0.38	2.41	0.25	0.03	0.307	0.758	0.127	0.524	0.41	2.19
4	14	15	0.80	0.20	0.751	1.55	-0.38	2.41	0.27	0.00	0.321	0.658	0.200	0.498	0.51	2.96
4	16	50	0.42	0.58	0.774	1.55	-0.37	2.41	0.16	0.12	0.154	1.701	0.187	0.629	0.11	0.86
4	16	38	0.53	0.47	0.774	1.55	-0.37	2.41	0.27	0.00	0.189	1.597	0.085	0.588	0.24	1.03
4	16	28	0.64	0.36	0.774	1.55	-0.37	2.41	0.28	0.00	0.245	1.297	0.071	0.569	0.33	1.36
4	16	20	0.74	0.26	0.774	1.55	-0.37	2.41	0.16	0.21	0.279	0.929	0.155	0.519	0.37	1.95
4	16	18	0.76	0.24	0.774	1.55	-0.37	2.41	0.23	0.00	0.316	0.809	0.049	0.516	0.42	2.30
4	16	16	0.78	0.22	0.774	1.55	-0.37	2.41	0.14	0.33	0.267	0.817	0.174	0.510	0.44	2.50
4	16	14	0.81	0.19	0.774	1.55	-0.37	2.41	0.17	0.34	0.297	0.741	0.256	0.486	0.53	3.16
4	16	12	0.84	0.16	0.774	1.55	-0.37	2.41	0.20	0.31	0.309	0.715	0.294	0.480	0.59	3.73
4	16	10	0.86	0.14	0.774	1.55	-0.37	2.41	0.29	0.20	0.310	0.726	0.294	0.477	0.69	4.88
4	18	25	0.67	0.33	0.792	1.55	-0.37	2.41	0.25	0.00	0.230	1.542	0.079	0.538	0.34	1.32
4	18	19	0.75	0.25	0.792	1.55	-0.37	2.41	0.24	0.00	0.282	1.205	0.013	0.517	0.42	1.80
4	18	15	0.80	0.20	0.792	1.55	-0.37	2.41	0.20	0.09	0.290	1.000	0.000	0.496	0.47	2.36
4	18	12	0.84	0.16	0.792	1.55	-0.37	2.41	0.15	0.18	0.283	0.841	0.003	0.492	0.48	2.94
4	18	10	0.86	0.14	0.792	1.55	-0.37	2.41	0.07	0.55	0.201	0.903	0.149	0.476	0.48	5.08
4	18	8	0.89	0.11	0.792	1.55	-0.37	2.41	0.16	0.51	0.124	1.018	0.082	0.469	0.71	2.87

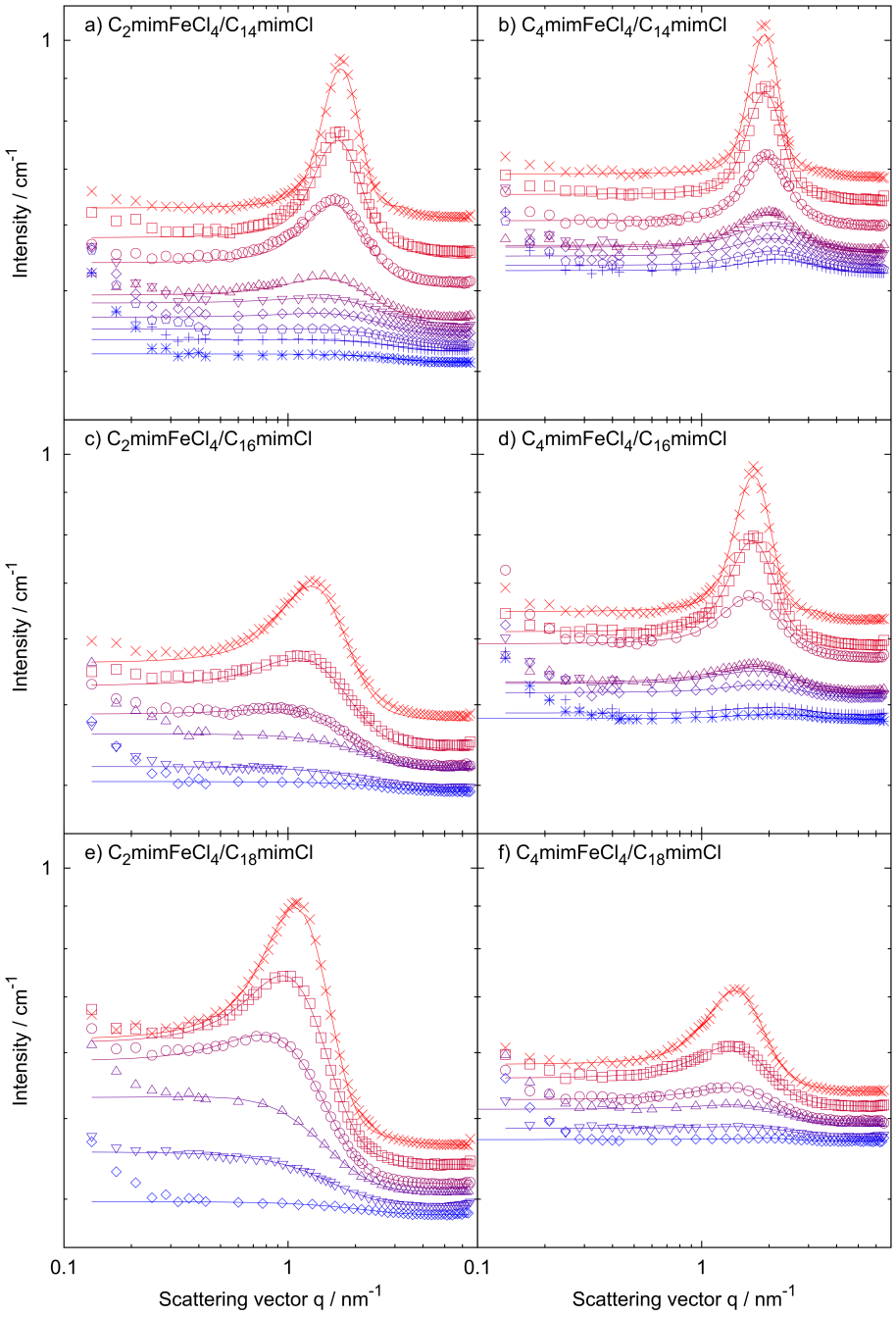

Figure A.2 SANS curves measured (symbols, ascending order from blue to red) and fitted with the model described in section A.1.1 (lines) for all six systems.

A.1.2 Alternative spherical model

Alternatively the model described in section A.1.1 was used with ΔSLD and volume fractions calculated as described in section A.2. With that eq. A.7 simplifies to

$$N_{agg} = \frac{4}{3}\pi \left\langle R^3 \right\rangle \frac{1}{v_{HC}} \tag{A.9}$$

Resulting fit curves and extracted aggregation numbers are plotted in Fig. A.4 and A.3, respectively.

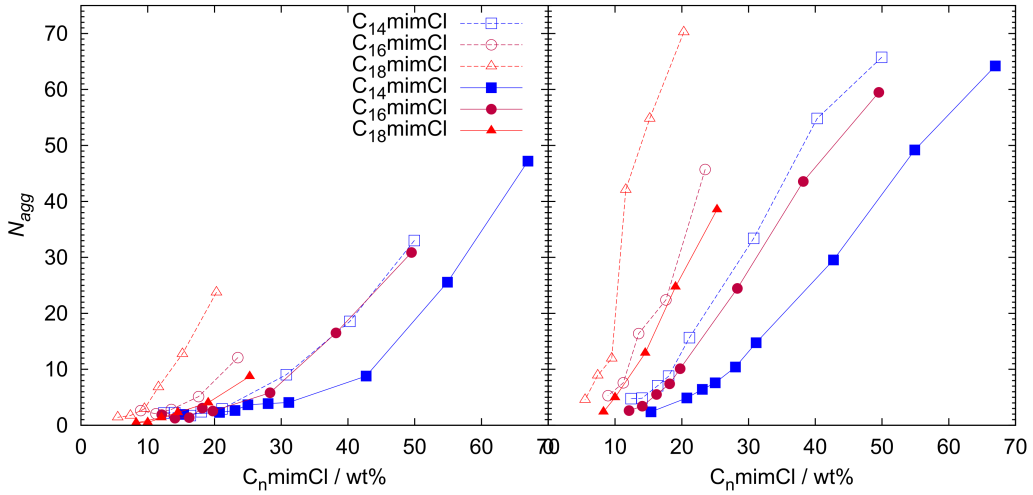

Figure A.3 Aggregation numbers calculated from SANS model fitting described in section A.1.2 (left) and A.1.3 (right) and listed in table A.3 for surfactant mixed with C_2mimFeCl$_4$ (open symbols) and C_4mimFeCl$_4$ (filled symbols).

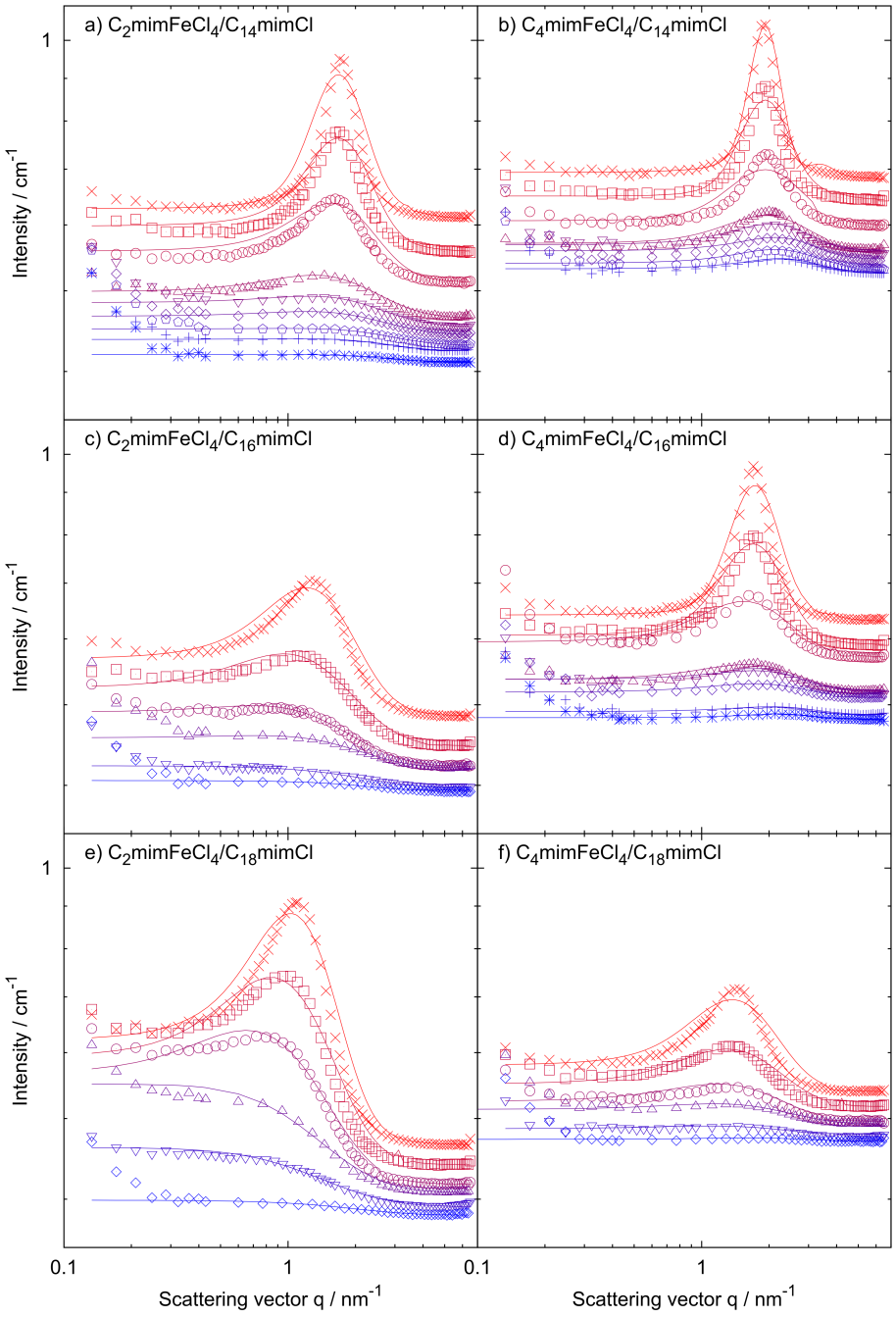

Figure A.4 SANS curves measured (symbols, ascending order from blue to red) and fitted with the model described in section A.1.2 (lines) for all six systems.

Table A.3 Scattering invariant as calculated with eq. 3.2 and 3.3a. The aggregation numbers are as derived for the three different SANS models described in section A.1.1 (I), A.1.2 (II) and A.1.3 (III). Plots are found in Fig. A.3 and 3.7.

C_xmimCl	$C_2mimFeCl_4$						$C_4mimFeCl_4$					
	$\frac{\phi_{m,surf}}{\text{wt\%}}$	$\frac{Q_{inv}^{ex}}{10^{-7}\text{nm}^{-4}}$	$\frac{Q_{inv}^{th}}{10^{-7}\text{nm}^{-4}}$	N_{agg}(I)	N_{agg}(II)	N_{agg}(III)	$\frac{\phi_{m,surf}}{\text{wt\%}}$	$\frac{Q_{inv}^{ex}}{10^{-7}\text{nm}^{-4}}$	$\frac{Q_{inv}^{th}}{10^{-7}\text{nm}^{-4}}$	N_{agg}(I)	N_{agg}(II)	N_{agg}(III)
14	50	1.51	2.02	48.0	33.0	65.7	67	1.44	2.16	43.6	47.2	64.2
14	40	1.35	1.72	36.9	18.6	54.8	55	1.43	1.86	38.7	25.6	49.2
14	31	1.23	1.33	20.7	9.0	33.4	43	1.42	1.47	26.5	8.8	29.5
14	21	0.80	0.83	6.4	2.9	15.7	31	1.10	1.01	12.8	4.1	14.7
14	18	0.56	0.64	3.2	2.4	8.8	28	0.80	0.86	7.6	3.9	10.4
14	16	0.50	0.54	2.5	1.7	7.1	25	0.75	0.71	5.5	3.7	7.6
14	14	0.35	0.38	2.2	2.3	4.8	23	0.55	0.61	4.7	2.6	6.4
14	12	0.29	0.26	3.9	2.2	4.8	21	0.47	0.48	4.0	2.3	4.9
14	10	0.20	0.08	3.5	–	–	15	0.16	0.16	2.3	1.9	2.4
16	24	1.02	1.16	25.5	12.1	45.7	50	1.39	1.83	44.4	30.9	59.5
16	18	0.84	0.81	11.5	5.1	22.4	38	1.29	1.48	33.4	16.5	43.6
16	14	0.52	0.54	5.8	2.8	16.4	28	1.08	1.08	17.5	5.8	24.4
16	11	0.41	0.38	3.6	2.1	7.6	20	0.67	0.64	6.5	2.5	10.1
16	9	0.26	0.20	2.5	2.6	5.3	18	0.62	0.55	4.4	3.1	7.4
16	7	0.13	0.06	2.7	–	–	16	0.40	0.44	3.9	1.4	5.5
16	–	–	–	–	–	–	14	0.31	0.30	2.6	1.3	3.4
16	–	–	–	–	–	–	12	0.18	0.17	2.1	1.9	2.6
16	–	–	–	–	–	–	10	0.15	0.03	1.6	–	–
18	20	1.04	1.17	44.1	23.7	70.2	25	0.93	1.15	25.1	8.7	38.5
18	15	0.84	0.87	28.8	12.8	54.8	19	0.71	0.84	11.9	4.0	24.7
18	12	0.58	0.62	16.6	6.8	42.1	15	0.52	0.57	6.3	2.3	12.9
18	10	0.46	0.46	7.8	2.9	12.0	10	0.26	0.28	3.8	0.5	5.0
18	7	0.36	0.29	7.4	1.7	8.9	8	0.16	0.15	2.6	0.4	2.4
18	6	0.21	0.13	5.4	1.4	4.6	12	0.42	0.42	3.6	1.4	–

A.1.3 Ellipsoidal model

$$I(q) = BG + P(R, \nu) \cdot S(R_{HS}, \phi_{HS})\,\mathrm{d}R \tag{A.10}$$

The form factor was chosen to be monodisperse to avoid overfitting and is given by an ellipsoidal model characterized by two equal semi-axis R and a semi-principal axes νR.

$$P(q, R, \nu) = \int_0^{\pi/2} K^2(q, x) \sin\Theta \mathrm{d}\Theta \tag{A.11a}$$

$$x = R\sqrt{\nu^2 \cos^2\Theta + \sin^2\Theta} \tag{A.11b}$$

$$K(q, R, \nu) = \frac{4}{3}\pi\nu R^3 \Delta SLD 3 \frac{\sin qx - qx\cos qx}{(qx)^3} \tag{A.11c}$$

ΔSLD and volume fractions were calculated as described in section A.2. The hard sphere radius is given by eq. A.12a and defines the hard sphere volume fraction via eq. A.12b.

$$R_{HS} = \sqrt[3]{\nu}(R + \Delta R) \tag{A.12a}$$

$$\phi_{HS} = \phi_{micelle} \frac{\nu (R_{HS})^3}{R^3} \tag{A.12b}$$

With that the aggregation number can be calculated as

$$N_{agg} = \frac{4}{3}\pi\nu R^3 \frac{1}{v_{HC}} \tag{A.13}$$

Extracted aggregation numbers are plotted in Fig. A.3. The general trend of the aggregation number found for the other methods/models can be reproduced.

A.2 Scattering invariant

The scattering length densities needed to calculate the theoretical invariant described in chapter 3 were derived as followed:

$$sld_{surf} = w \cdot sld_{C_n} + (1 - w) \cdot sld_{mimCl} \tag{A.14a}$$

$$SLD_{bulk} = \frac{sld_{MRTIL}\frac{m_{IL}}{\rho_{IL}} + sld_{surf}\frac{m_{surf,b}}{\rho_{surf}} + sld_{mimCl}\frac{m_{surf}-m_{surf,b}}{a\cdot\rho_{mimCl}}}{V_{tot}\phi_{bulk}} \tag{A.14b}$$

$$\Delta SLD = SLD_{bulk} - sld_{C_n} \tag{A.14c}$$

A.3 Density

As shown in Fig. A.5 (left) the density of C_4mimFeCl$_4$ and a mixture of C_4mimFeCl$_4$/C_{14}mimCl show a linear dependency on temperature. Linear regression gives an equation to correct density values from literature given for room temperature as surface tension measurements were done at 45 °C. The linearity of the reciprocal density of C_4mimFeCl$_4$/C_{14}mimCl mixtures shown in Fig. A.5 (right) validates the simple ideal mixing approximation used to calculate the density of the mixtures.

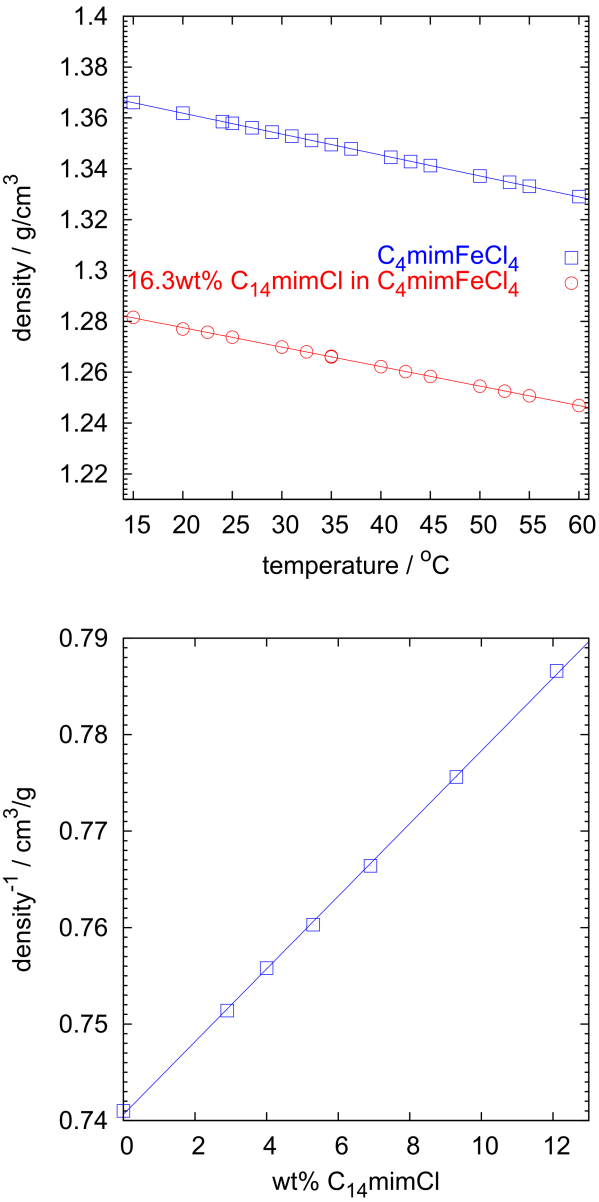

Figure A.5 left: Density (d) as a function of temperature measured with Anton Paar density-meter DMA4500 for pure C_4mimFeCl$_4$ (blue squares, linear regression gives: $d = [(-8.23 \pm 0.012)\, 10^{-4}\,°C^{-1} \cdot x + (1.37833 \pm 0.000048)]\, g/cm^3$) and 16.3 wt% C_{14}mimCl in C_4mimFeCl$_4$ (red circles, linear regression gives: $d = [(-7.66 \pm 0.034)\, 10^{-4}\,°C^{-1} \cdot x + (1.29287 \pm 0.00013)]\, g/cm^3$). **right:** Density at 35 °C as a function of surfactant concentration with Anton Paar density-meter for a binary solution of C_4mimFeCl$_4$/C_{14}mimCl. (linear regression gives: $1/d = [(3.769 \pm 0.031)\, 10^{-3} \cdot x + (0.74063 \pm 0.00021)]\, cm^3/g$)

A.4 Differential scanning calorimetry (DSC)

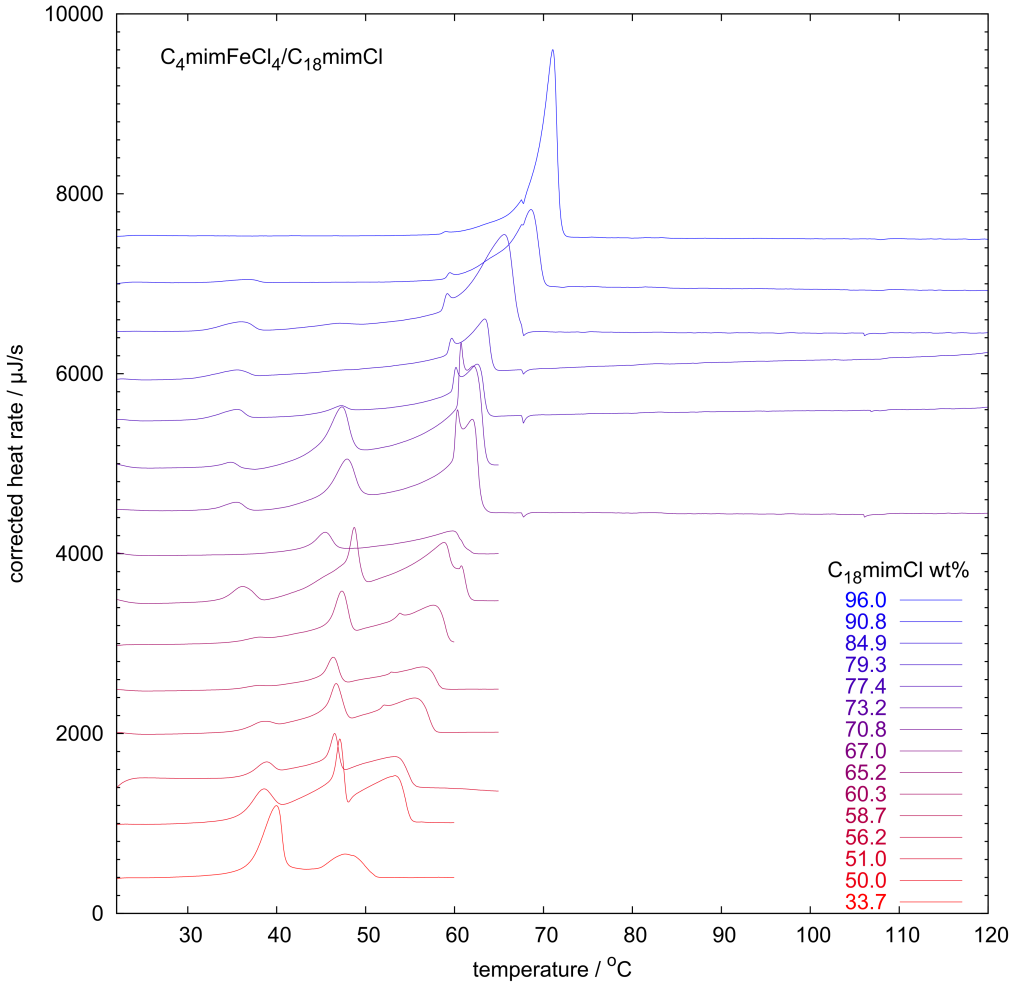

Figure A.6 DSC curves (background subtracted) for the system C_{18}mimCl/C_4mimFeCl$_4$. Increasing surfactant ratio is in ascending order. Curves are shifted relative to each other to enhance clarity.

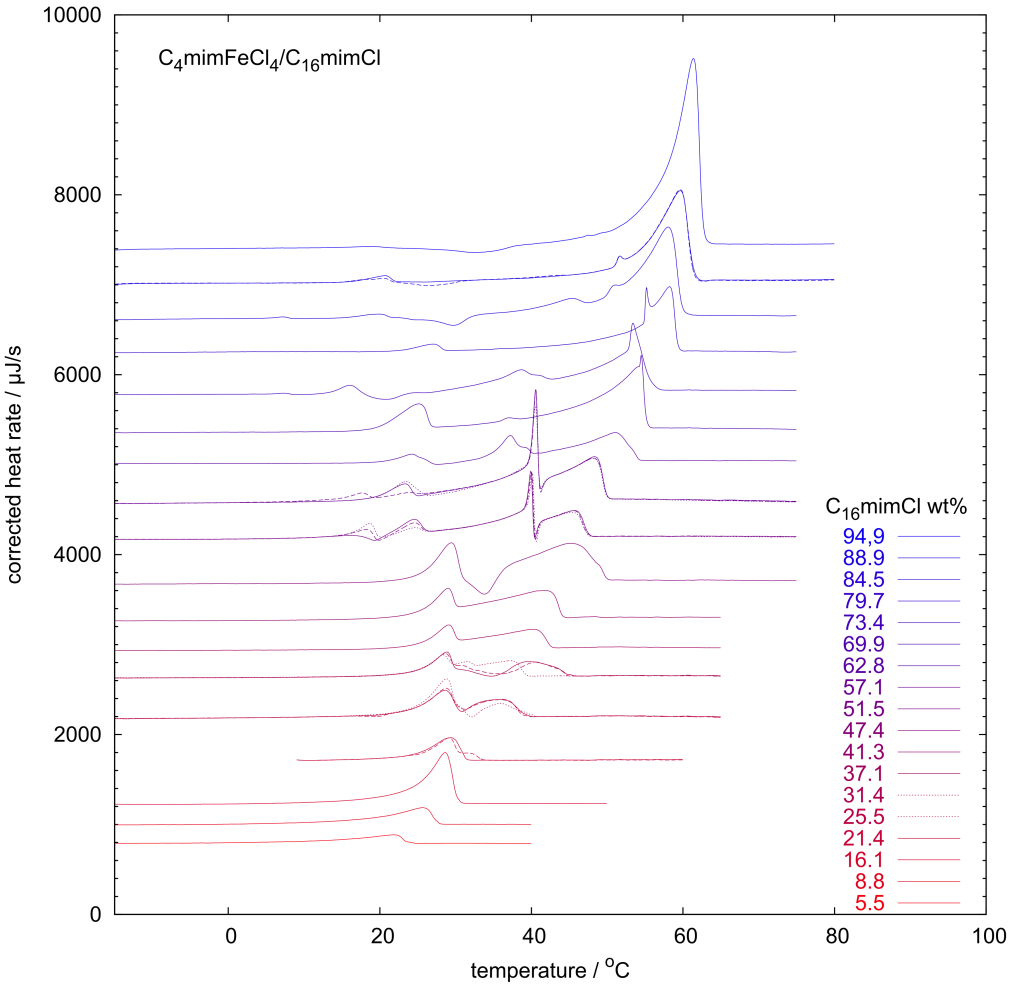

Figure A.7 DSC curves (background subtracted) for the system C_{16}mimCl/C_4mimFeCl$_4$. Increasing surfactant ratio is in ascending order. Curves are shifted relative to each other to enhance clarity. In case of samples with a low reproducibility several curves are plotted in the chronological order straight→broken→dotted line.

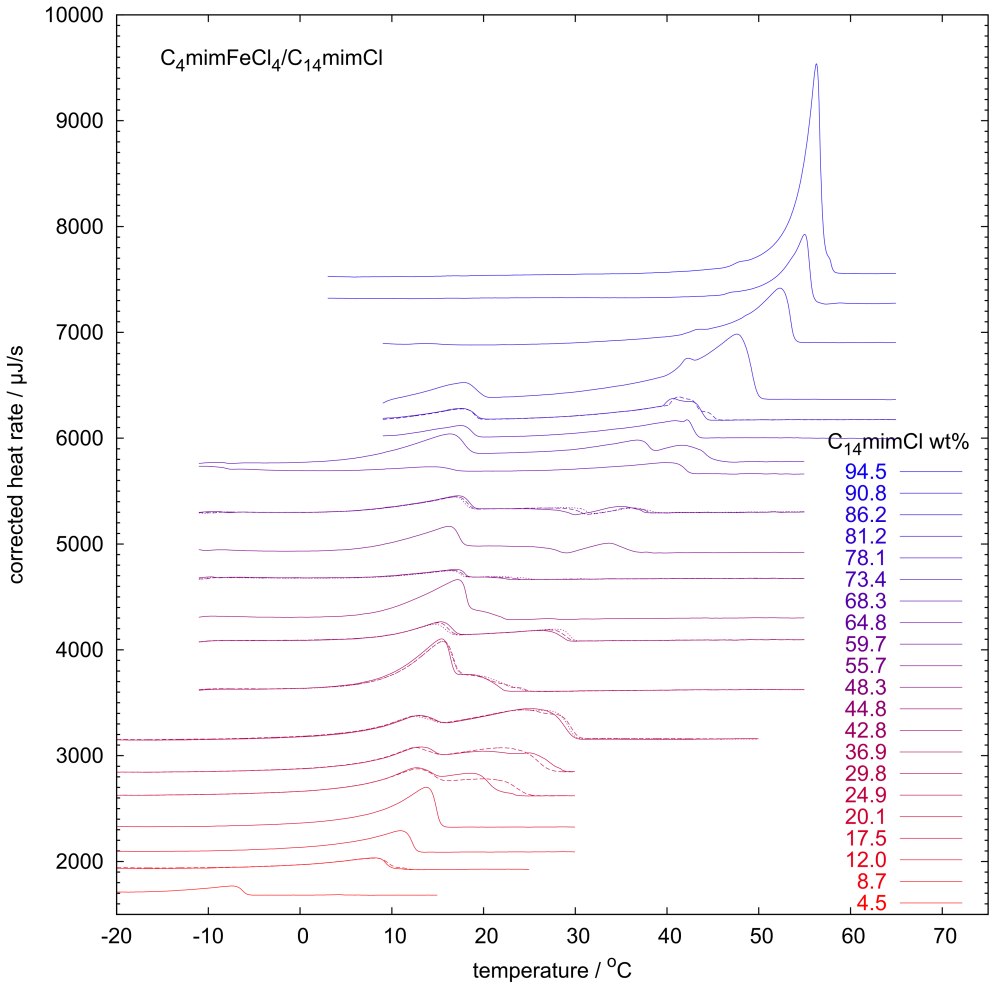

Figure A.8 DSC curves (background subtracted) for the system C_{14}mimCl/C_4mimFeCl$_4$. Increasing surfactant ratio is in ascending order. Curves are shifted relative to each other to enhance clarity.

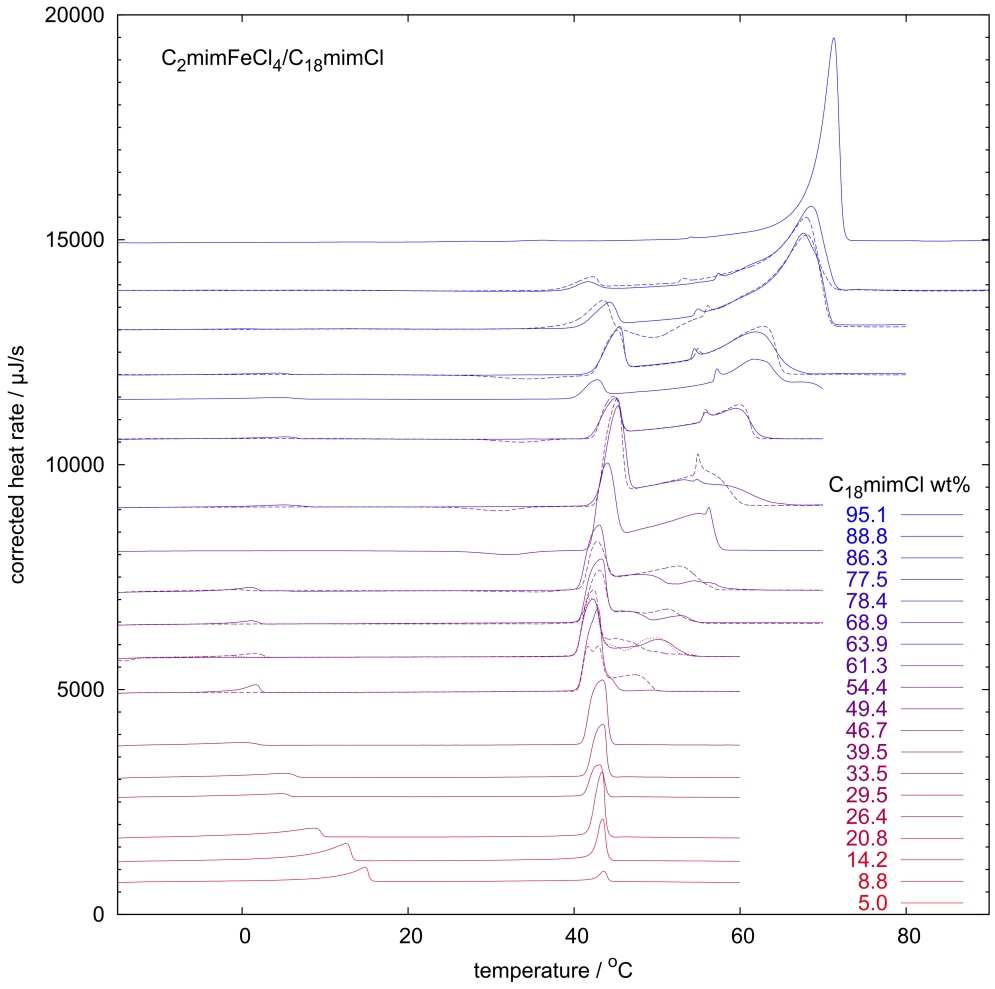

Figure A.9 DSC curves (background subtracted) for the system C_{18}mimCl/C_4mim$FeCl_4$. Increasing surfactant ratio is in ascending order. Curves are shifted relative to each other to enhance clarity.

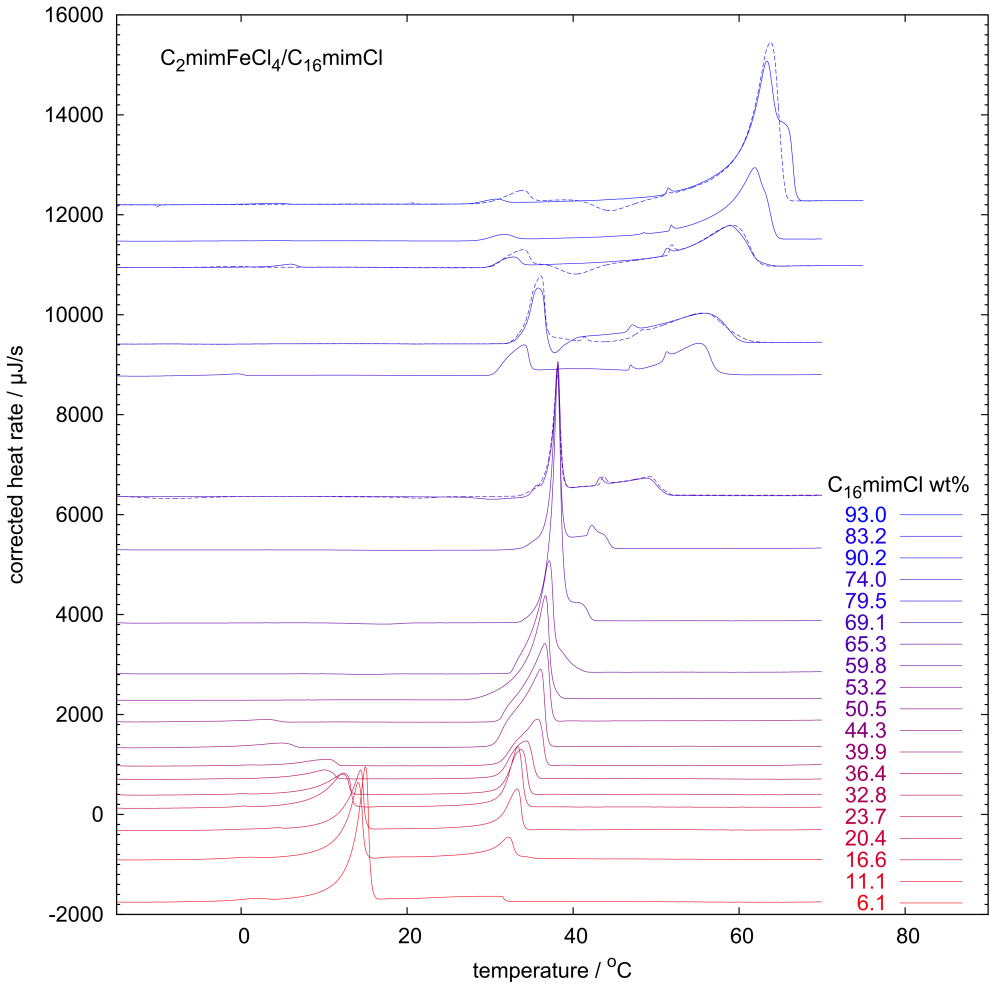

Figure A.10 DSC curves (background subtracted) for the system $C_{16}mimCl/C_2mimFeCl_4$. Increasing surfactant ratio is in ascending order. Curves are shifted relative to each other to enhance clarity.

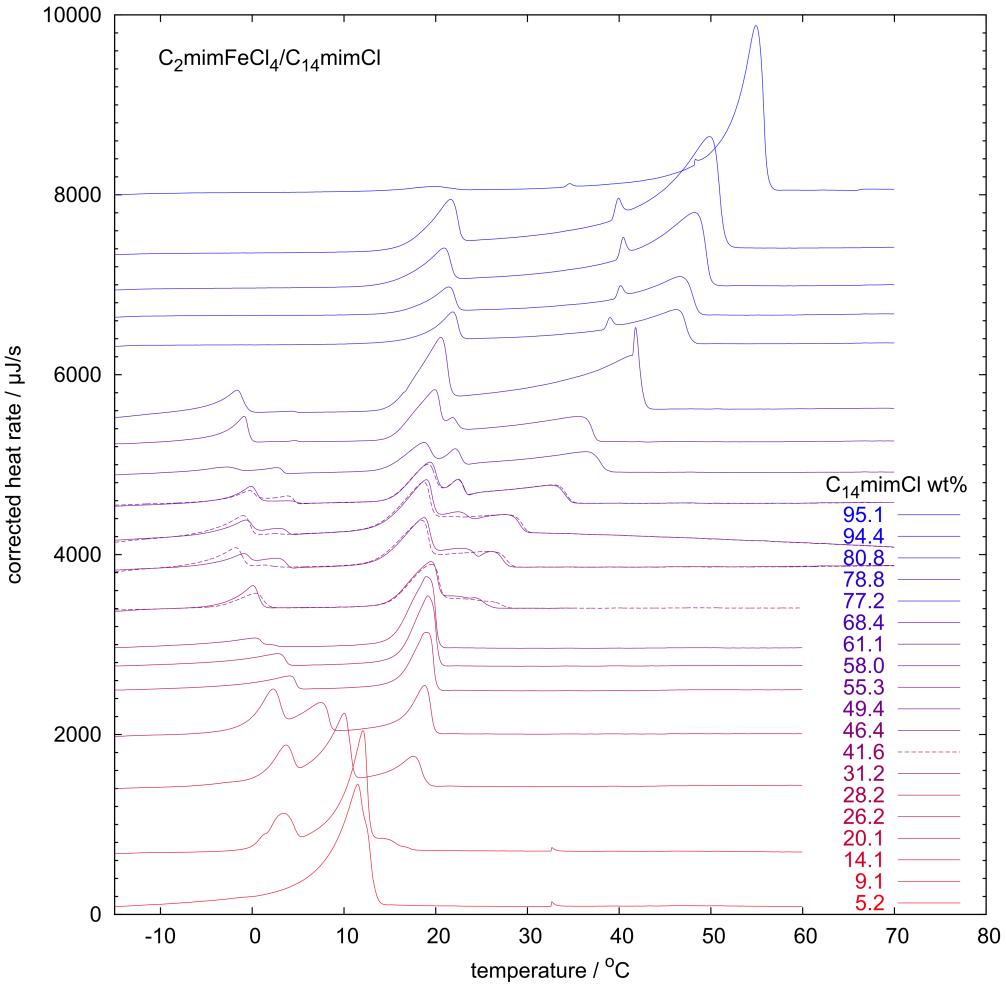

Figure A.11 DSC curves (background subtracted) for the system $C_{14}mimCl/C_2mimFeCl_4$. Increasing surfactant ratio is in ascending order. Curves are shifted relative to each other to enhance clarity.

Table A.4 Heats determined by the DSC integrals over all peaks (excluding the low temperature peaks for the C_2mimFeCl_4-system, see description above) normalized by the total sample mass m_{sample}, the surfactant mass m_{surf} and the surfactant amount n_{surf}. Q/n is plotted in Fig. 3.2.

C_{14}mimCl/C_2mimFeCl_4				C_{16}mimCl/C_2mimFeCl_4				C_{18}mimCl/C_2mimFeCl_4			
$\frac{\phi_{m,tot}}{\text{wt\%}}$	$\frac{Q/m_{sample}}{\text{J/g}}$	$\frac{Q/m_{surf}}{\text{J/g}}$	$\frac{Q/n_{surf}}{\text{kJ/mol}}$	$\frac{\phi_{m,tot}}{\text{wt\%}}$	$\frac{Q/m_{sample}}{\text{J/g}}$	$\frac{Q/m_{surf}}{\text{J/g}}$	$\frac{Q/n_{surf}}{\text{kJ/mol}}$	$\frac{\phi_{m,tot}}{\text{wt\%}}$	$\frac{Q/m_{sample}}{\text{J/g}}$	$\frac{Q/m_{surf}}{\text{J/g}}$	$\frac{Q/n_{surf}}{\text{kJ/mol}}$
26.2	35.2	134.6	42.41	11.1	15.6	140.1	48.07	8.8	11.7	132.7	49.24
28.1	37.4	133.1	41.91	16.6	23.9	144.2	49.46	14.2	21.8	153.5	56.94
31.2	40.4	129.4	40.77	20.4	29.5	144.6	49.61	20.8	34.6	166.2	61.66
41.5	59.6	143.6	45.22	23.7	35.2	148.1	50.81	26.4	42.9	162.5	60.27
46.4	64.8	139.5	43.95	36.4	57.8	158.8	54.45	29.5	46.7	158.3	58.75
49.4	66.0	133.5	42.06	39.9	70.0	175.5	60.18	33.5	56.7	169.0	62.71
55.3	78.6	142.2	44.81	44.3	71.4	160.9	55.20	39.5	64.5	163.3	60.59
61.1	86.5	141.4	44.55	53.2	83.8	157.5	54.01	46.7	78.3	167.6	62.20
58.0	80.1	138.1	43.51	59.8	93.9	157.0	53.84	49.4	83.3	168.5	62.51
68.4	94.6	138.3	43.56	65.3	102.0	156.1	53.55	54.4	93.2	171.4	63.59
78.0	109.5	140.5	44.25	69.1	112.5	162.7	55.80	61.3	102.8	167.6	62.16
77.2	112.7	146.0	45.99	74.0	121.9	164.6	56.46	63.9	112.5	176.0	65.31
80.8	112.8	139.5	43.95	79.5	128.8	162.0	55.57	68.9	122.4	177.6	65.87
84.2	120.9	143.6	45.24	83.2	134.6	161.8	55.51	77.5	135.7	175.1	64.97
95.1	132.6	139.4	43.91	90.2	158.1	175.2	60.10	86.3	155.6	180.2	66.86
				92.9	159.1	171.2	58.72	88.8	157.7	177.5	65.87
								95.1	156.8	164.8	61.15

(Continues on next page.)

(Continued from previous page.)

C_{14}mimCl/C_4mimFeCl$_4$				C_{16}mimCl/C_4mimFeCl$_4$				C_{18}mimCl/C_4mimFeCl$_4$			
$\frac{\phi_{m,tot}}{\text{wt\%}}$	$\frac{Q/m_{sample}}{\text{J/g}}$	$\frac{Q/m_{surf}}{\text{J/g}}$	$\frac{Q/n_{surf}}{\text{kJ/mol}}$	$\frac{\phi_{m,tot}}{\text{wt\%}}$	$\frac{Q/m_{sample}}{\text{J/g}}$	$\frac{Q/m_{surf}}{\text{J/g}}$	$\frac{Q/n_{surf}}{\text{kJ/mol}}$	$\frac{\phi_{m,tot}}{\text{wt\%}}$	$\frac{Q/m_{sample}}{\text{J/g}}$	$\frac{Q/m_{surf}}{\text{J/g}}$	$\frac{Q/n_{surf}}{\text{kJ/mol}}$
4.5	4.5	99.9	31.46	5.5	8.5	155.7	53.41	33.7	54.3	161.2	59.79
8.7	9.4	108.1	34.05	8.8	13.3	151.2	51.87	50.0	82.8	165.7	61.46
12.0	14.2	118.0	37.18	16.1	24.7	153.4	52.61	51.0	80.1	157.1	58.27
17.5	22.1	126.5	39.83	21.4	32.4	151.3	51.90	56.2	93.0	165.4	61.37
20.1	26.7	133.2	41.97	25.5	37.4	146.5	50.26	58.7	99.7	169.8	62.98
24.9	35.0	140.6	44.28	31.4	53.1	169.2	58.02	60.3	104.6	173.5	64.36
29.8	39.7	133.5	42.06	37.1	60.6	163.2	55.96	65.2	109.9	168.5	62.51
36.8	43.8	119.0	37.48	41.3	67.2	162.8	55.83	67.0	113.5	169.4	62.85
42.8	55.4	129.5	40.79	47.4	71.0	149.9	51.40	70.8	112.6	159.0	58.98
44.8	58.2	129.9	40.90	51.5	80.4	156.2	53.58	73.2	138.3	189.0	70.12
48.3	56.9	117.9	37.14	57.1	81.2	142.1	48.73	84.9	139.5	164.4	60.97
55.7	65.6	117.9	37.12	62.8	95.3	151.8	52.06	90.8	160.1	176.3	65.41
59.7	74.2	124.3	39.16	69.9	98.6	141.0	48.37	96.0	150.5	156.8	58.15
64.9	70.1	108.0	34.03	73.4	104.4	142.2	48.77	100.0	166.1	166.1	61.64
68.4	81.6	119.3	37.58	79.7	121.6	152.6	52.35				
73.4	83.8	114.1	35.95	84.5	116.3	137.6	47.19				
78.1	95.5	122.2	38.49	88.9	133.4	150.1	51.47				
81.2	102.6	126.3	39.79	94.9	135.4	142.6	48.91				
86.2	116.8	135.5	42.67	100.0	146.4	146.4	50.22				
90.8	127.5	140.4	44.23	100.0	143.4	143.4	49.19				
94.5	145.5	154.0	48.51								
100.0	146.9	146.9	46.28								

A.5 Surface tension

Table A.5 Fit parameters for the modified Szyszkowski model using eqs. 3.1a. The headgroup spacing is given by $a_s = 1/\Gamma$.

$C_xmimFeCl_4$	C_ymimCl	24 °C	45 °C	fit parameter							calc.
		$\frac{c_{10}}{\text{wt\%}}$		$\frac{cmc_\gamma}{\text{wt\%}}$	$\frac{\Gamma}{\text{nm}^{-2}}$	K_1	K_2	b	N	$\frac{\gamma^0}{\text{mN/m}}$	$\frac{a_s}{\text{nm}^2}$
2	14	—	6.36	11.66	1.58	0.409	8.21E-31	0.023	27.42	49.65	0.63
2	16	—	3.51	6.75	1.71	0.891	4.98E-38	0.020	43.37	51.05	0.58
2	18	—	1.91	4.90	2.07	1.186	6.96E-30	0.000	40.61	50.77	0.48
4	14	18.7	21.96	22.51	0.99	0.193	6.45E-58	0.035	41.69	44.92	1.01
4	16	12.3	15.44	15.76	1.01	0.373	2.53E-52	0.028	42.29	44.99	0.99
4	18	—	9.60	8.09	2.75	0.128	2.35E-38	0.020	40.20	44.70	0.36

A.6 Polarized microscopy

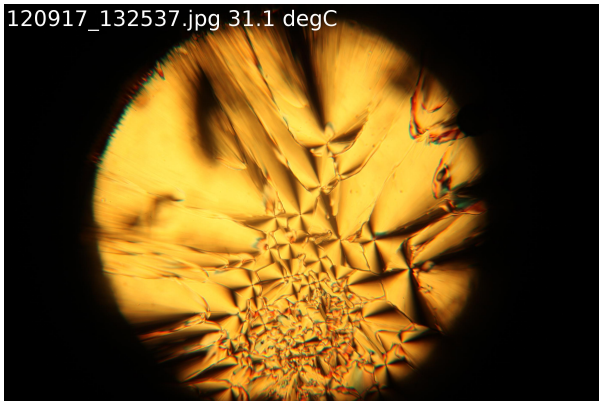

Figure A.12 Example for a polarized microscopy image at 31.1 °C of the metastable hexagonal phase in the system C_4mimFeCl$_4$/C_{14}mimCl exhibiting a typically fan-shaped texture.

A.7 SAXS

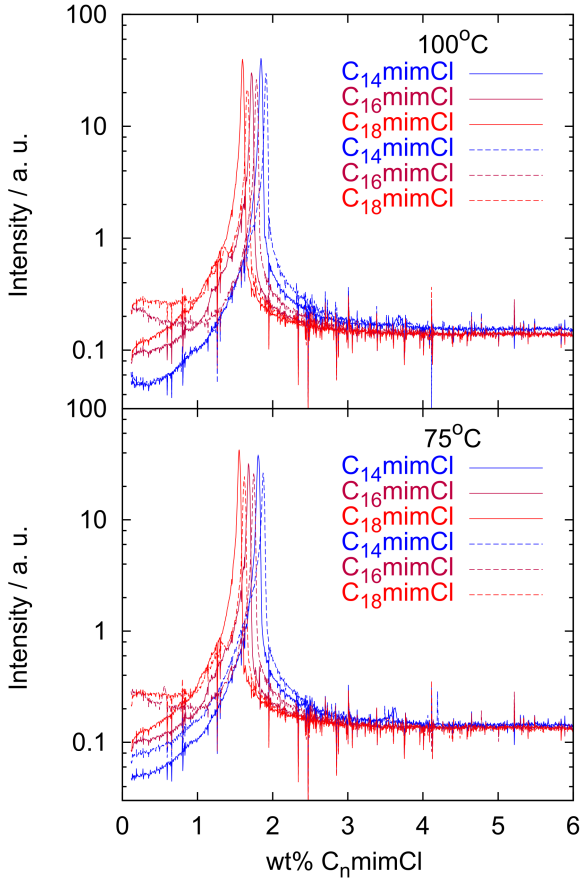

Figure A.13 SAXS curves for surfactant in C_2mimFeCl_4 (straight lines) and C_4mimFeCl_4 (broken lines) at 100 °C (top) and 75 °C (bottom). All samples have a content of 85 wt% surfactant.

B

Appendix — Microemulsions

B.1 Additional phase diagrams

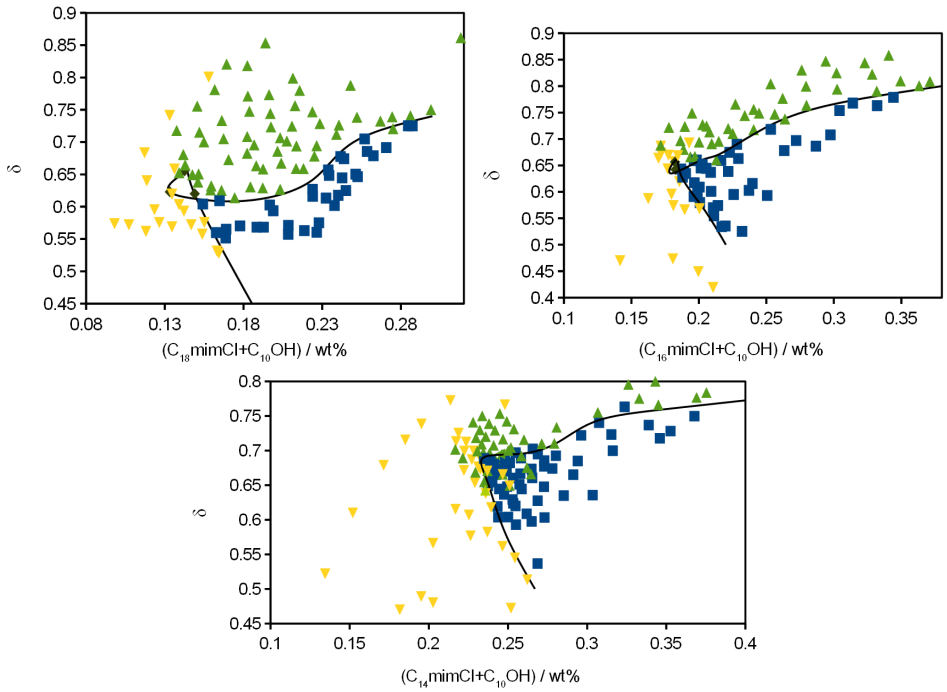

Figure B.1 Detailed view of all data points recorded for determining the fish-diagrams for C_4mimFeCl_4-based systems with C_{18}mimCl (top left), C_{16}mimCl (top right) and C_{14}mimCl (bottom). By visual observation the samples were classified as monophasic (blue squares), triphasic (black diamonds) or biphasic (triangles) with a bigger upper (yellow) or bottom (green) phase. From their position phase boundaries were interpolated (black line).

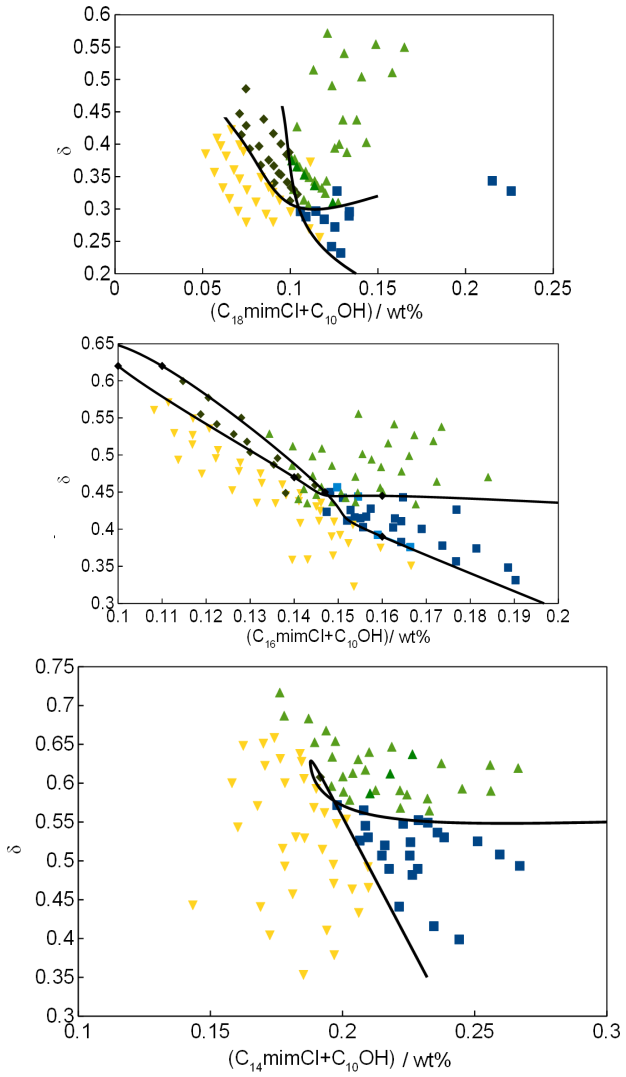

Figure B.2 Detailed view of all data points recorded for determining the fish-diagrams for C_2mim$FeCl_4$-based systems with C_{18}mimCl (top left), C_{16}mimCl (top right) and C_{14}mimCl (bottom). By visual observation the samples were classified as monophasic (blue squares), triphasic (black diamonds) or biphasic (triangles) with a bigger upper (yellow) or bottom (green) phase. From their position phase boundaries were interpolated (black line).

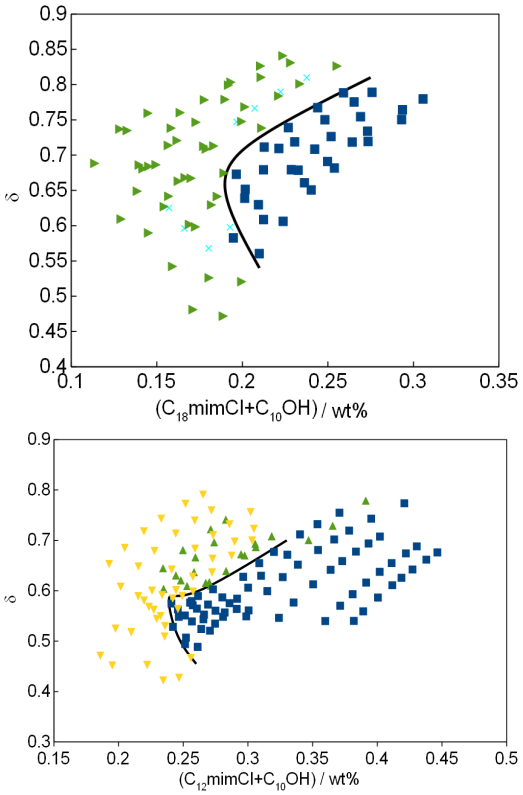

Figure B.3 Detailed view of all data points recorded for determining the fish-diagrams for the C_6mim$FeCl_4$-based system with C_{18}mimCl (top) and the C_2mim$FeCl_4$-based system with C_{12}mimCl as surfactant (bottom). By visual observation the samples were classified as monophasic (blue squares), triphasic (black diamonds) or biphasic (triangles) with a bigger upper (yellow) or bottom (green) phase. From their position phase boundaries were interpolated (black line).

B.2 The clipped random wave model[111,112]

The scattering intensity is described by an inverse eighth-order polynomial, which is an extension of the Teubner-Strey model. It contains three length-scale parameters with the inter-domain distance D_s, the coherence length ξ of the local domain order, and the surface roughness parameter c. While the first two parameters are similar to the analogous values in the Teubner-Strey model, the roughness parameter gives additional information and improves the model mainly in the high q range:

$$I(q) = \frac{4\,Q_{inv}\,b(a^2+(b+c)^2)/\pi}{(q^2+c^2)(q^4-2(a^2-b^2)q^2+(a^2+b^2)^2)} + BG \qquad \text{(B.1)}$$

$$a = 2\pi/D_s \qquad \text{(B.2)}$$

$$b = 1/\xi \qquad \text{(B.3)}$$

The amplitude scaling parameter Q_{inv} gives directly the scattering invariant. The fit parameters are listed in table B.1 and plotted in Fig. B.6. It can be seen that D_s and ξ are in a very good agreement with the Teubner-Strey model. In the oil rich region (low x_{MRTIL}) the surface roughness parameter c shows values comparable to water systems[112–114] (in our system they are slightly higher due to a higher surfactant concentration) and the trend of a growing roughness value with longer surfactant chains (means an increasing roughness) is as expected. Increasing the MRTIL content in the system gives continuously bigger c-values for all three systems which fits well to the general picture of a weakening of the mesoscopic structuring by increasing the MRTIL ratio. Above $x_{MRTIL} \approx 0.4$ the CRW-fits give high and erratic numbers for c. This is due to the fact that the roughness parameter is not necessary anymore to describe the SANS data (i. e. the fit quality is independent of c) as the TS itself gives already good fit results. Also remarkable is the fact that the simple two level model to explain the invariant (compare Fig. B.5) as well fails above $x_{MRTIL} \approx 0.4$ which gives a hint to structural changes at this point.

B.3 The scattering invariant Q_{inv}

The scattering invariant is defined as

$$Q_{inv} = \int_0^\infty I(q) \cdot q^2 \mathrm{d}q \tag{B.4}$$

During data analysis the invariant was determined by three different methods:

1. With the help of the program SASfit[70] the measured SANS data were integrated numerically whereby extrapolation to $I(0)$ and infinity was done by Guinier and Porod approximation, respectively. The background determination by Porod's law is shown in Fig. B.4 and all results are listed in Table B.1.

2. The CRW-model gives directly the invariant as a fit parameter.

3. The contrast fit parameter in the Teubner-Strey model (see eq. 2d) is directly related to the invariant by $Q_{inv} = 2\pi^2 \langle \eta^2 \rangle$.

All fit parameters are listed in Table B.1. The invariants determined by the three methods are plotted in Fig. B.5. The calculated invariants are strongly dependent on the chosen BG which explains the deviations between the three methods especially for low x_{MRTIL} (where the TS-fits have an obviously to low BG). For this reason the first method is the most reliable and was therefore chosen for further discussion in the main article.

Table B.1 Results for numerical SANS data analysis (including $I(0)$ from Guinier approximation and Porod's Law $I(q) = BG + C \cdot q^{-4}$) and fit parameters for Teubner-Strey and CRW fits.

		Teubner-Strey				CRW					Porod/Guinier			
	x_{MRTIL}	ξ [nm]	D_s [nm]	BG $[\frac{1}{\text{cm}}]$	Q_{inv} $[\frac{1}{\text{cm nm}^3}]$	ξ [nm]	D_s [nm]	c $[\frac{1}{\text{nm}}]$	BG [nm]	Q_{inv} $[\frac{1}{\text{cm nm}^3}]$	$I(0)$ $[\frac{1}{\text{cm}}]$	C $[\frac{1}{\text{cm nm}^3}]$	BG $[\frac{1}{\text{cm nm}^3}]$	Q_{inv} $[\frac{1}{\text{cm nm}^3}]$
C_{14}mimCl	0.05	1.67	4.86	0.29	11.87	2.12	4.24	1.20	0.48	7.24	2.48	5.57	0.48	8.83
	0.12	1.74	5.67	0.38	11.22	1.92	4.92	1.35	0.54	7.29	3.75	5.84	0.51	9.15
	0.19	1.79	6.15	0.48	10.69	1.82	5.55	1.80	0.60	7.38	4.32	6.26	0.57	9.32
	0.20	1.82	7.19	0.54	10.04	1.75	6.71	2.30	0.62	7.38	6.38	6.98	0.58	9.59
	0.37	1.77	8.82	0.59	8.76	1.75	8.73	5.80	0.61	7.44	9.18	7.94	0.57	9.49
	0.42	1.69	9.88	0.63	8.09	1.69	9.86	12.73	0.63	7.43	10.43	4.91	0.65	7.46
	0.49	1.54	10.77	0.65	6.54	1.54	10.77	> 25	0.65	6.54	9.73	6.22	0.63	7.02
	0.54	1.36	12.48	0.70	5.86	1.36	12.48	> 25	0.7	5.86	8.39	5.18	0.69	5.79
	0.60	1.27	13.85	0.66	4.35	1.27	13.86	> 25	0.66	4.35	6.44	3.75	0.66	4.18
	0.72	0.90	16.04	0.60	1.64	0.90	16.04	> 25	0.60	1.64	1.32	3.20	0.57	2.24
	0.77	0.87	8.95	0.58	0.62	0.87	8.94	> 25	0.58	0.57	0.23	1.94	0.55	1.17
	1.00	0.78	5.41	0.54	0.59	0.78	5.42	> 25	0.54	0.55	0.06	1.88	0.52	1.07
C_{16}mimCl	0.05	1.69	4.76	0.29	11.12	2.22	4.24	1.32	0.48	6.69	2.00	5.76	0.47	8.47
	0.12	1.91	5.38	0.41	9.98	2.19	4.82	1.44	0.55	6.60	2.61	5.58	0.52	8.46
	0.19	2.05	5.91	0.47	9.01	2.15	5.41	1.69	0.58	6.36	3.17	5.88	0.52	8.50
	0.27	2.20	6.42	0.57	8.45	2.18	6.13	2.48	0.64	6.52	3.86	5.11	0.61	8.13
	0.35	2.15	6.90	0.58	7.11	2.15	6.84	6.09	0.60	6.21	3.90	5.59	0.58	7.56
	0.42	2.11	7.24	0.62	5.96	2.10	7.25	> 25	0.62	5.98	4.05	4.69	0.60	6.40
	0.50	1.95	7.54	0.63	4.66	1.95	7.54	> 25	0.63	4.66	3.27	3.59	0.62	4.86

(Continues on next page.)

(Continued from previous page.)

		Teubner-Strey				CRW					Porod/Guinier			
	x_{MRTIL}	ξ [nm]	D_s [nm]	BG [$\frac{1}{\text{cm}}$]	Q_{inv} [$\frac{1}{\text{cm nm}^3}$]	ξ [nm]	D_s [nm]	c [$\frac{1}{\text{nm}}$]	BG [nm]	Q_{inv} [$\frac{1}{\text{cm nm}^3}$]	$I(0)$ [$\frac{1}{\text{cm}}$]	C [$\frac{1}{\text{cm nm}^3}$]	BG [$\frac{1}{\text{cm nm}^3}$]	Q_{inv} [$\frac{1}{\text{cm nm}^3}$]
(C_{16}mimCl)	0.55	1.87	7.57	0.68	4.14	1.86	7.58	> 25	0.68	4.14	3.04	3.68	0.66	4.51
	0.61	1.71	7.45	0.66	3.05	1.71	7.45	> 25	0.66	3.05	2.01	3.12	0.64	3.43
	0.71	1.53	6.84	0.63	1.09	1.53	6.84	> 25	0.63	1.09	0.54	1.38	0.62	1.29
	0.79	1.56	5.96	0.57	0.22	1.56	5.96	> 25	0.57	0.22	0.06	1.59	0.53	0.95
	0.94	1.41	4.85	0.54	0.20	1.41	4.85	> 25	0.54	0.20	0.01	0.62	0.53	0.36
	1.00	1.07	4.80	0.55	0.63	1.07	4.80	> 25	0.55	0.63	0.10	0.67	0.55	0.53
C_{18}mimCl	0.12	2.09	5.21	0.44	8.68	2.41	4.76	1.50	0.56	5.91	2.20	6.17	0.50	8.27
	0.19	2.27	5.70	0.48	7.60	2.41	5.31	1.79	0.57	5.52	2.42	5.77	0.51	7.77
	0.26	2.37	6.11	0.57	7.46	2.39	5.88	2.60	0.63	5.86	2.87	5.41	0.58	7.76
	0.33	2.35	6.51	0.59	6.32	2.35	6.45	5.54	0.61	5.52	2.83	5.98	0.55	7.41
	0.40	2.36	6.81	0.68	5.82	2.35	6.82	> 25	0.68	5.83	2.78	4.91	0.64	6.61
	0.47	2.19	7.12	0.68	4.70	2.19	7.12	> 25	0.68	4.70	2.85	4.28	0.65	5.40
	0.54	2.03	7.07	0.68	3.69	2.03	7.07	> 25	0.68	3.66	2.03	4.12	0.64	4.54
	0.59	1.92	7.18	0.68	2.74	1.91	7.18	> 25	0.68	2.74	1.54	2.85	0.66	3.23
	0.65	1.77	6.89	0.67	1.87	1.76	6.89	> 25	0.67	1.87	1.05	2.14	0.65	2.25
	0.75	1.58	6.14	0.59	0.51	1.58	6.14	> 25	0.59	0.50	0.17	0.42	0.58	0.48
	0.79	1.57	5.75	0.55	0.17	1.57	5.75	> 25	0.55	0.17	0.01	0.23	0.55	0.18
	0.94	1.52	5.52	0.55	0.24	1.52	5.52	> 25	0.55	0.24	0.01	-0.08	0.55	0.04

B.3.1 Calculation of theoretical invariant

Using eq. 5.2d, $\langle \eta^2 \rangle$ was calculated for two different cases: All hydrocarbon chains of the surfactant/cosurfactant are belonging to the oil phase (case 2), partitioning of the hydrocarbon chains (case 1, see table B.2). Scattering length densities (SLD) were calculated as

$$SLD = \frac{\sum_{i=1}^{n} b_{c_i}}{v_m} \tag{B.5}$$

where b_{c_i} is the bound coherent scattering length of atom i (taken from[127]) in the chemical group with molecular volume v_m. Used densities and resulting SLD are summarized in B.2. Resulting volume ratios and ρ for the two phases in case 1-3 were calculated under the assumption of invariant densities of chemical groups during mixing:

$$\Phi_{IL} = \sum \Phi_j \tag{B.6}$$

$$\rho_{IL} = \frac{\sum(\Phi_j \cdot SLD_j)}{\Phi_{IL}} \tag{B.7}$$

with the jth chemical group belonging to the IL phase. Φ_{oil} and ρ_{oil} where calculated analogously.

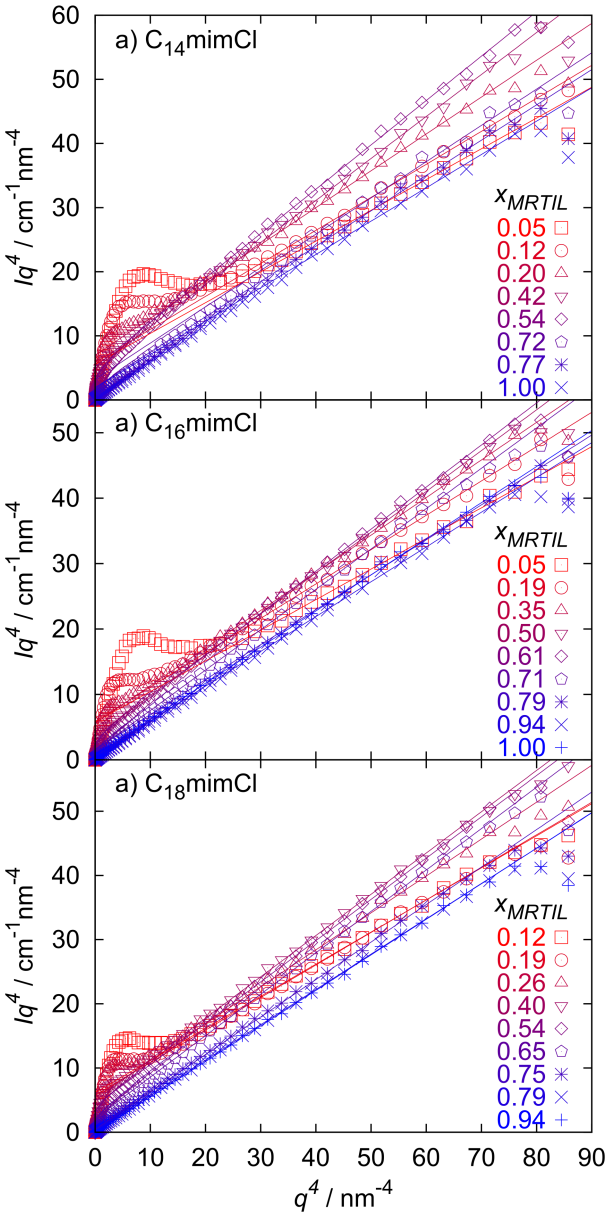

Figure B.4 Determination of the background (BG) by Porod's Law ($I(q) = BG + C \cdot q^{-4}$) Symbols are measured SANS data and lines are fits with Porod's law in the range $2.45\,nm^{-1} \leq q \leq 2.86\,nm^{-1}$ ($36.4\,nm^{-4} \leq q^4 \leq 67.3\,nm^{-4}$).

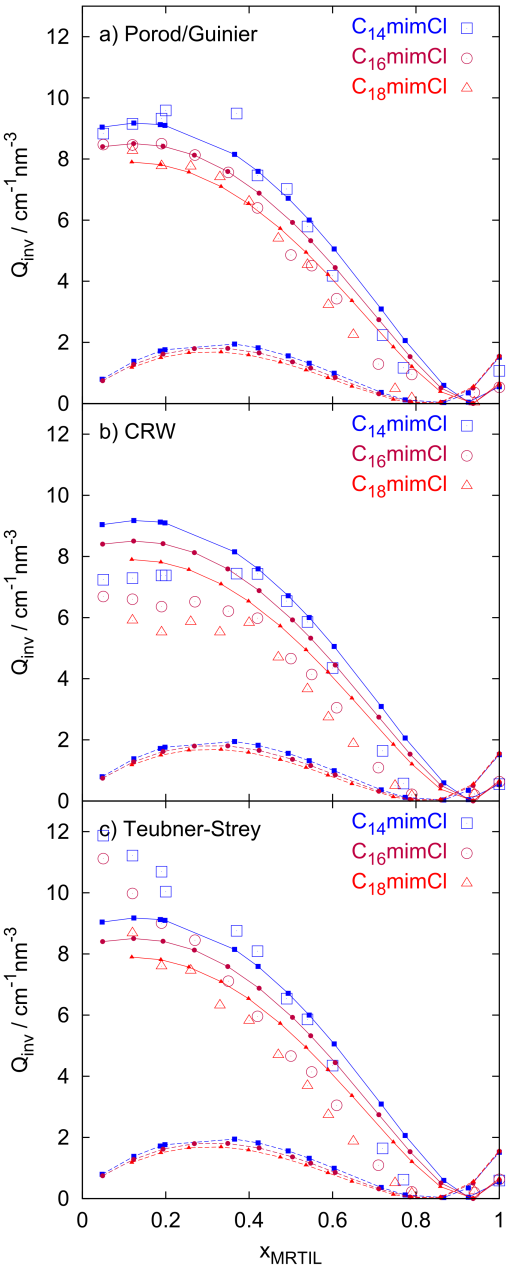

Figure B.5 Values for the scattering invariant as determined directly from the experimental data and using the Porod/Guinier approximation for the range where no experimental data is available. (a, open symbols), CRW fit (b, open symbols) and Teubner-Strey fit (c, open symbols). Small symbols are calculated invariants for two different distributions of surfactant/cosurfactant chains as described in the main article and in section B.3.1.

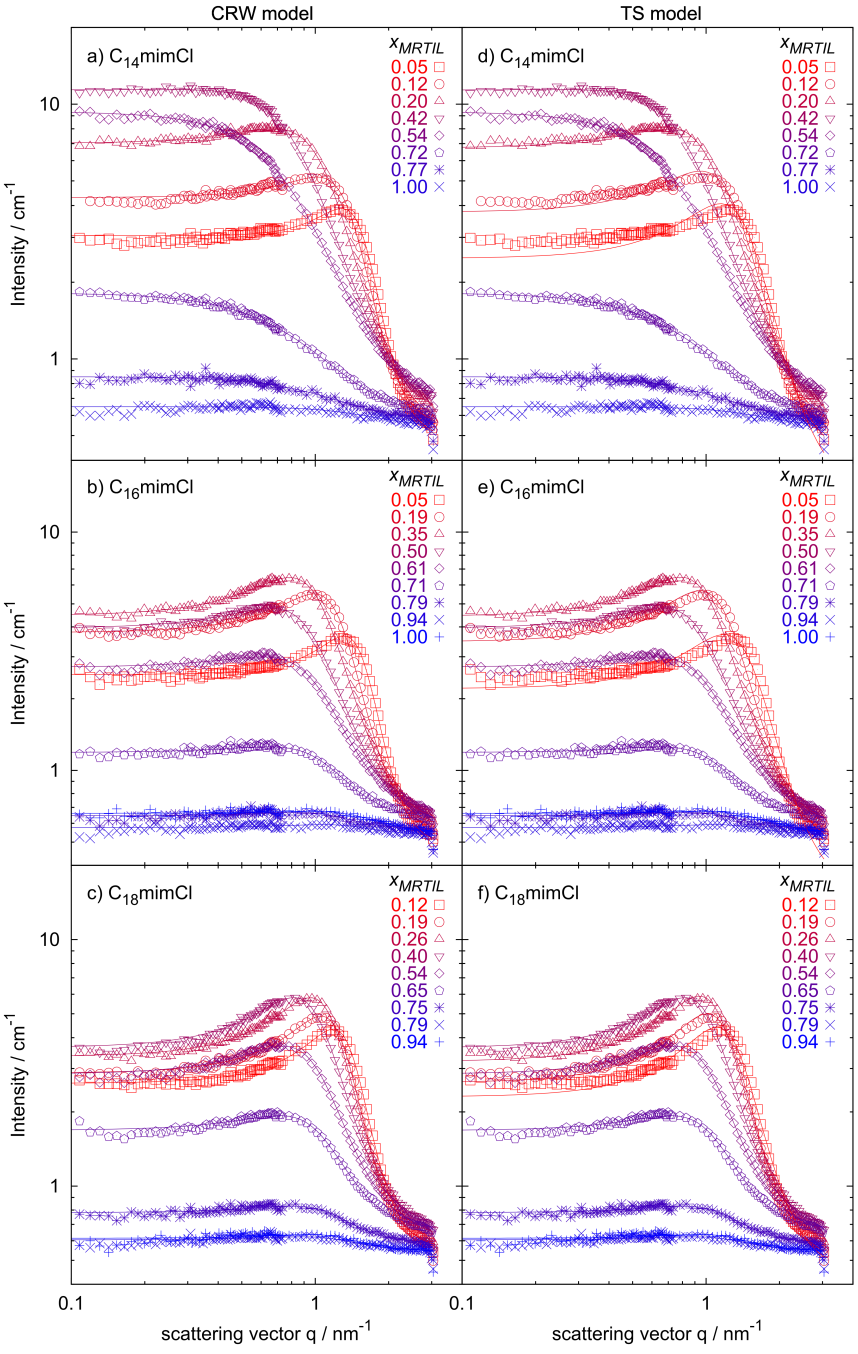

Figure B.6 SANS data (symbols) for the systems with C_{14}mimCl (top row), C_{16}mimCl (middle row) and C_{18}mimCl (bottom row) as surfactant. Lines are fits with the CRW (left column) and TS (right column) model. The corresponding parameters are listed in table B.1.

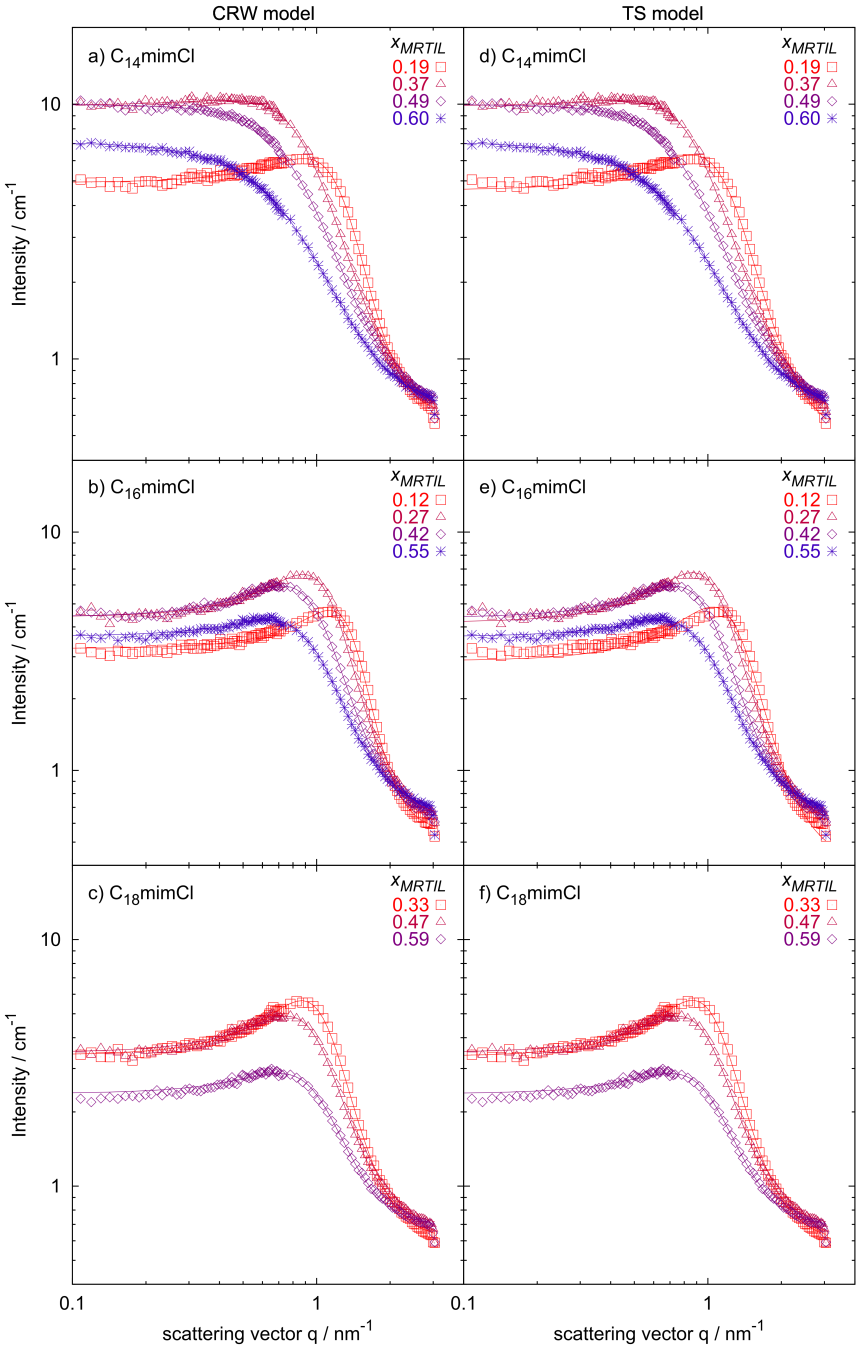

Figure B.7 SANS data (symbols) which were not plotted in the main article for the systems with C_{14}mimCl (top row), C_{16}mimCl (middle row) and C_{18}mimCl (bottom row) as surfactant. Lines are fits with the CRW (left column) and TS (right column) model. The corresponding parameters are listed in table B.1.

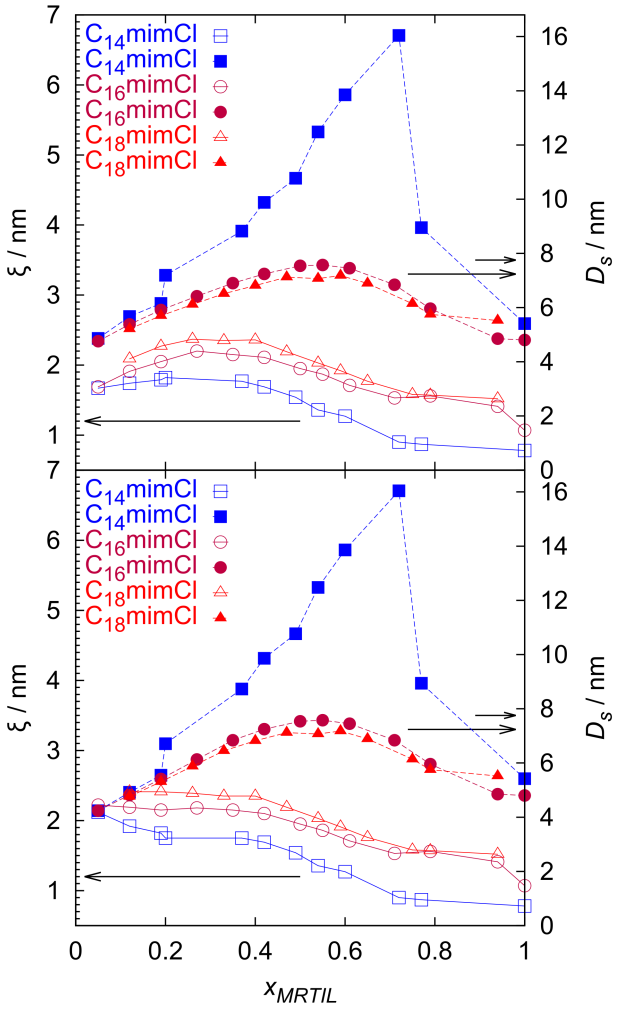

Figure B.8 Fit parameters ξ (open symbols) and D_s (filled symbols) as derived from Teubner Strey (top) and CRW (bottom) fits. The values are mostly identical for both models. Only for small x_{MRTIL} the CRW-model gives slightly higher values for ξ. Values are additionally listed in table B.1.

Table B.2 Characteristic parameters of different chemical groups used to calculate values for $Q_{inv} = 2\pi^2 \langle \eta^2 \rangle$.

	parameters		location in IL/oil-phase	
chem. group	density/g cm^{-3}	SLD/10^{-4}nm^{-2}	case 1	case 2
C_4mimFeCl_4	1.36	1.55	1/0	1/0
D12-cyclohexane	0.89	6.68	0/1	0/1
-mimCl	1.45	2.41	1/0	1/0
decyl	0.79	-0.41	6/4	0/1
-OH	1.42	1.04	1/0	1/0
tetra-	0.81	-0.38	7/7	0/1
hexa- decyl	0.82	-0.37	7/9	0/1
octa-	0.82	-0.37	7/11	0/1

B.4 SANS experiments recorded at D11 (ILL)

The SANS data were analyzed by fitting with the Teubner-Strey model similar to the data measured at PSI (SANSII). Results are plotted in Fig. B.9 and listed in table B.4. As described in section B.3.1, the fitted value for $\langle \eta^2 \rangle$ was compared with calculated values from the real sample compositions for three possible divisions of the interface. Results are listed in table B.4 and plotted in Fig. B.10.

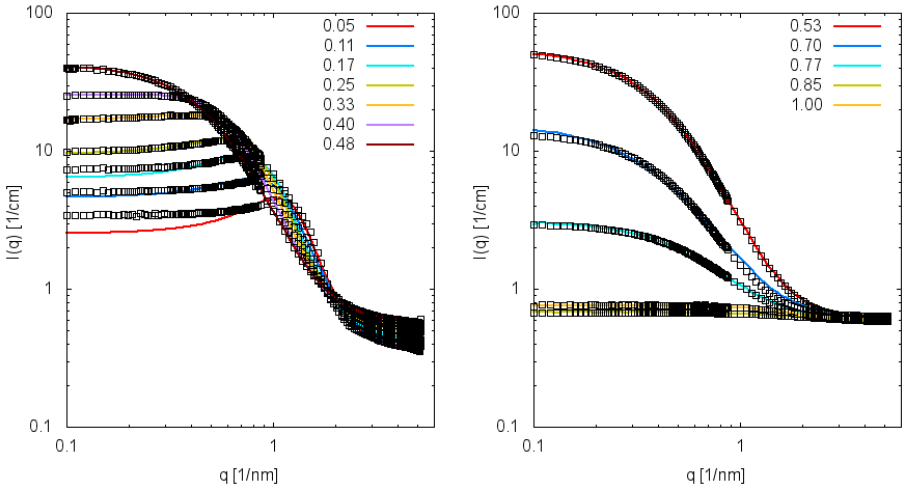

Figure B.9 SANS curves with D12-cyclohexane as the oil phase. The samples are along the experimental path shown in Fig. 5.18. Ratios between MRTIL and oil are x_{MRTIL}=0.05-0.48 (left) and x_{MRTIL}=0.53-1.00 (right) and are given in the inset. Lines are fits with the TS model.

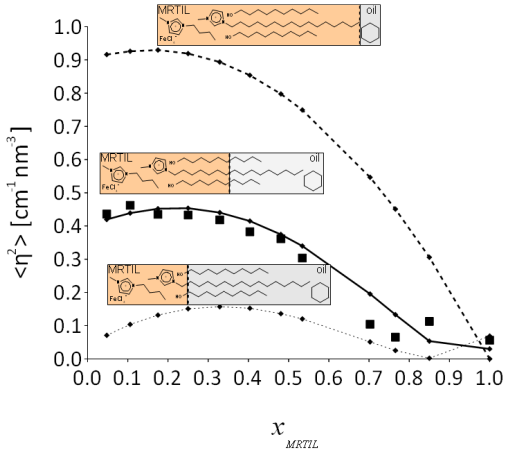

Figure B.10 $\langle \eta^2 \rangle$ as deduced from the TS fits (filled squares) compared to values calculated as described in section B.3.1 from the real sample compositions for three possible divisions of the interface: The whole interface is counted into the IL phase (dashed line), all hydrocarbon chains of the surfactant/cosurfactant belong to the oil phase (dotted line), and partial partitioning of the hydrocarbon chains (full line).

Table B.3 Characteristic parameters of different chemical groups used to calculate values for $\langle \eta^2 \rangle$.

	parameters		location in IL/oil-phase		
chem. group	density/g cm^{-3}	SLD/10^{-4}nm^{-2}	case 1	case 2	case 3
C_4mimFeCl$_4$	1.36	1.55	1/0	1/0	1/0
D12-cyclohexane	0.89	6.68	0/1	0/1	0/1
-mimCl	1.45	2.41	1/0	1/0	1/0
decyl	0.79	-0.41	1/0	0.6/0.4	0/1
hexadecyl	0.82	-0.37	1/0	0.375/0.625	0/1
-OH	1.42	1.04	1/0	1/0	1/0

Table B.4 Parameter for the TS fits shown in B.9 and calculated values for $\langle \eta^2 \rangle$.

	fit parameter SASfit				calculated $\langle \eta^2 \rangle$ /cm^{-1}nm^{-3}		
x_{MRTIL}	$\frac{\xi}{\text{nm}}$	$\frac{D_s}{\text{nm}}$	$\frac{\langle \eta^2 \rangle}{\text{cm}^{-1}\text{nm}^{-3}}$	$\frac{BG}{\text{cm}^{-1}}$	case 1	case 2	case 3
0.05	2.05	5.44	0.4356	0.3500	0.9161	0.4195	0.0709
0.11	1.90	6.53	0.4623	0.3669	0.9259	0.4388	0.1037
0.17	2.29	7.48	0.4349	0.4313	0.9297	0.4519	0.1317
0.25	2.28	8.59	0.4331	0.4851	0.9191	0.4536	0.1509
0.33	2.29	10.76	0.4184	0.5359	0.8936	0.4404	0.1570
0.40	2.30	13.39	0.3827	0.5657	0.8537	0.4149	0.1523
0.48	1.86	27.36	0.3614	0.5881	0.7975	0.3745	0.1361
0.53	1.96	60.00	0.3034	0.5981	0.7493	0.3398	0.1203
0.70	1.74	60.00	0.1043	0.6352	0.5466	0.1953	0.0511
0.77	1.14	60.00	0.0653	0.5951	0.4509	0.1331	0.0252
0.85	0.35	6.00	0.1128	0.5757	0.3059	0.0534	0.0019
1.00	0.65	5.64	0.0576	0.6000	0.0000	0.0299	0.0687

B.5 SANS curves measured at 36 °C

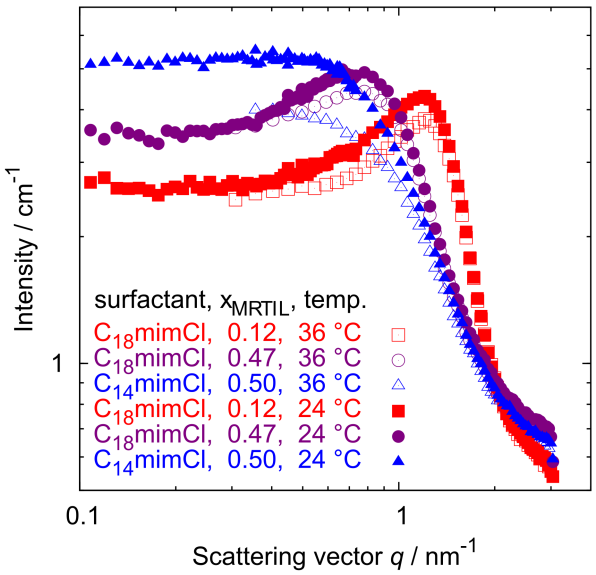

Figure B.11 SANS data measured at 24 °C (filled symbols) and 36 °C (open symbols) for three different microemulsion systems.

B.6 SANS experiments recorded at SANSI (PSI) under magnetic field

Table B.5 Composition of all samples measured in SANS experiments under magnetic field. It should be mentioned that in Fig. 5.20 and 5.22 for consistency the mass fractions were recalculated to H12-cyclohexane with the same volume.

$\frac{C_2mimFeCl_4}{wt\%}$	$\frac{C_4mimFeCl_4}{wt\%}$	$\frac{C_{14}mmCl}{wt\%}$	$\frac{C_{16}mimCl}{wt\%}$	$\frac{C_{18}mimCl}{wt\%}$	decanol	D12-cyclohexane
–	45.7	12.2	–	–	12.7	29.5
–	45.1	13.8	–	–	11.5	29.5
–	49.1	–	10.4	–	8.3	32.2
–	47.8	–	12.0	–	8.9	31.3
–	51.5	–	–	9.4	5.9	33.2
–	50.1	–	–	10.8	6.0	33.1
33.0	–	8.3	–	–	5.2	20.4
32.7	–	9.7	–	–	4.9	20.1
34.4	–	–	7.4	–	2.6	21.2
33.8	–	–	9.1	–	2.7	20.7
10.9	–	–	8.9	–	3.0	77.2
21.6	–	–	48.5	–	15.1	14.9
32.9	–	–	34.3	–	10.6	22.2
35.6	–	–	31.0	–	9.7	23.7
38.9	–	–	26.9	–	8.2	26.1
35.2	–	–	–	6.7	1.2	21.7
35.1	–	–	–	7.1	1.1	21.6
10.0	–	–	–	9.2	1.6	79.2

B.7 Surface tension

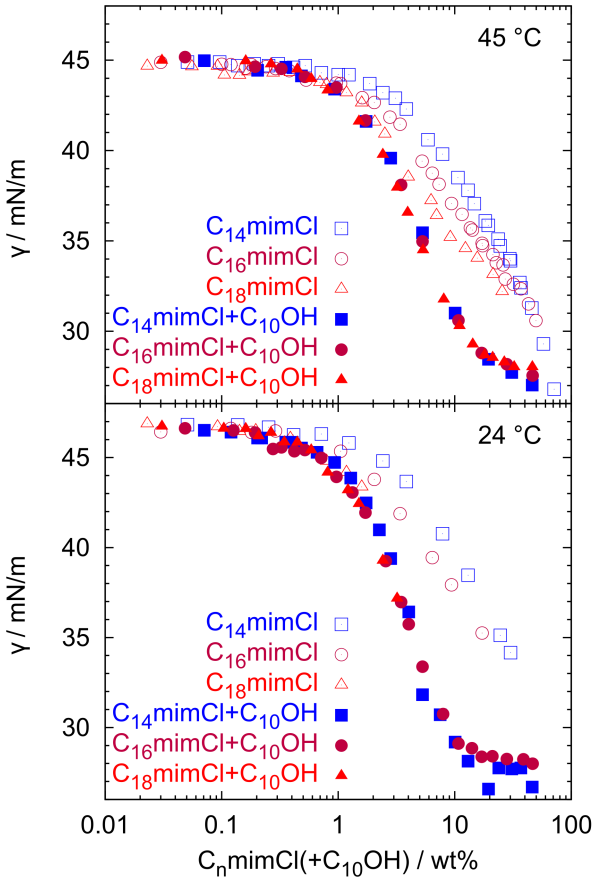

Figure B.12 Surface tension of $C_j$mimCl without (open symbols) and with 2 molecules decanol per surfactant molecule (filled symbols) in C_4mim$FeCl_4$ at 45 °C (top) and 24 °C (bottom).

B.8 Conductivity

A first insight into this mesoscopic microemulsion structure can be deduced from the conductivity titration shown in Fig. B.13. With increasing MRTIL content the conductivity increases by one order of magnitude, which is due to the formation of a structure continuous in MRTIL. In water and oil containing microemulsions as well as in systems with an IL substituting the water such a percolation behavior of the conductivity is well known and can be explained by structural transitions between a droplet and a bicontinuous structure.[51] The behavior of our MRTIL system is analogous and shows a percolation point of conductivity around $x_{MRTIL} \approx 0.1$, determined by plotting the specific conductivity with an exponent of 5/8 versus x_{MRTIL} (Fig. B.13).[63,128]

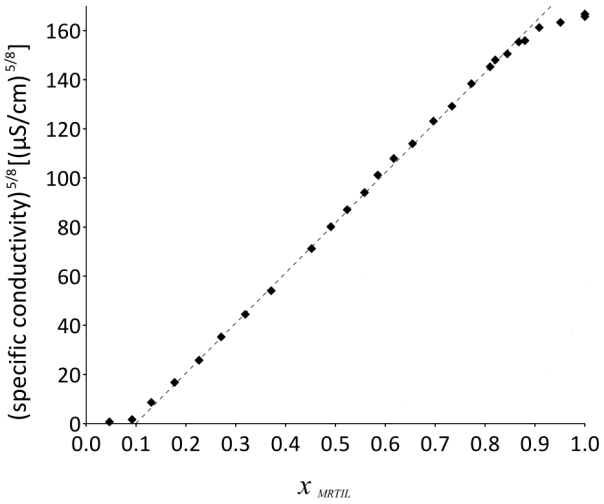

Figure B.13 Specific electric conductivity as a function of the MRTIL volume ratio (eq. 5.11) for the microemulsion system C_4mim$FeCl_4$/C_{16}mimCl. The broken line is a guide to the eyes. Measurements were done along the experimental path shown in Fig. 5.18.

B.9 Viscosity

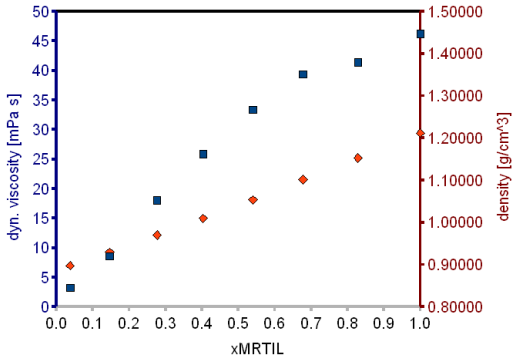

Figure B.14 Dynamic viscosity (squares) and density (diamonds) of microemulsions with a constant amphiphile mass ratio (C_{16}mimCl+decanol) of 23 wt%. along the experimental path shown in Fig. 5.5. Viscosities are low and in the range obtained for assuming a linear relation for the MRTIL/cyclohexane mixture viscosities, i.e., they are determined simply by the liquid components of the microemulsion.

B.10 Cube model

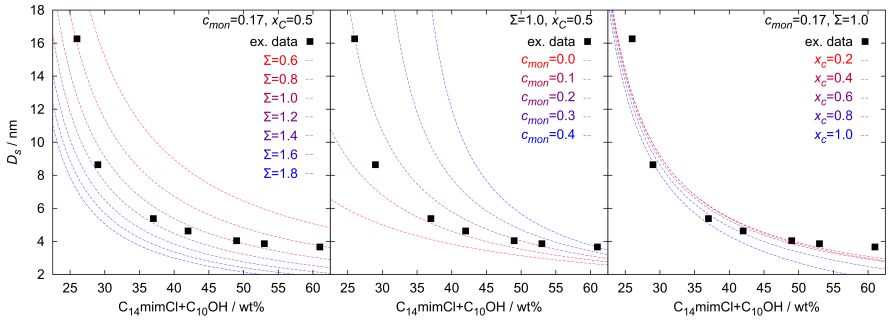

Figure B.15 D_s as derived experimentally with Teubner-Strey fits (filled squares) from SANS curves displayed in Fig. 5.7. Dashed lines display the cube model defined with eq. 5.6 for various different parameters.

B.11 Force Calculations in a Magnetic Field

Using the volume magnetic susceptibilities given in table 5.5, and densities of $1.36\,\mathrm{g/cm^3}$ (C_4mimFeCl_4) and $0.779\,\mathrm{g/cm^3}$ (cyclohexane), the field gradient to fulfill the condition $F_{grav} = F_{mag}$ can be calculated to be $\nabla B = 4.4\,\mathrm{Tm^{-1}}$, which effectively fits into the range of $3\,\mathrm{Tm^{-1}} \leq \nabla B \leq 46\,\mathrm{Tm^{-1}}$ which is given by the field profile along the sample estimated in Fig. B.16.

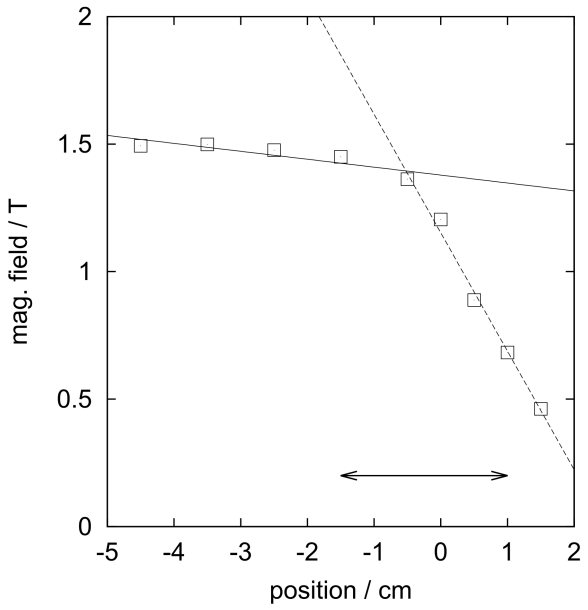

Figure B.16 Magnetic field profile of the magnet used for the data shown in Fig. 5.16 and measured as described in section 2.11. The position of the edge of the magnet plates where the sample was located is set to zero. The lines give linear fits whose slope gives directly the field gradient of $\nabla B = 46\,\mathrm{Tm^{-1}}$ (broken line) or $3\,\mathrm{Tm^{-1}}$ (straight line). The double-arrow gives the approximate sample position.